Trinity College Dublin
Coláiste na Tríonóide, Baile Átha Cliath
The University of Dublin

AI-based Taxonomic Classification of Pollinators and Advanced AoA Estimation from mm-Wave and Microwave Signals

---

Author:
Linta ANTONY

Supervisor:
Adam NARBUDOWICZ

Co-Supervisors:
Nicola MARCHETTI

This thesis is submitted in fulfilment of the requirements for
the degree of Doctor of Philosophy
in the
Department of Electronic & Electrical Engineering
March 2026

Declaration

I declare that this thesis has not been submitted as an exercise for a degree at this or any other university and it is entirely my own work.

I agree to deposit this thesis in the University's open access institutional repository or allow the library to do so on my behalf, subject to Irish Copyright Legislation and Trinity College Library conditions of use and acknowledgement.

I consent to the examiner retaining a copy of the thesis beyond the examining period, should they so wish.

Elements of this work that have been carried out jointly with others or by collaborators have been duly acknowledged in the text wherever included.

12-03-2026

Date

Linta Antony

Abstract

Biodiversity is declining at an unprecedented rate worldwide, with insects, particularly pollinators, among the most severely affected groups. Robust monitoring of pollinator populations is essential for safeguarding ecosystem stability, wild plant diversity, and global food production. However, traditional taxonomic identification is labour-intensive, dependent on expert knowledge, and often requires lethal sampling. Moreover, insect abundances fluctuate strongly across space and time due to weather and land-use dynamics, making high-resolution, scalable monitoring challenging.

Although Machine Learning (ML) approaches have been explored for image-based insect identification, their sensitivity to lighting, background clutter, and image quality limits their usability in real-world monitoring. By contrast, Millimetre-Wave (mmWave) radar operating in the 30 GHz range with wavelength comparable to insect body and wing dimensions offers a non-invasive means to capture fine-scale biomechanical signatures, including micro-Doppler modulations generated by wing flapping. Despite this promise, most radar-based entomology studies focus on morphological parameter estimation (e.g., Wingbeat Frequency (WBF), mass, velocity) and do not exploit the rich harmonic content or modern ML capabilities needed for reliable species-level classification.

This thesis addresses this gap by proposing a non-invasive, low-cost mmWave radar framework for hierarchical taxonomic classification of pollinating insects. As an initial contribution, the thesis investigates the fundamental interaction between flying insects and mmWave antennas through electromagnetic simulation. A dynamic insect model is developed to quantify variations in antenna gain and reflection coefficient (S_{11}) induced by micro-Doppler motion in the antenna's near field. These simulations provide initial evidence that insect wing dynamics create measurable perturbations in received mmWave signals, motivating the development of a radar-based classification framework.

Building on this insight, the thesis introduces a mmWave radar pipeline for hierarchical taxonomic classification of pollinating insects. A comprehensive signal-processing and

ML pipeline is presented to isolate micro-Doppler activity, extract informative temporal–spectral features, and classify insects at family, genus, and species levels. Explainable Artificial Intelligence (AI) methods are integrated to reveal the critical bio-mechanical and harmonic features underpinning model decisions, improving trust and interpretability.

Beyond empirical radar sensing, the thesis explores the potential of Joint Sensing and Communication (JSC) for insect monitoring. The feasibility of insect detection from a modulated communication signal is also demonstrated, enabled by a semi-supervised segmentation algorithm that autonomously identifies micro-Doppler-active signal regions.

Finally, the thesis contributes to compact antenna design for multi-target localization by addressing different spherical-mode-based Angle-of-Arrival (AoA) estimation methods. A novel Virtual Modes (VM) concept is introduced to enhance angular resolution, reduce computational cost, increase degrees of freedom, and minimise size - weight constraints in compact antenna systems.

Acknowledgements

I would like to dedicate this short chapter to all those who have helped and guided me during my PhD journey. This thesis is a result of the research carried out during my four years as a Doctoral student in CONNECT, the Science Foundation Ireland Research Centre for Future Networks and Communications, at Trinity College Dublin, the University of Dublin, under the supervision of Prof. Adam Narbudowicz and co-supervision of Prof. Nicola Marchetti. The work was supported by Trinity College Dublin Kinsella Challenge-Based E3 Award, Nature+CONNECT, funded by Microsoft and Research Ireland through CONNECT, the Research Ireland Research Centre for Future Networks and Communications (13/RC/2077_P2). For this, I am immensely grateful.

I would like to express my deepest gratitude to my supervisor Assoc.Prof.Adam Narbudowicz for his exceptional guidance, insightful feedback, and the many learning opportunities he provided throughout this research journey. His patience and unwavering kindness greatly eased my research journey. I am especially grateful for his continuous support, even after he relocated for a new position; despite his demanding schedule, he continued to mentor and guide me with remarkable generosity. This dissertation would not have been possible without his dedication, encouragement, and belief in my work.

I would like to express my sincere gratitude to my co-supervisor, Prof. Nicola Marchetti, for his unwavering support, thoughtful mentorship, stimulating discussions, and constant kindness. His encouragement and insightful guidance greatly strengthened this work and shaped many aspects of my research journey. This thesis would not have been possible without his dedication.

I am also deeply grateful to Prof. Ian Donohue for his continuous support, valuable guidance, and brilliant suggestions throughout these years, all of which significantly enriched my research.

I am profoundly thankful to Prof. Jane Stout for her expert guidance in insect handling and for her generous support and advice, which were indispensable to the practical aspects

of this work.

I would like to thank all my colleagues in CONNECT, the School of Engineering, and the School of Computer Science and Statistics. To Danh, Linh, Athira, Sumayia, Agastya, Bruno, Arijeet, Yang, Abel, Maryam, Pieter, Litty, and many more, your friendship, positivity, and constant support have been invaluable during this research.

I am deeply grateful for my family's unwavering support. Their love, encouragement, and belief in me have been a constant source of strength through every challenge of these years. I am especially thankful to my beloved husband, Sibin, whose immeasurable support, patience, perseverance, and trust have carried me through the most difficult moments. His endless love and encouragement have made the journey toward this dissertation immeasurably lighter and brighter. I wish to express my deepest gratitude to my dear parents, Antony and Leema. Their love, wisdom, and unwavering belief in me have shaped every step of my journey. I hope that completing this thesis brings them the joy and pride they truly deserve and reminds them of the profound role they have played in everything I have achieved. I am also grateful to my brother Leo for his constant support and encouragement throughout these years.

Above all, I am profoundly grateful to the Almighty for granting me strength, clarity, and perseverance throughout this journey. Without His grace and guidance, none of this would have been possible.

Contents

List of Acronyms

AI	Artificial Intelligence
AoA	Angle-of-Arrival
CNN	Convolutional Neural Network
CW	Continuous-Wave
DAS	Delay-and-Sum
DoF	Degrees of Freedom
EM	Electromagnetic
ESPRIT	Estimation of Signal Parameters via Rotational Invariance Techniques
FIT	Finite Integration Technique
FMCW	Fequency Modulated Continuous Wave
IoT	Internet of Things
JSC	Joint Sensing and Communication
kNN	k-Nearest Neighbors
LiDAR	Laser Detection and Ranging
MFCCs	Mel Frequency Cepstral Coefficients
ML	Machine Learning
mmWave	Millimetre-Wave
MUSIC	Multiple Signal Classification
MVDR	Minimum Variance Distortionless Response
O-RAN	Open Radio Access Network
PEF	Pitch Estimation Filter
PEC	Perfect Electric Conductor

RCS	Radar Cross Section
RMS	Root Mean Square Energy
RMSE	Root Mean Square Error
ROC	Receiver Operating Characteristic
SHAP	SHapley Additive exPlanation
SISO	Single-Input Single-Output
SM	Spherical Modes
SMB	Spherical Modes Beamforming
SNR	Signal-to-Noise Ratio
STFT	Short-Time Fourier Transform
VNA	Vector Network Analyzer
VM	Virtual Modes
WBF	Wingbeat Frequency
ZCR	Zero-Crossing Rate

Chapter 1

Introduction

1.1 Overview

Biodiversity is declining rapidly worldwide, with accelerating species extinctions indicating the onset of a sixth mass extinction [1]. Tracking population trends in insects, including major pollinators, is challenging because their abundance varies with landscape characteristics such as agricultural land cover and other environmental pressures [2]. Pollinators support most flowering plants and many crops, making them central to global conservation priorities and ecosystem functioning [3]. However, substantial knowledge gaps and the absence of standardised monitoring methods persist, and long-term pollinator data remain scarce [4].

Conventional approaches to insect monitoring usually rely on collecting and killing specimens, after which specialists must sort them and identify species through detailed morphological examination [5]. Since these samples often include vast numbers of individuals and considerable taxonomic diversity, only part of the material can be identified, and many groups are assigned to broad taxonomic categories because of limited expertise. As a result, well-studied taxa receive disproportionate attention. The high labour demands of both field collection and specimen processing also limit how many locations can be surveyed and how often sampling can take place [6].

Recent advances in Artificial Intelligence (AI) offer promising ways to speed up routine insect classification tasks. Most current research applies AI-based computer vision to insect images [7], [8], drawing on the success of image recognition technologies in consumer devices. Annotated images can be used to train deep-learning models to identify organisms automatically. Despite advances in image processing, field applications remain fundamentally constrained by the difficulty of capturing usable images in the first place. Additional practical challenges persist, including sensitivity to light and weather conditions, high camera power requirements, large data transfer needs, and the use of hardware optimised for vertebrate detection rather than close-range, small-movement monitoring of insects [9].

A complementary approach involves the use of radar systems [10]. Entomological radar has a long history, having been used mainly to monitor mass migrations of insects at high altitudes [11], [12]. Yet these systems also relied on high-power equipment, making them costly to build, deploy, and maintain. Their size, and energy demand make it impractical to install large numbers of units in close proximity, which restricts achievable spatial and temporal coverage. In addition, these legacy radars are not designed to detect or classify individual insects flying near the ground. Most insects are simply too small relative to the operating wavelengths used in such systems, preventing the radar from detecting individual animals.

Recent studies have demonstrated the ability of electromagnetic simulation software to successfully simulate the Radar Cross Section (RCS) of airborne animals [13]. As it is not easy to model the electromagnetic scattering caused by an insect' complex body shape, several works discuss the use of spheres [14], prolate spheroids [15] and ellipsoids [16] to provide simplified electromagnetic modelling. While prior studies have successfully used spheres, spheroids, and ellipsoids to approximate insect bodies, these models are static and lack the anatomical and biomechanical dynamics that generate micro-Doppler signatures. Even in recent work demonstrating the value of anatomically informed models [17], the focus remains on static radar cross-section prediction rather than on the time-varying electromagnetic effects caused by insect motion.

Studies on radio wave reflection by insects have shown that RCS correlates with insect mass [18], while signal polarization relates to body length [19]. Wingbeat Frequency (WBF) can be extracted from radar echoes, as demonstrated in experiments where insects were affixed to polystyrene foam for accurate measurement [20]. Species identification of migratory insects has been achieved with high accuracy (84%-100%) using manually extracted morphological parameters such as mass, WBF, and length-to-width ratio [21]. In these studies, ground truth parameters were measured manually using instruments such as weighing scales, rulers, and stroboscopes, and then compared to estimates derived from radar signals. The reported errors, including a 40% root mean square percent error for mass and length-to-width ratio, and a 1 Hz standard deviation for WBF, reflect the accuracy of radar-based estimation relative to the manually measured values [22]. Recent research aims to improve the precision of extracting these morphological parameters to enhance insect identification [22], [23].

Insect wing flapping generates distinctive micro-Doppler signatures, providing valuable insights for radar-based analysis and identification. [24] used a 94 GHz radar to capture WBF from micro-Doppler signatures to differentiate mosquitoes and honeybees. [25] demonstrated a 5.8 GHz Continuous-Wave (CW) Doppler radar integrated with machine learning for automated honeybee hive surveillance, achieving behavioral classification by leveraging Doppler signatures at hive entrances.

However, many existing approaches in radar entomology focus primarily on basic parameters such as wingbeat frequency extracted from micro-Doppler signatures generated by wing flapping, and rarely take full advantage of the harmonic content of these signals or the capabilities of modern machine learning for classifying closely related insect species.

While mmWave radar represents a promising pathway for non-invasive insect sensing, recent developments in wireless communications now support Joint Sensing and Communication (JSC), allowing a single mmWave waveform to deliver data and perform high-resolution sensing at the same time. Integrating insect sensing capabilities within JSC systems can minimise hardware requirements, optimise energy usage, and unlock seamless deployment in future smart ecological monitoring networks.

To date, JSC has not been explored for near-field biological micro-Doppler sensing, and no existing work investigates whether hybrid communication–sensing waveforms can reliably capture insect wingbeat signatures.

Most insect detection studies rely on Single-Input Single-Output (SISO) radar, which provides temporal signatures but offers little information about *where* insects are located. For real-world ecological monitoring, especially in multi-insect scenarios, accurate AoA estimation is crucial. However, conventional phased arrays are bulky and unsuitable for field deployment around crops or natural habitats. Recent research has explored compact antenna systems based on spherical mode expansions, enabling high angular resolution with significantly fewer physical elements [26]. This work demonstrates that compact multi-mode antennas can achieve or surpass the performance of larger, traditional arrays with an equivalent number of RF transceivers, offering effective localization solutions. These studies show that in multi-mode antennas, resolution is tied to the number of effectively excited modes. The Degrees of Freedom (DoF), indicating the antenna's capacity to resolve multiple signals, is capped at $M - 1$, where M is the number of excited SM. Thus, enhancing resolution necessitates generating more modes. However, stimulating numerous modes within a confined space can compromise bandwidth and increase losses.

To address the above challenges, the thesis aims at the following research questions:

RQ1: How can electromagnetic insect modelling be used to study the micro-Doppler effects generated when an insect flies near a mmWave antenna?

RQ2: How can the presence of pollinating insects be automatically detected in mmWave radar signals?

RQ3: Do different pollinating insect species exhibit distinct wing-flapping and micro-Doppler patterns, and how can mmWave radar capture these differences?

RQ4: How effectively can micro-Doppler signatures be used to classify pollinating insects at different taxonomic levels (family, genus, species)?

RQ5: How feasible is it to use modulated mmWave waveforms for insect detection and micro-Doppler extraction?

RQ6: How can compact, spherical-mode-based antenna systems be used to achieve advanced multi-target localisation and AoA estimation?

1.2 Thesis Contribution

The novel contributions of this thesis are summarized below:

- **C1: Electromagnetic modelling of insect–antenna interactions.**
  A dynamic insect model capable of simultaneous wing flapping and translational motion is developed. Using full-wave electromagnetic simulations, this contribution

quantifies how insect micro- and macro-motions influence the antenna gain and reflection coefficient (S_{11}) in the near field. This directly addresses **RQ1**.

- **C2: Automated micro-Doppler activity detection.**

  An algorithm is designed to autonomously identify micro-Doppler–active regions within continuous mmWave radar recordings, enabling robust and efficient detection of insect presence without manual annotation. This addresses **RQ2**.

- **C3: Characterisation of species-specific wingbeat signatures.**

  A comprehensive analysis of temporal, spectral, and harmonic features is performed to reveal consistent and discriminative micro-Doppler patterns across different pollinating insect species. This addresses **RQ3**.

- **C4: Hierarchical micro-Doppler–based taxonomic classification.**

  A hierarchical machine-learning framework is developed to classify insects at multiple taxonomic levels (family, genus, and species). Explainable AI techniques are integrated to identify the most discriminative features driving model decisions. This addresses **RQ4**.

- **C5: Feasibility of using modulated signals for insect monitoring.**

  The capability of hybrid communication–sensing mmWave waveforms to simultaneously transmit data and extract micro-Doppler signatures is investigated. This demonstrates the potential for integrated sensing within future communication systems. This addresses **RQ5**.

- **C6: Virtual Modes for compact multi-target AoA estimation.**

  A novel Virtual Modes concept is proposed to enhance angular resolution, increase degrees of freedom, and reduce computational cost in compact antenna systems. This enables accurate multi-target localisation and directly addresses **RQ6**.

1.3 Thesis Outline

The outline of this thesis is shown in Figure 1.1. The remainder of this thesis is organised as follows:

Chapter 2 - Background Theory & Review of Related Work - This chapter introduces the scientific and technical foundations required for the thesis. It reviews global

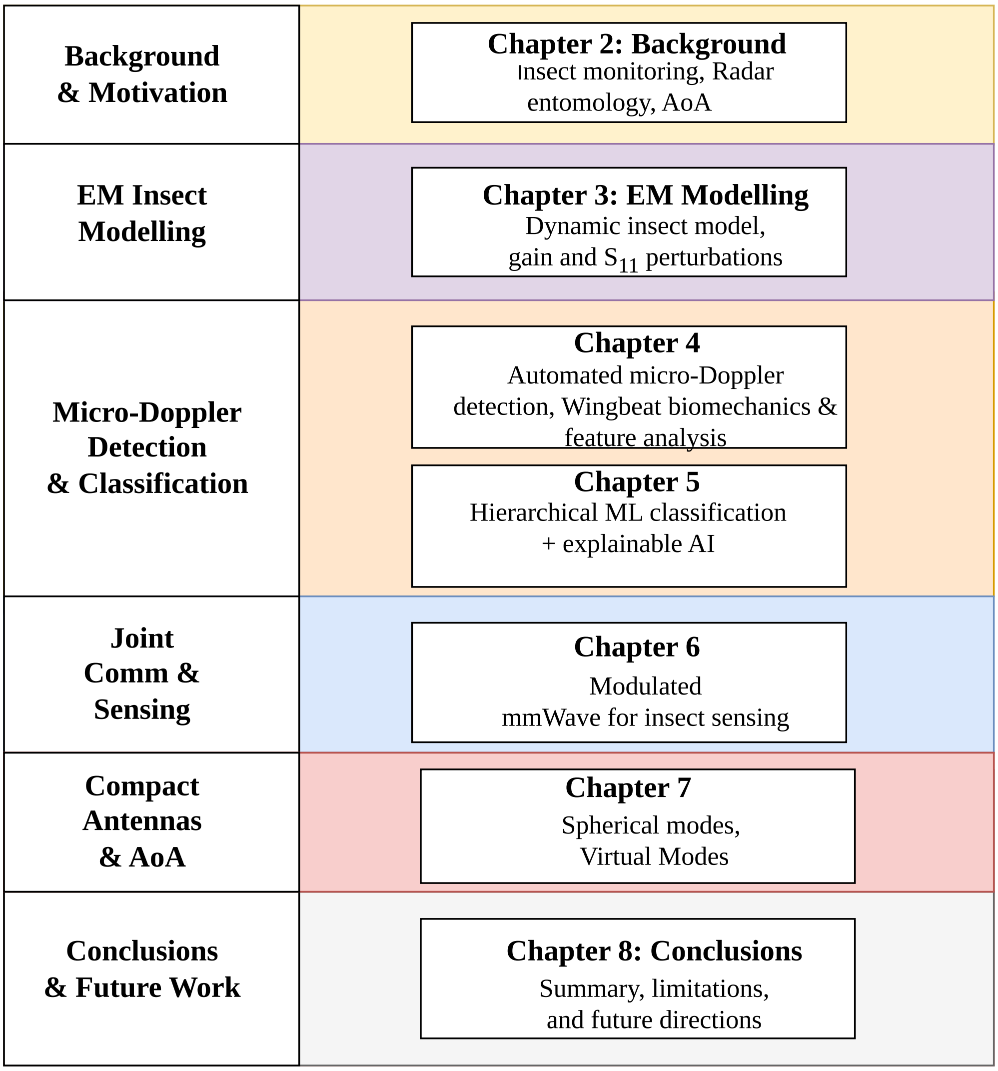

FIGURE 1.1: Outline of the thesis and its main research themes.

pollinator decline, insect biomechanics, and existing approaches to insect monitoring. It then summarises the fundamentals of mmWave radar, and introduction to fundamental concepts in AoA.

Chapter 3 -Micro-Doppler Effects in Flying Insects -This chapter provides the theoretical framework for understanding the micro-Doppler concept discussed throughout this thesis. Then, this chapter presents a dynamic wing-flapping insect model, and full-wave electromagnetic simulations are performed to quantify variations in antenna gain and reflection coefficient (S_{11}) caused by insect micro- and macro-motion in the near field. These results provide the physical motivation for later radar-based classification.

Chapter 4 - Micro-Doppler Feature Extraction and Analysis - This chapter introduces an algorithm for automatically identifying micro-Doppler active regions within continuous mmWave radar recordings. The method enables robust and efficient detection of insect activity without manual segmentation and forms the first processing stage of the radar pipeline. This chapter conducts a detailed analysis of temporal, spectral, and harmonic features extracted from micro-Doppler signatures. It demonstrates that different pollinating insect species exhibit distinct wingbeat patterns.

Chapter 5 - Taxonomic Classification of Insects - This chapter presents a hierarchical classification framework to identify pollinating insects at family, genus, and species levels. Explainable AI methods (e.g., SHapley Additive exPlanation (SHAP)) are used to interpret feature importance and provide biological insights into classification decisions.

Chapter 6 - Feasibility of insect detection with modulated signals - This chapter evaluates the feasibility of using modulated waveforms, i.e. as in telecommunication links, for micro-Doppler extraction. A hybrid digital phase modulated mmWave signal is synthesized on the basis of the measured data. It is studied to assess whether communication and sensing can be integrated for insect detection.

Chapter 7 - Virtual Modes for Compact Multi-Target AoA Estimation - This chapter evaluates classical AoA estimation techniques in the context of compact spherical-mode multiport antenna systems. This chapter introduces the Virtual Modes (VM) concept for spherical-mode-based AoA estimation in compact antenna systems. The method improves angular resolution, increases degrees of freedom, and reduces computational cost, enabling efficient multi-target detection.

Chapter 8- Conclusion & Future Work - In this chapter, we detail the conclusions of this thesis and discuss some of the open and existing research questions relevant to our work. Finally, we elaborate on the future directions of this research.

1.4 Dissemination

This section details the publications undertaken to disseminate the research findings of this PhD project.

Patent applications

- Antony, Linta, Norouzi, Maryam, Narbudowicz, Adam, and Donohue, Ian . "Detection and classification of flying insects by using micro-Doppler signatures of wing movement. " Patent Application 2411645.1

Journal

- Antony L, et al. "Harnessing mm-Wave Signals and Machine Learning for Non-Invasive Taxonomic Classification of Insects." *PNAS Nexus.*
- Antony L, Marchetti N, Donohue I, Narbudowicz A. "Insect Detection Using mm-Waves: Integrated Communication and Biodiversity Sensing Based on Micro-Doppler Effects." *IEEE Access. 2025 Jul 14.*
- Antony, Linta, et al. "Virtual spherical modes for aoa estimation with small sub-wavelength antennas." *IEEE Antennas and Wireless Propagation Letters 2024.*

Conference

- Antony L, Narbudowicz A. Study of Virtual Spherical Modes for Multi-Target Angle of Arrival Estimation. 2025 European Conference on Antennas and Propagation (EuCAP), Stockholm, Sweden, 2025 .
- Antony L, Marchetti N, Donohue I, Narbudowicz A. "Statistical Analysis of MM-Wave Signals for Enhanced Biodiversity Monitoring."*2025 International Conference on Statistics: Theory and Applications (ICSTA), Paris, 2025*
- Antony L, Zandamela A, Marchetti N, Narbudowicz A. "Angle of arrival estimation methods using spherical-modes-driven multiport antennas." *2024 European Conference on Antennas and Propagation (EuCAP), Galsgow, Scotland, 2024*
- Antony L, Zandamela A, Marchetti N, Narbudowicz A. Angle of Arrival Estimation Methods Based on Spherical Modes-Driven Multiport Antennas. *2023 International Symposium on Antennas and Propagation (ISAP), Kuala Lumpur, Malaysia, 2023*

Presentation

- Antony L, Narbudowicz A. Study of Virtual Spherical Modes for Multi-Target Angle of Arrival Estimation. 2025 European Conference on Antennas and Propagation (EuCAP), Stockholm, Sweden, 2025 .

- Antony L, Marchetti N, Donohue I, Narbudowicz A. "Statistical Analysis of MM-Wave Signals for Enhanced Biodiversity Monitoring."*2025 International Conference on Statistics: Theory and Applications (ICSTA), Paris, 2025*
- Antony L, Zandamela A, Marchetti N, Narbudowicz A. "Angle of arrival estimation methods using spherical-modes-driven multiport antennas." *2024 European Conference on Antennas and Propagation (EuCAP), Galsgow, Scotland, 2024*
- Antony L, Zandamela A, Marchetti N, Narbudowicz A. Angle of Arrival Estimation Methods Based on Spherical Modes-Driven Multiport Antennas. *2023 International Symposium on Antennas and Propagation (ISAP), Kuala Lumpur, Malaysia, 2023*
- Antony L, Marchetti N, Narbudowicz A. “mm - Wave Signal Technologies for Digitizing Biodiversity,” *Inaugural School of Engineering Research Symposium (SERS), Dublin, Ireland, 2024*
- Antony L, Marchetti N, Narbudowicz A. “mm - Wave Signal Technologies for Digitizing Biodiversity,” *Insect cost action, Tirana, Albania, 2025*
- Antony L, Marchetti N, Narbudowicz A. “mm - Wave Signal Technologies for Digitizing Biodiversity,” *Climate Gateway Launch, Dublin, Ireland, 2024*
- Antony L, Marchetti N, Narbudowicz A. “New Radar System for Biodiversity Monitoring,” *CONNECT Review, Dublin, Ireland, 2023*
- Antony L, Marchetti N, Narbudowicz A. “.Insect Biodiversity Monitoring using RADAR ,” *CONNECT Plenary, Waterford, Ireland, 2022*
- Antony L, Marchetti N, Narbudowicz A. “New Radar System for Biodiversity Monitoring,” *CONNECT Plenary, Clonmel, Ireland, 2024*

Non-Peer Reviewed Presentations

- Antony L, Marchetti N, Narbudowicz A. “mm - Wave Signal Technologies for Digitizing Biodiversity,” *Climate Gateway Launch, Dublin, Ireland, 2024*
- Antony L, Marchetti N, Narbudowicz A. “.Insect Biodiversity Monitoring using RADAR ,” *CONNECT Plenary, Waterford, Ireland, 2022*

Chapter 2

Background Theory & Review of Related Work

2.1 Global Pollinators Decline

Insect pollinators such as bees, butterflies, and hoverflies play a fundamental role in sustaining healthy ecosystems and global food production. An estimated 75% of crop species, 35% of agricultural output, and nearly 88% of flowering plants rely, at least in part, on insect-mediated pollination [3]. Yet, growing evidence indicates that many pollinator groups face mounting conservation pressures. Numerous studies over the past decade have documented alarming declines in insect abundance and diversity, with pollinators among the groups in decline [27]. Recent analyses of global collection datasets reveal a striking reduction in wild bee diversity, with one study documenting a 25% drop in the number of species reported compared with the 1990s [28]. Major drivers of decline include agricultural intensification, particularly habitat degradation and pesticide use, alongside climate change and the introduction of non-native species [1].

Despite their ecological and economic significance, comprehensive, large-scale assessments of distributional and population changes in key pollinator taxa, especially bees and hoverflies, remain largely absent. Existing species-specific datasets are typically derived from small-scale field studies that cover limited geographic areas and short time frames (<5 years). As a result, substantial gaps persist in both standardised monitoring approaches and long-term datasets, constraining our ability to implement effective conservation strategies and fully understand temporal trends in pollinator communities [29].

2.2 Insect Monitoring Methods

Effective monitoring is crucial to detect declines, understand their causes, and assess conservation actions. However, insects are small, highly mobile, and often very abundant, making them difficult to observe and count accurately. Traditional monitoring has relied on labour-intensive manual sampling, but recent advances in automated and non-invasive sensing technologies now offer promising alternatives.

2.2.1 Traditional Methods

Conventional field monitoring of insects typically relies on direct sampling and trapping methods, including sweep netting, pan traps, Malaise traps (which intercept flying insects and channel them into collection bottles), and light traps [30]. These approaches are simple and low-cost, and they yield physical specimens that can be identified to species by taxonomists. However, traditional methods typically require killing insects, followed by labour-intensive sorting and species identification by specialists. In many cases, the sheer number of individuals and the high taxonomic diversity in samples mean that only a subset is identified, or identification is limited to broad taxonomic groups. As a result, monitoring efforts are often biased toward well-studied groups, such as butterflies, while many other taxa are overlooked due to limited taxonomic expertise [5].

2.2.2 Computer Vision

Computer vision, a branch of computer science, develops algorithms that extract information from digital images and video. Early studies combined yellow sticky traps with image processing and machine learning to classify insects based on morphological features such as shape, colour, and texture [31]. The emergence of deep learning, particularly Convolutional Neural Network (CNN), has transformed this field by enabling automatic feature extraction directly from raw image data [8]. For example, Alves et al. [32] developed a dataset of cotton field pests spanning 15 categories and achieved 97.8% classification accuracy using a ResNet34-based CNN. Similarly, Kasinathan et al. [33] applied deep learning to a publicly available dataset containing 1,387 images across 24 classes captured against complex backgrounds. Several technical challenges currently hinder the widespread application of computer vision in entomological research. A primary limitation is the difficulty of consistently capturing high-quality images of small and fast-moving insects in natural environments. In addition, computer vision models require large, well-annotated training datasets, which are labour-intensive. Practical deployment is further constrained by camera power consumption, on-device processing requirements, and the need for reliable data transfer in remote field settings [6].

2.2.3 Acoustic Monitoring

Recent technological advances, together with the increasing availability of low-cost automated recording devices, have accelerated the use of bioacoustics, an emerging approach that employs sound to assess community composition and biodiversity within ecosystems [34]. Many insect taxa produce characteristic acoustic signals that can be exploited for monitoring. In acoustic surveys, field sensors record insect sounds, which are subsequently analysed using machine learning algorithms for species identification. Calling or courtship signals are typically captured using microphones or similar audio recorders and can be analysed in either the time domain [35] or the frequency domain [36]. However, these methods remain difficult to apply effectively in field settings, as they are highly susceptible to environmental noise and weather conditions. Moreover, not all environments are suitable for acoustic monitoring; for example, urban areas with substantial sound pollution and limited vegetation provide poor acoustic conditions for detecting insect signals. Additional constraints include the considerable human effort required for manually inspecting and annotating large acoustic datasets for model development, as well as the substantial energy and bandwidth demands associated with storing and processing such data [37].

2.2.4 LiDAR

Entomological LiDAR is a remote sensing technique that uses laser light to detect airborne insects. The system emits rapid laser pulses and measures the backscattered light from objects within the beam path. Optical approaches offer several advantages over microphones, as they are not affected by wind noise or ambient sound and can detect insects at considerable distances, including small-bodied species [38]. Using optical sensor data, Chen et al. [39] achieved 79.4% classification accuracy across 10 insect classes (flies and mosquitoes) using a Bayesian classifier. Recent field studies have shown that scanning LiDAR can generate detailed information on insect flight activity across habitats. For example, high-resolution LiDAR has been used to compare insect abundance and flight height over different land cover types, revealing distinct daily activity patterns and diversity profiles between forest and open field sites [40]. Despite these advantages, LiDAR systems are often complex and expensive, produce large data volumes requiring extensive processing, and are susceptible to noise introduced by sunlight, atmospheric conditions, and background structures such as vegetation.

2.3 Radar

Radars emit electromagnetic radiation that is reflected by objects in the air, and based on their echoes, these objects can be characterized. Among remote sensing techniques, radar stands out as one of the most established and promising approaches. Insect radar, in particular, has a long and well documented history and offers significant potential to address key limitations in current state of the art insect monitoring solutions [41]. The application of radar techniques in entomology dates back several decades, with some of the earliest demonstrations reported in [42] and was supplemented by other prominent works focused on individual insect detection [43]. Many recent works focus on new RCS information processing methods. For instance, Kong et al. [44] have presented a systematic investigation on insect cross sections in lab conditions; they conducted work with multiple frequencies and insect species and concluded that the measurement results confirmed the established system's effectiveness and accuracy. Another recent article [45] introduced an approach to insect mass estimation with support vector regression; the best-reached estimation accuracy of insect mass in lab conditions was 78%. Wang et al. [46] proposed a new detection method for maneuvering targets with small RCS; it was tested with many simulations and good field experiments. A fundamental way to characterize insect targets for radar is through electromagnetic modeling of their scattering. Simple shape approximations have often been used to simulate insect scattering: for instance, early studies considered insects as dielectric spheres or ellipsoids to estimate RCS and its variation with size, orientation, and frequency [13]–[15]. This simplification leverages classical scattering theory when the insect's dimensions are small relative to the wavelength. As radar technology advanced, more sophisticated models were explored – from point scatterer models to anatomically-inspired shapes [17].

Various mathematical solutions are considered for the improvement of the radar detection ability. For instance, Hu et al. [22] proposed using the second-order polynomial approximation for the insects' horizontal speed estimation for high resolution and full polarization radar set. In [22], the same research group has studied the invariant target parameters of a small sample of insects and proposed two methods for body mass and length calculation. Recent research aims to improve the precision of extracting these morphological parameters to enhance insect identification [23].

2.3.1 Motivation for Radar-Based Insect Monitoring

Radar systems offer several compelling advantages for insect monitoring, particularly in scenarios where non-invasive, automated, and continuous sensing is required. Unlike visual or acoustic methods, radar can operate under diverse lighting and weather conditions and does not rely on line-of-sight imaging, making it well-suited for deployment in natural, cluttered environments [47]. Furthermore, radar enables the capture of wingbeat frequency and micro-Doppler modulations [20]. These characteristics, combined with the increasing accessibility of compact, low-power Millimetre-Wave (mmWave) radar hardware, motivated the focus of this thesis on radar-based insect monitoring as a scalable and non-lethal alternative for biodiversity assessment.

2.4 Fundamentals of Radar

Radar is a term derived from the words "radio detection and ranging," and was initially created to detect and measure the distance of a target by transmitting radio waves. However, modern radars have evolved to include capabilities such as target location, imaging, and identification. A typical radar system consists of a transmitter, antenna, receiver, and signal processor [48]. Radar can be categorized into monostatic and bistatic types based on the physical distance between the transmitting and receiving antennas. In a monostatic radar, a single antenna is used for both transmitting and receiving, while in bistatic radar, the transmitting and receiving antennas are separated by a considerable distance [49]. Radar can also be classified based on the waveforms transmitted, such as CW radar, where the transmitter operates continuously, where a continues sinusoidal signal is constantly transmitted. Such a transmitter does not allow for distance measurement, as there is no reference point in the waveform [50]. Pulsed radar transmits a relatively short burst of pulses, and after each pulse, the receiver is turned on to receive the echo. In contrast, Fequency Modulated Continuous Wave (FMCW) radar transmits a continuous signal whose frequency is modulated over time. This allows the system to simultaneously extract both range and velocity information by analyzing the frequency difference between the transmitted and received signals [51].

mmWave radar operates at much higher frequencies than conventional RF systems, typically within the 30–300 GHz range. At these frequencies, the electromagnetic wavelength lies between $1 - 10$ mm, placing mmWave technology in the corresponding region of the electromagnetic spectrum, as illustrated in Figure 2.1.

Compared to other radar types, mmWave radar offers several advantages, including higher spatial resolution, strong penetration capabilities, and reduced interference. The short wavelength enables the detection of very small objects, such as insects. Additionally, they little to no impact on insect targets and are relatively insensitive to external environmental conditions [52].

Rapid advances in semiconductor technology, system design, and computational performance have significantly accelerated the development of mmWave radar over recent decades. Although the high cost of mmWave hardware was once a major barrier, modern semiconductor processes now allow the production of cost-effective mmWave devices.

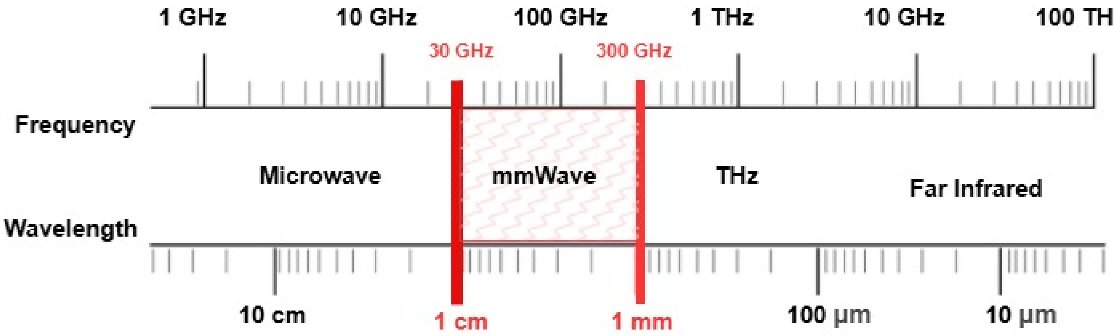

Figure 2.1: Spectral location of millimeter-wave frequencies.

2.4.1 Radar Equation

The radar equation is used to determine the range of a radar-based on various factors such as the transmitter, receiver, antenna, target, and distance. In the case of a monostatic radar, the equation takes into account the transmitted power (P_t), antenna gain (G), RCS

(σ), wavelength(λ) and the distance to the target (R). Using these factors, the equation calculates the power at the target as follows [48].

$$P_d = \frac{P_t G^2 \sigma \lambda^2}{(4\pi)^3 R^4} \tag{2.1}$$

This formulation assumes far-field conditions and is used in this thesis to provide an order-of-magnitude detectability estimate, in the near-field sensing configuration.

2.5 The Biomechanics of Insect flight: WBF and Morphometrics

Insect WBF shows remarkable variation across species, ranging from approximately 5–6 Hz in large, slow-flying dragonflies to more than 1000 Hz in minute midges. Typically, smaller insects exhibit significantly higher wingbeat rates than their larger counterparts [53]. The primary WBF is influenced by both wing loading and the insect's muscle physiology [54], [55].

Insects of the same body mass can have very different wing flapping speeds if their wing dimensions differ significantly [56]. High wing loading (heavy body, small wings) necessitates a higher WBF to generate sufficient lift. Low wing loading (light body, large wings) permits slower WBF. In addition to morphology, muscle physiology plays a crucial role in WBF. Asynchronous flight muscles, found in most endopterygote orders (e.g., Diptera, Hymenoptera, Coleoptera), enable multiple wing strokes per neural impulse and support very high WBFs, typically above 100 Hz. In contrast, synchronous muscles contract once per neural impulse, limiting WBF to a few tens of Hz, up to around 100 Hz at most [57]. Muscle physiology thus co-evolves with wing morphology. Insects with high wing loading often require asynchronous muscle to achieve the necessary WBF for flight [54].

Under constant flight conditions, the WBF (f_w) increases with the square root of wing loading (W/S), where W is the body mass and S is the wing area [58]. This frequency is further constrained by muscle physiology, such that f_w does not exceed the muscle's natural contraction frequency (f_m). Based on this, f_w can be modeled as

$$f_w \approx C\sqrt{\frac{W}{S}}, \quad \text{subject to} \quad f_w \leq f_m \tag{2.2}$$

Here, C can be treated as an empirical constant that represents aggregate aerodynamic factors.

2.6 Review of Existing Insect Models

Direct measurements of the radar signatures of flying organisms, particularly insects, remain technically challenging [17], [59], [60]. Recent studies have shown that EM modelling techniques can reliably reproduce the radar scattering characteristics of airborne animals [13]. Nevertheless, accurately capturing the scattering behaviour of insects is non-trivial due to their complex morphology, heterogeneous internal composition, and the presence of fine structures such as wings and legs. A central question in this modelling effort is the level of anatomical and geometric fidelity required in the input model, and the extent to which specific morphological features influence the resulting radar signatures.

2.6.1 Simple Geometric Dielectric Models

Early entomological radar research often represented insects using highly simplified shapes typically spheres, finite cylinders, or prolate spheroids illuminated by plane waves. In these homogeneous dielectric models, an insect is approximated as a single body with uniform complex permittivity.

The perfectly conducting sphere is the most mathematically tractable model owing to its radial symmetry. However, the RCS of real insects is substantially more complex because EM energy penetrates the body, scatters from internal boundaries, and interacts with inhomogeneous tissues [48].

[61] demonstrated that an insect's RCS could, to first order, be approximated by a spherical water droplet of equivalent mass. Yet, because a sphere's backscatter is independent of viewing angle and polarization, this approximation fails to reproduce the strong aspect and polarization dependence observed experimentally in insect scattering.

As more detailed morphological data became available, these simple forms were extended to dielectric prolate-spheroid models [14], [15]. In this family of models, the insect is represented by a prolate spheroid whose dimensions are derived from measured body length and width distributions, often with aspect ratios around 3:1–4:1 for winged insects.

As morphological data improved, researchers adopted dielectric prolate-spheroid models [14], [15]. Here, body length and width distributions inform spheroid dimensions, typically with aspect ratios of 3:1–4:1 for many winged insects. Given the longstanding assumption that water content dominates insect scattering [62], many models treated insects as water-filled spheroids. Building on this, [63] introduced an "insect-equivalent RCS model," representing insects as single-layer ellipsoids filled with a generic biological medium (they use spinal cord tissue properties). More recently, [16] compared simulated RCS from ellipsoids with different material compositions and found that mixtures of chitin and hemolymph yielded scattering results closest to measured insect data.

2.6.2 High-fidelity Anatomical EM Models

Advances in imaging and computational EM have enabled the development of anatomically detailed models that go far beyond simple geometric approximations. [13] demonstrated that full 3D EM modelling based on high-resolution anatomical meshes derived from CT scans of bats and incorporating realistic tissue permittivities can accurately predict radar scattering across angles and polarizations. [64] extended similar computational EM techniques to airborne insects, developing methods to predict insect RCS using detailed geometry, tissue-specific permittivities, and method-of-moments or FDTD solvers. [17] constructed a high-fidelity three-dimensional insect model using micro-CT scans of a gold–palladium-coated specimen. Electromagnetic simulations performed in WiPL-D Pro under different morphological and material configurations demonstrated that high-resolution anatomical modelling provides clear advantages over the simple ellipsoidal models used in earlier studies.

2.7 Review of Dielectric and Electromagnetic Properties of Insects

Historically, entomological radar studies have assumed that the dominant contributor to electromagnetic scattering from insects is their high water content [62]. This assumption led to EM models that represented insects as homogeneous water-filled spheroids or ellipsoids [16], [63]. Water has a high relative permittivity (60) and a strong loss factor (–33), making it the dominant contributor to absorption and scattering in the microwave regime and thus a convenient surrogate material in insect EM models.

Laboratory studies have shown that homogenised insect tissues exhibit relative permittivities in the range of approximately 30–40 at microwave frequencies, with substantial dielectric losses (loss factors around –16 to –21) [65]. These values vary markedly between species. For example, homogenised pastes of the lesser grain borer (*Rhyzopertha dominica*), the rice weevil (*Sitophilus oryzae*), the red flour beetle (*Tribolium castaneum*), and the saw-toothed grain beetle (*Oryzaephilus surinamensis*) all exhibit high permittivity values (30–40) and large negative loss factors, reflecting their high water content and ionic conductivity [65].

In contrast, chitin, the principal structural component of the exoskeleton, has a much lower dielectric constant (3.8–4.5) and a negligible loss factor (–0.14 to –0.18), indicating that it contributes weakly to microwave absorption [66].

2.8 Angle of Arrival (AoA) estimation

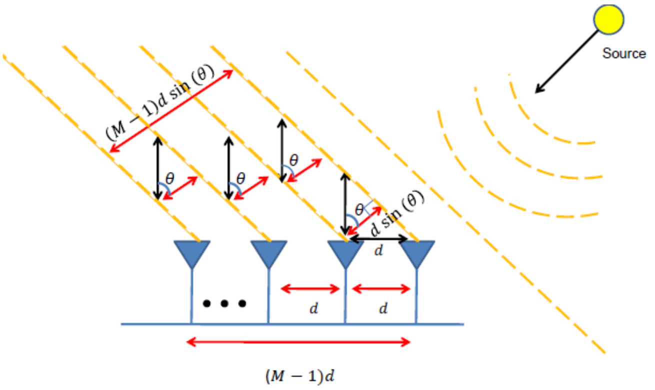

FIGURE 2.2: Classical linear array used for AoA Estimation

Localization refers to the process of determining the position or location of a target or signal source relative to a reference system. Accurate localization plays a crucial role across diverse domains, including wireless communication, navigation systems, autonomous vehicles, the Internet of Things (IoT), and environmental monitoring. AoA estimation is a popular localization technique based on relative angle measurements. In the state-of-the-art, the method is implemented using antenna arrays, where the AoA algorithms exploit the differential phase information from the array's output, from which the arriving signal's source direction can be computed [67].

The traditional setup for AoA estimation is illustrated in Fig. 2.2, where N independent sources arrive at a linear antenna array consisting of M elements. Assuming each source varies over time as $e^{j\omega t}$, the array's response to signals arriving from directions $\theta_1, \theta_2, \ldots, \theta_N$ can be represented as $\mathbf{A}$, which is formed from the array steering vectors:

$$\mathbf{A} = [a(\theta_1), a(\theta_2), \cdots, a(\theta_N)], \tag{2.3}$$

$$\vec{a}(\theta_i) = \left[e^{-jkd_1 \sin\theta_i}, e^{-jkd_2 \sin\theta_i}, \cdots, e^{-jkd_M \sin\theta_i} \right]^{\mathrm{T}}, \tag{2.4}$$

here, $k = 2\pi/\lambda$ is the wavenumber, and λ denotes the signal wavelength. It is essential to note that this array response assumes an ideal case with no mutual coupling between antenna elements. The received signal at the antenna array can be expressed in vector form as

$$\mathbf{x}(t) = \mathbf{A}\mathbf{s}(t) + \mathbf{n}(t), \tag{2.5}$$

where $\mathbf{x}(t) \in \mathbb{C}^{M\times 1}$ denotes the received signal vector across the M array elements, $\mathbf{s}(t) = [s_1(t), s_2(t), \ldots, s_N(t)]^{\mathrm{T}} \in \mathbb{C}^{N\times 1}$ represents the source signal vector corresponding to the N impinging sources, and $\mathbf{n}(t) \in \mathbb{C}^{M\times 1}$ is the additive noise vector, typically modeled as zero-mean spatially white complex Gaussian noise.

The spatial covariance matrix of the received signal is defined as

$$\mathbf{R}_{\mathbf{x}} = \mathbb{E}\left\{\mathbf{x}(t)\mathbf{x}^{\mathrm{H}}(t)\right\} = \mathbf{A}\mathbf{R}_{\mathbf{s}}\mathbf{A}^{\mathrm{H}} + \sigma_n^2\mathbf{I}, \tag{2.6}$$

where $\mathbf{R}_{\mathbf{s}} = \mathbb{E}\left\{\mathbf{s}(t)\mathbf{s}^{\mathrm{H}}(t)\right\}$ denotes the source covariance matrix, σ_n^2 is the noise variance, and $\mathbf{I}$ is the $M \times M$ identity matrix.

AoA estimation methods can generally be categorized into two broad classes: conventional (non-subspace-based) and subspace-based approaches.

1. Conventional Methods

These methods operate directly on the spatial covariance matrix ($R_{\mathbf{x}}$) without involving eigendecomposition.

- **Delay-and-Sum (DAS):** A straightforward beamforming approach that computes power in different directions by steering and summing phase-aligned signals [68]. For spherical-mode-based multiport antennas, the DAS power spectrum is given by:

$$P_{\mathrm{DAS}}(\theta) = \mathbf{a}^H(\theta)\,\mathbf{R}_{\mathbf{x}}\,\mathbf{a}(\theta) \tag{2.7}$$

- **Minimum Variance Distortionless Response (MVDR):** This method minimizes received power from all directions except the look direction, thereby offering better resolution in noisy or interfered environments [69]. The MVDR weight vector is:

$$\mathbf{w}(\theta) = \frac{\mathbf{R}_{\mathbf{x}}^{-1}\,\mathbf{a}(\theta)}{\mathbf{a}^H(\theta)\,\mathbf{R}_{\mathbf{x}}^{-1}\,\mathbf{a}(\theta)} \tag{2.8}$$

  and the output power is:

$$P_{\mathrm{MVDR}}(\theta) = \mathbf{w}^H(\theta)\,\mathbf{R}_{\mathbf{x}}\,\mathbf{w}(\theta) \tag{2.9}$$

2. Subspace-Based Methods

These methods rely on the eigenvalue decomposition of the spatial covariance matrix to separate signal and noise subspaces, offering significantly improved resolution.

- **Multiple Signal Classification (MUSIC):** MUSIC exploits the orthogonality between the noise subspace and steering vectors of actual signals [70]. Its spatial spectrum is defined as:

$$P_{\mathrm{MUSIC}}(\theta) = \frac{1}{\mathbf{a}^H(\theta)\,\mathbf{U}_n\,\mathbf{U}_n^H\,\mathbf{a}(\theta)} \tag{2.10}$$

  where $\mathbf{U}_n$ denotes the noise eigenvector matrix obtained via eigendecomposition of the spatial covariance matrix $\mathbf{R}_{\mathbf{x}}$, which can be computed from simulation or measurements.

- **Estimation of Signal Parameters via Rotational Invariance Techniques (ESPRIT):** Unlike other methods, ESPRIT does not require scanning across angles. It relies on forming two overlapping subarrays from a parent array with translational invariance [71]. The signal subspace produced by these subarrays maintains rotational invariance, and the ESPRIT algorithm leverages such invariance and operates with pairs of identical sensors known as doublets.

Chapter 3

Micro-Doppler Effects in Flying Insects

In this chapter, the concept of the micro-Doppler effect generated by a flying insect is introduced. The chapter establishes the theoretical framework underpinning the micro-Doppler analysis used throughout this thesis. It begins with a brief overview of the Doppler effect, followed by an introduction to the micro-Doppler phenomenon arising from the biomechanical motion of insect flight.

Next, a dynamic insect modelling approach is proposed to investigate how wingbeat-induced motion affects the antenna response in the near-field, in particular the variations in antenna gain and reflection coefficient (S_{11}). The dynamic modelling presented in this chapter was published in [72]. These simulations provide initial evidence that the wing dynamics of an insect can induce measurable perturbations in received mmWave signals, thereby motivating experimental validation of the micro-Doppler effect in the antenna's near-field.

Finally, the chapter presents the experimental verification of the near-field micro-Doppler effect at mmWave frequencies by analyzing reflected signals from individual flying insects.

3.1 Doppler Effect

When a radar system transmits an electromagnetic waveform toward a target, the incident field is scattered by the target and the resulting echo is received by the radar. The characteristics of the backscattered signal depend on the physical and dynamical properties of the target. For a target moving with a constant radial velocity, the carrier frequency of the received signal is shifted relative to that of the transmitted signal. This phenomenon is known as the Doppler effect, and the corresponding frequency offset is referred to as the Doppler shift [48]. The Doppler effect is of particular relevance in radar sensing because both the radar platform and the target may be in motion, such that the transmitted and backscattered fields can each be considered to originate from a moving source. Conceptually, the Doppler shift can be understood by recognizing that the motion of the source or observer compresses or stretches the effective wavelength of the waveform, resulting in an increase or decrease in the observed frequency.

The frequency shift caused by the Doppler effect can be calculated based on the relative velocity (V) between the radar and the target and the frequency (f) of the electromagnetic wave used by the radar.

$$f_D = -2fV/c \tag{3.1}$$

When a target is closing on the radar it introduces a positive Doppler shift, but has a negative velocity since range is measured away from the radar. By including a minus sign in the equations for Doppler shift a positive frequency shift is obtained for approaching targets

3.2 Retrieving Doppler Signatures Using Quadrature Detection

The quadrature detector consists of two synchronous detectors operating together, producing one output corresponding to the phase of the input signal and another corresponding to the same signal shifted by 90°, allowing the sign of the phase to be determined. The structure of the detector is shown in Figure 3.1. The received signal can be expressed as $A\sin(\omega_0 t + \phi)$, where $\omega_0 = 2\pi f_0$ is the radar's angular reference frequency and ϕ is the phase shift introduced by the motion of the target. The synchronous detection process removes the reference carrier from the received signal, leaving only the phase variation. The mixer stage represents a multiplication of the signals leading to:

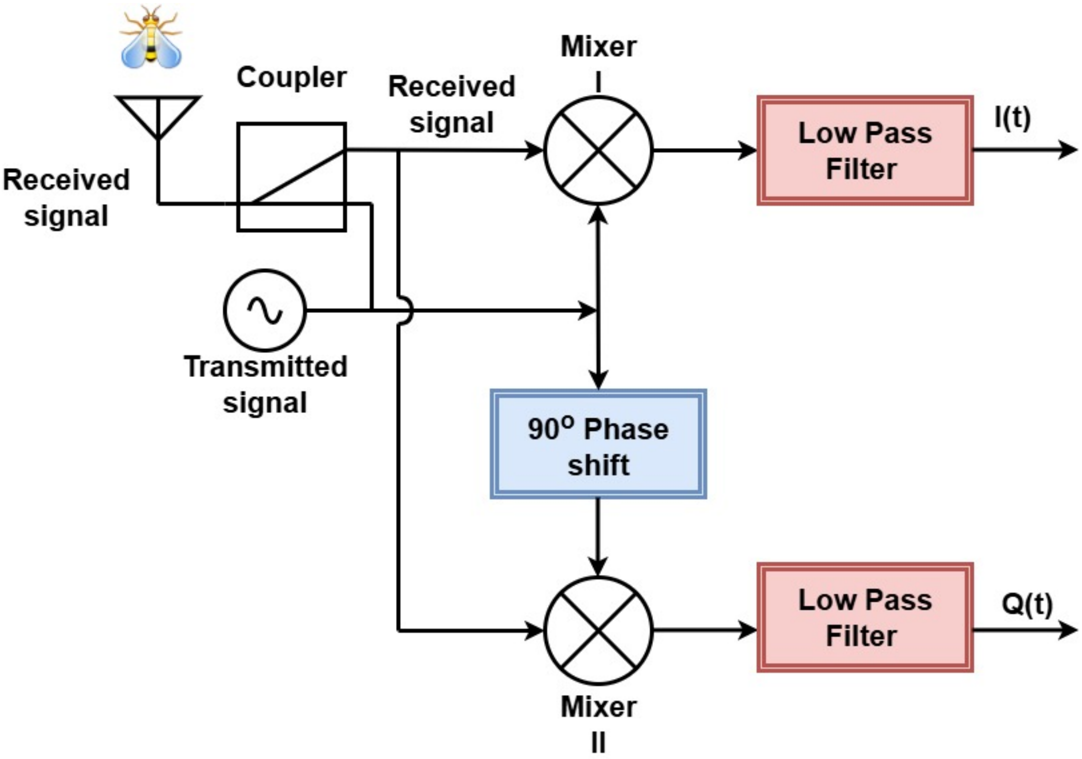

Figure 3.1: Quadrature Detection.

$$\begin{aligned} S(t) &= A\sin(\omega_0 t + \phi)\cdot k\sin(\omega_0 t) \\ &= Ak\sin(\omega_0 t)\left[\sin\phi\cos(\omega_0 t) + \cos\phi\sin(\omega_0 t)\right] \\ &= \frac{kA}{2}\left[\sin(\phi)\sin(2\omega_0 t) + \cos(2\omega_0 t) + \cos(\phi)\right]. \end{aligned}$$

The low-pass filter removes the expressions representing frequencies of $2\omega_0$, and through arranging for k to equal 2 the output of the synchronous detector is:

$$S(t) = A\cos(\phi), \tag{3.2}$$

which is the in-phase, or I-channel, output of the quadrature detector. If the phase of the reference signal fed into the detector is delayed by 90° or $\frac{\pi}{2}$ radians then the output is:

$$\begin{aligned} S(t) &= A\cos\left(\phi - \frac{\pi}{2}\right) \\ &= A\sin(\phi), \end{aligned} \tag{3.3}$$

which is the quadrature, or Q-channel, output. Combining the I and Q outputs, a complex Doppler signal can be formed by

$$\begin{aligned} S(t) &= A\cos(2\pi f_D t) + iA\sin(2\pi f_D t) \\ &= A\cos(2\pi f_D t) + iA\sin(2\pi f_D t) \\ &= Ae^{i2\pi f_D t} \end{aligned} \tag{3.4}$$

Thus, the Doppler frequency shift f_D can be estimated from the complex Doppler signal $S(t)$ by using a frequency measurement tool. To estimate the Doppler frequency shift of a single sinusoidal signal, the periodogram can be used to calculate the spectral density of the signal. Then the maximum likelihood estimation can be applied to locate the maximum of the periodogram.

$$\hat{f}_D = \max_{f_D(k)} \left\{ \left| \sum_{k=1}^{N} A(k) e^{j2\pi f_D(k)} \right|^2 \right\} \tag{3.5}$$

3.3 Micro-Doppler Effect

Micro-Doppler effects describe the Doppler frequency modulations generated by an object's micro-motions, such as oscillatory or small translational movements that are superimposed on its overall motion [73]. For animals, these micro-movements include body dynamics or wing flapping. When a radar signal is reflected from a moving animal, the uniform translational motion produces the main Doppler shift, while the rapid wing motion and other dynamic movements introduce additional time-varying frequency components, referred to as micro-Doppler.

In contrast to conventional mm-wave radar approaches, which are primarily designed for detecting large-scale motion [12], [74] and generally use broad features of the radar return, the micro-Doppler signature represents a species-specific motion pattern, similar to a fingerprint. This enables the identification and characterization of insect species based on their wingbeat frequency and movement patterns.

Micro-Doppler effects appear as characteristic patterns in the time–frequency representation (spectrogram) of the radar return. Figure 3.2 illustrates an example of a micro-Doppler spectrogram generated by an insect's wing flapping. In this representation, harmonic frequency bands can be observed as a result of the insect's periodic wing motion.

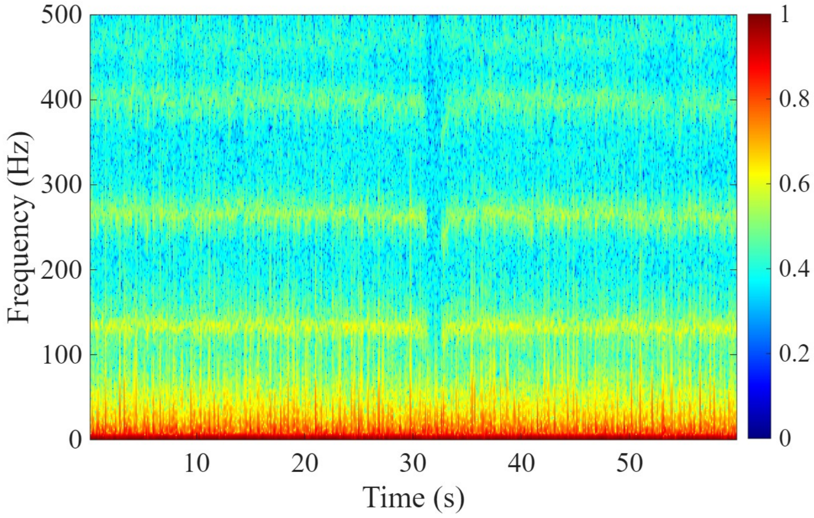

FIGURE 3.2: Micro-Doppler spectrogram of an insect wing flap. Reproduced from [75]

Each wingbeat modulates the reflected signal, producing harmonic components around the primary Doppler frequency.

3.4 Signal Model Relates Micro-Doppler and Wingbeat Frequency

Flying insects generate radar echoes that contain a slowly varying component from the body motion and a rapidly periodic component caused by wing flapping. The received signal can therefore be modeled as the combination of a low-frequency term due to body motion, a higher-frequency wingbeat oscillation, and additive noise. For the general case of an insect flying in front of the antenna, the complex down-converted micro-Doppler signal can be written as:

$$A(t)e^{j\phi(t)} = s_{\text{noise}}(t) + s_{\text{body movement}}(t) + s_{\text{wingbeat}}(t) \tag{3.6}$$

where $s_{noise}(t)$ corresponds to noise, including multiplicative background noise from all non-insect reflective objects; $s_{bodymovement}(t)$ is the Doppler signal originating from the movements of the insect due to its flight pattern; and $s_{wingbeat}(t)$ is the micro-Doppler periodic reflection due to wing movement. Since the latter component is periodic, that is, modulated by the repeated wing movement, it can be expressed as the sum of harmonic signals with the lowest frequency corresponding to the frequency f_w at which the insect moves its wings:

$$s_{\text{wingbeat}}(t) = \sum_{n=1}^{N} A_n exp(2\pi n f_w t + \varphi_n) \tag{3.7}$$

where A_n and φ_n are, respectively, the effective amplitude and phase shift induced by the wing-beating at $(n)^{th}$ harmonic frequency (visualized on Fig. 3.2). Harmonics in the wing–beat micro-Doppler are a direct consequence of the non-rigid motion of the insect wings and how it scatters EM waves. Several non-sinusoidal and multi-component motions occur within one flapping cycle, and each of these introduces additional spectral lines at integer multiples of the f_w. If the motion were a perfect sinusoid with a single rigid reflector, the radar return would contain only one Doppler tone at f_w. Different parts of the wing (e.g., the tip, base, and edges) are located at different ranges from the antenna at each instant and move with different radial velocities. The coherent superposition of the corresponding scattered fields makes the received signal non-sinusoidal, resulting in harmonic components [53], [73].

3.5 Modelling of Micro-Doppler Effect in mm-Wave Antenna Due to Near-Field Insect Fly-By

Prior work in electromagnetic simulation of insects has largely relied on static models, using simplified geometries such as spheres [14], prolate spheroids [15], or ellipsoids [16], which omit the biomechanical motion critical for generating micro-Doppler signatures. While anatomically informed static models improve RCS fidelity over generic shapes [17], they do not account for the temporal dynamics introduced by wingbeat and body motion. To bridge this gap, we introduce a dynamic 3D insect model incorporating both wing-flapping and translational movement, enabling simulation of time-varying electromagnetic interactions with mmWave antennas.

The numerical analysis is carried out using the Finite Integration Technique (FIT) solver in CST Microwave Studio. The simulated scenario includes a wideband horn antenna operating in the 10−40 GHz frequency range. The antenna has an aperture of $H_a \times W_a = 28.85 \times 21.13$ mm^2, a rectangular throat of $H_g \times W_g = 15.10 \times 4.36$ mm^2, and

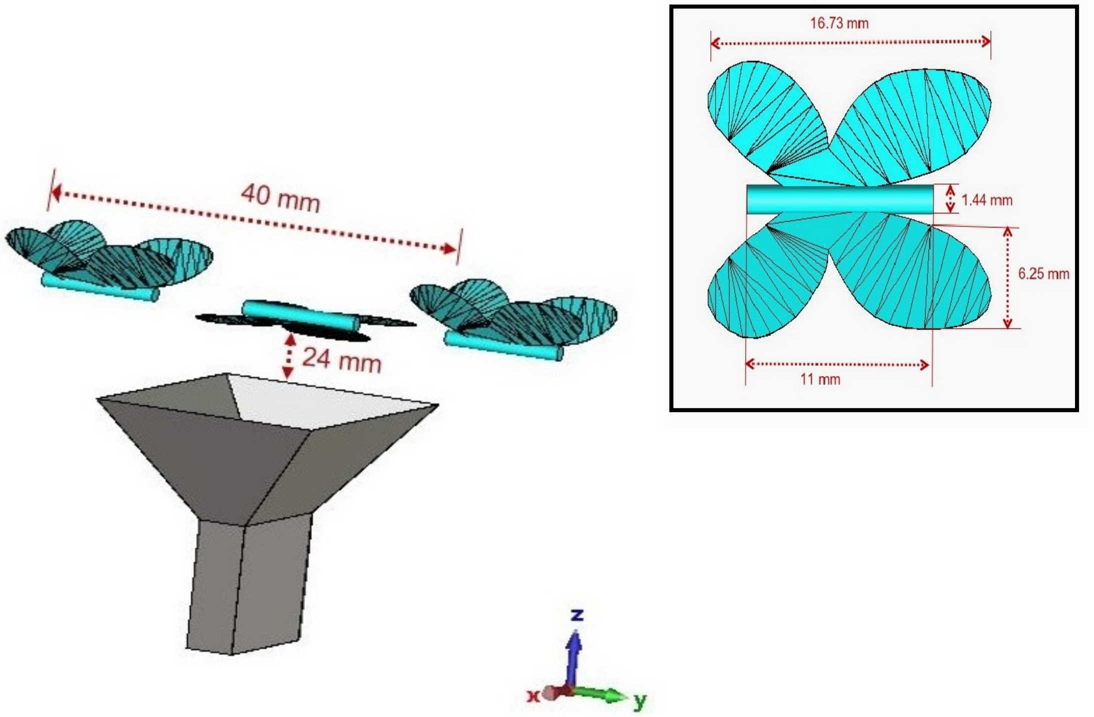

FIGURE 3.3: Simulated model with key dimensions. Reproduced from [72]

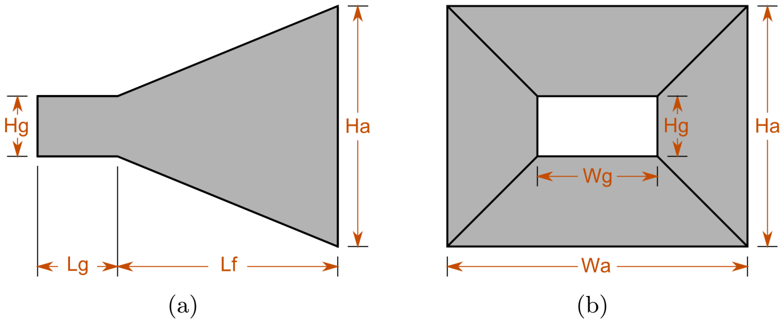

(a) (b)

FIGURE 3.4: Metallic horn antenna: (a) Side view and (b) Front view.

a waveguide feed with length $L_g = 12.4$ mm, as illustrated in Fig. 3.4. The antenna is modeled using Perfect Electric Conductor (PEC) material to reduce simulation time, with negligible impact on accuracy.

The insect target is represented as a solid 3D model, shown in the inset of Fig. 3.3. The model moves linearly in front of the antenna while simultaneously flapping its wings. The insect's body is modeled as a cylindrical structure measuring 11 mm in length and 1.44 mm in diameter. The wings are modeled with dimensions of 16.73 mm in length and 6.25 mm in width. The dielectric constant (ε_r) and loss tangent ($\tan\delta$) of the insect are taken as 34.3 and 18.6, respectively [65]. The wing motion is modeled as a ±45° sweep from the planar rest position. The relationship between the insect's translational motion

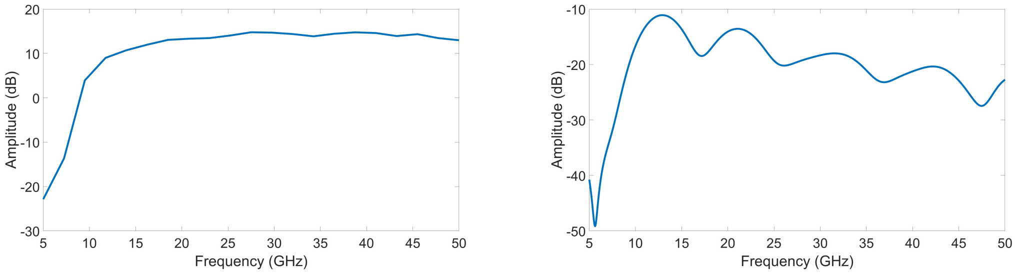

(a) (b)

Figure 3.5: Antenna performance in free space (no insect): (a) Magnitude of boresight antenna gain as a function of frequency and (b) Reflection coefficient (S_{11}) of the antenna as a function of frequency.

and wing flapping is obtained by calculating the wing angle $\alpha(d_y)$ at each position d_y as:

$$\alpha(d_y) = Acos\left(2\pi f_w \frac{d_y}{v}\right) \tag{3.8}$$

where $A = 45°$ denotes the maximum angular position of the wings, f_w is the WBF, d_y represents the position of the insect along the Y-axis, and v is its forward flight velocity. The forward velocity and WBF are selected as 1 m/s [76] and 200 Hz [77], respectively, values that are reported in the literature for small insects. The motion is evaluated along the Y-axis from −20 mm to +20 mm, as shown in Fig. 3.3. The minimum distance between the insect and the antenna aperture occurs at $d_y = 0$, corresponding to 24 mm separation.

Fig. 3.5(a) and Fig. 3.5(b) show, respectively the simulated gain at boresight and the reflection coefficient in free space, i.e., without the insect. It can be seen that the antenna operates within the whole bandwidth of interest, with stable gain ranging between 10-15 dBi, which is typical for horn antenna designs.

Fig. 3.6 and Fig. 3.7 presents a comprehensive analysis of the impact of insect hovering (just wing flapping motion without translation motion) near an antenna, capturing both the antenna gain and S_{11} over time, and their corresponding power spectral densities. Fig. 3.6 illustrates the phase, amplitude, and power spectrum of the antenna gain, respectively. Similarly, depict the amplitude, phase, and power spectrum of the reflection coefficients. In both the S_{11} and gain measurements, clear periodic fluctuations are observed in the time-domain amplitude and phase plots. These oscillations are the result of the insect's wing movements modulating the electromagnetic environment around the antenna. As the insect hovers, its flapping wings periodically scatter and reflect the incident electromagnetic

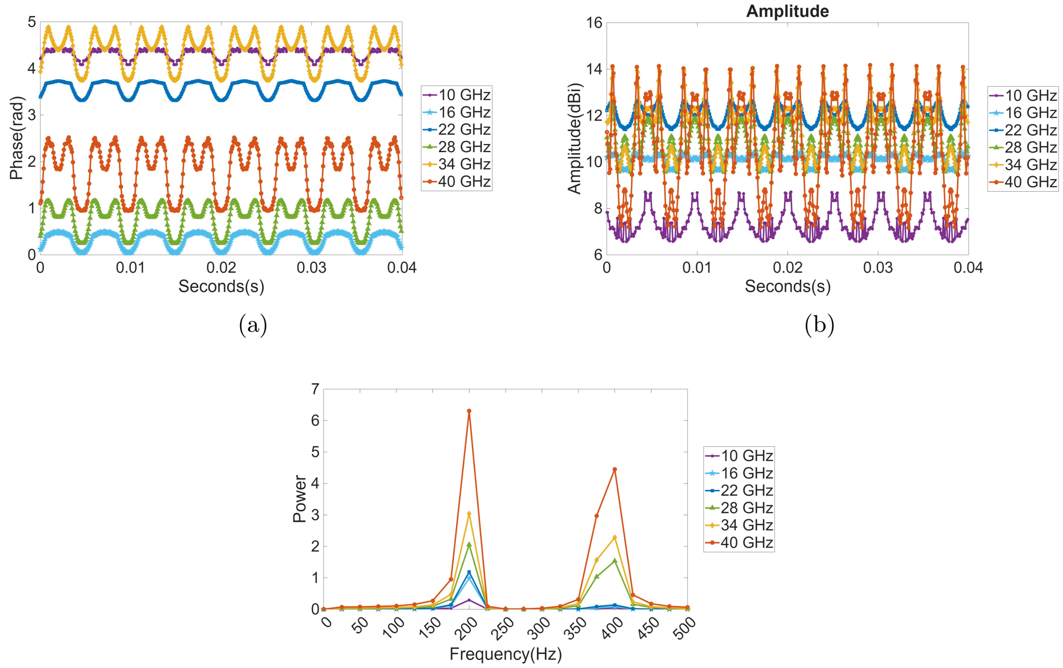

(a) (b)

(c)

FIGURE 3.6: Antenna gain at boresight during insect wing flapping: (a) Phase of the antenna gain, (b) Amplitude of the antenna gain (linear), (c) Gain spectrum

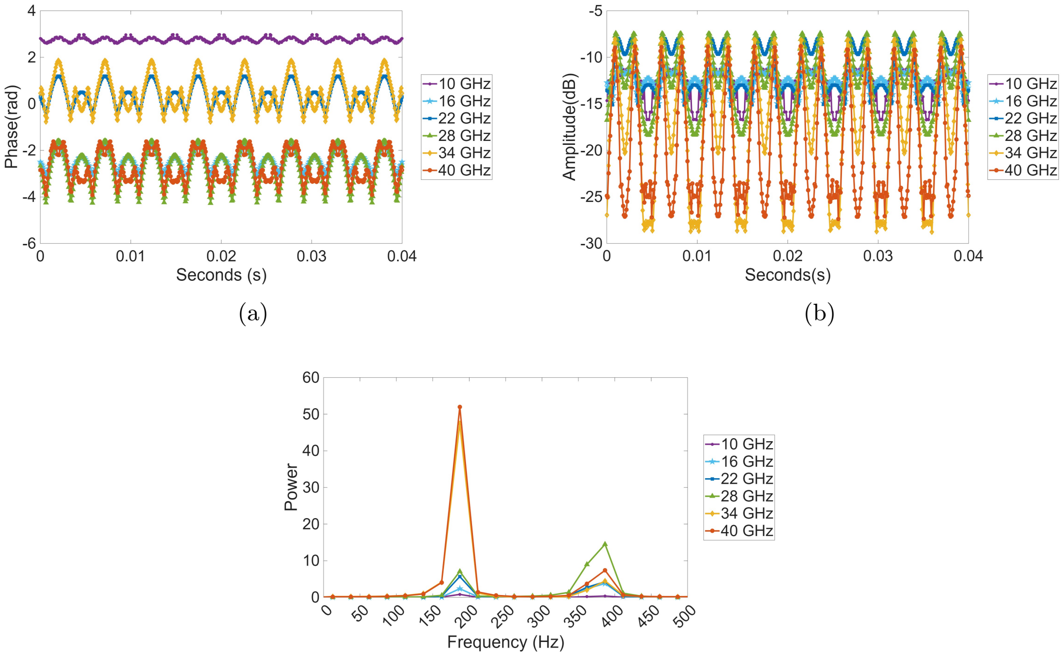

(a) (b)

(c)

FIGURE 3.7: S_{11} at boresight during insect wing flapping: (a) Phase of the S_{11}, (b) Amplitude of the S_{11} (linear), (c) S_{11} spectrum.

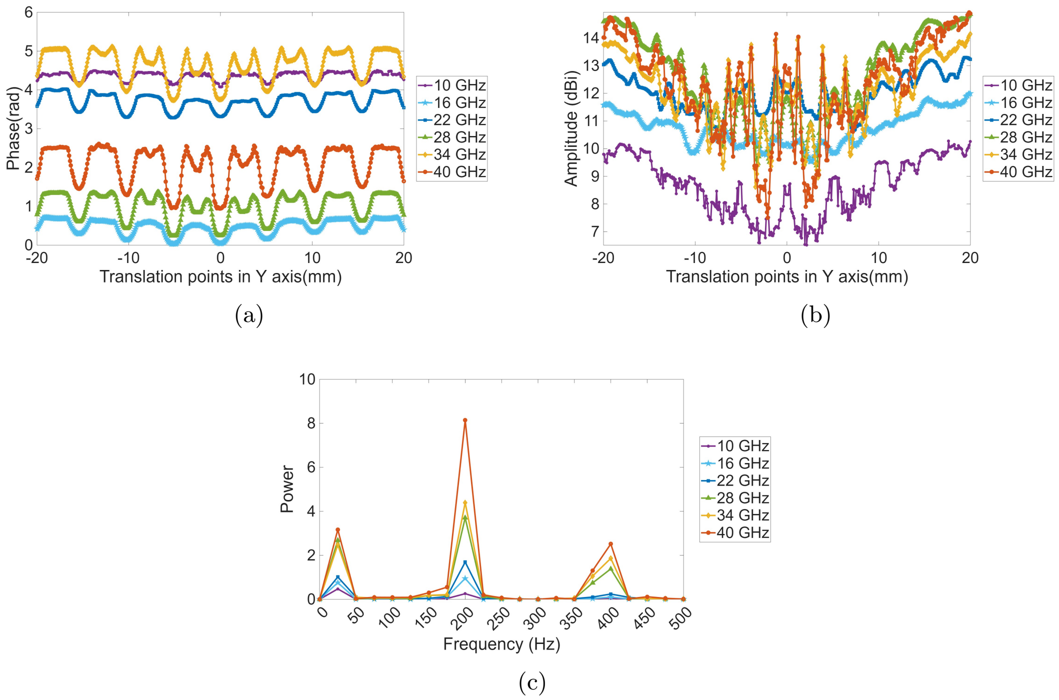

(a) (b) (c)

Figure 3.8: Antenna gain at boresight during insect wing flapping and translation motion: (a) Phase of the antenna gain, (b) Amplitude of the antenna gain (linear), (c) Gain spectrum. Reproduced from [72]

waves, leading to time-varying distortions in both the reflected signal and the antenna's effective radiation characteristics.

Notably, the power spectral analysis in Fig. 3.6(c) and Fig. 3.7(c) reveals distinct spectral peaks at 200 Hz and 400 Hz for both the reflection coefficients and the gain. The 200 Hz peak corresponds precisely to the modeled wing flapping frequency of the insect, confirming that the periodicity observed in the time-domain data is directly linked to the flapping motion. The second harmonic at 400 Hz arises from symmetric wing motion.

The magnitude of these fluctuations varies with frequency. Higher frequencies, such as 40 GHz, exhibit more pronounced oscillations, suggesting increased sensitivity to small-scale motion like wingbeats. In contrast, lower frequencies show smoother, less intense variations.

Fig.3.8(a) and Fig.3.8(b) depict respectively the periodic variations in phase and amplitude of the antenna gain during insect's fly-by(insect posses both wing flapping motion and translation motion), while Figs.3.9(a) and Fig.3.9(b) depict same effect for the S_{11}. Once the insect crosses antenna's main beam (from -10 mm to 10 mm), it creates noticeable fluctuations to gain and S_{11}. A partial signal blockage causes drop in gain that is

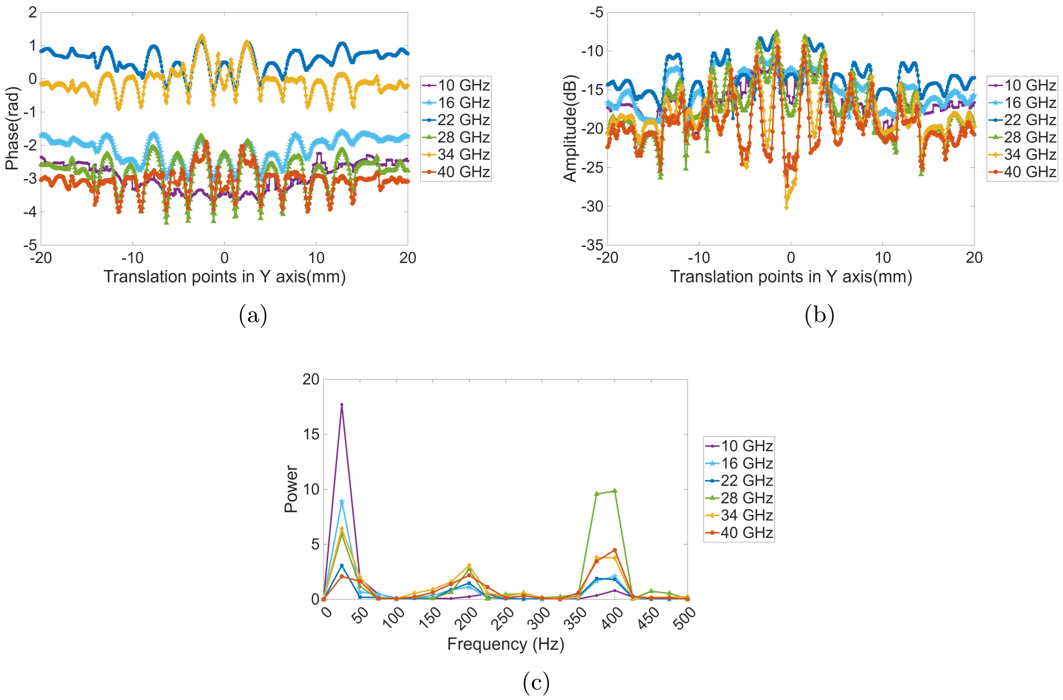

(a) (b)

(c)

FIGURE 3.9: S_{11} at boresight during insect wing flapping and translation motion: (a) Phase of the S_{11}, (b) Amplitude of the S_{11} (linear), (c) S_{11} spectrum. Reproduced from [72]

modulated by the insect's WBF pattern. For the same locations, the S_{11} increases due to increased reflection from the insect's body that is also modulated by the same WBF. As the effective area of the insect increases as the operating wavelength lowers, the higher frequencies are more able for the proposed detection mechanism.

Fig. 3.8(c) and Fig. 3.9(c) illustrates the power spectral analysis of the gain and S_{11}. A peak around 25 Hz can be observed, which is due to the insect's translation motion. Another peak at 200 Hz correspond to the simulated insect's WBF, followed by harmonic peaks at 400 Hz. Since the WBF is correlated with insect's size, its measurement is a first step to insect identification and corresponding biodiversity analysis.

3.6 Micro-Doppler Effects in Flying Insects: Experimental Verification

3.6.1 Measurement Setup and Experimental Protocol

Figure 3.10(a) illustrates the experimental setup. A mmWave broadband horn antenna (BBHA 9170) transmits a CW signal generated by a Rohde & Schwarz Vector Network

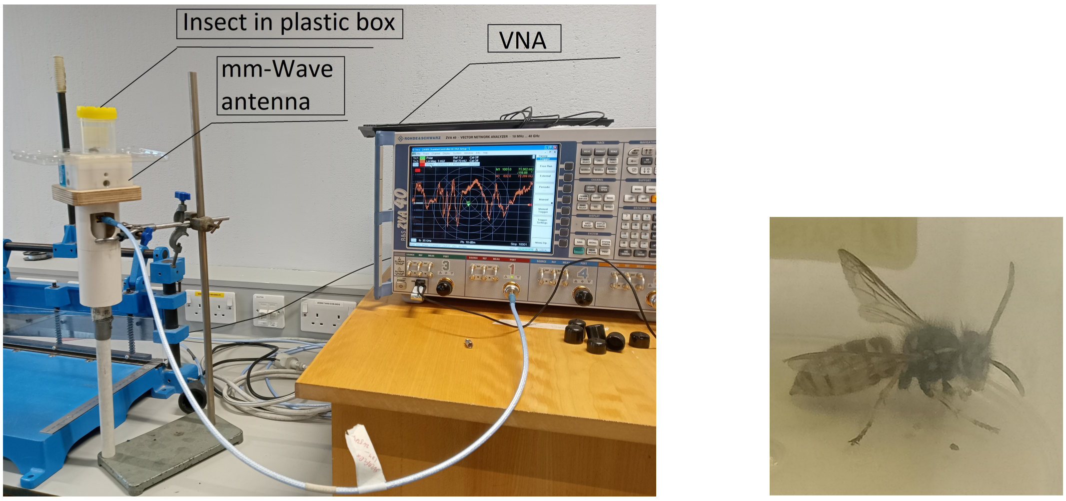

(a) Experimental setup (b) *Vespula vulgaris*

Figure 3.10: Methodology: (a) Experimental setup; (b) One of the investigated insects (*Vespula vulgaris*). Reproduced from [75]

Analyzer (VNA) and records the corresponding backscattered response. The reflection coefficient S_{11} was measured over a duration of 10 s, yielding 10,001 samples of amplitude and phase. Ethical approval for the study was obtained from the Ethics Committee of the School of Natural Sciences, Trinity College Dublin.

Live insects belonging to the order *Hymenoptera* were collected on the Trinity College Dublin campus and individually placed in small cylindrical plastic containers (4 cm in diameter and 5 cm in height). Each container was positioned on a plastic support above the mmWave antenna. The containers permitted natural wing motion while having a negligible effect on the measured backscattered signal. Synchronized video recordings were acquired to provide a coarse temporal reference for annotating wing activity during the measurements.

3.6.2 Frequency Sensitivity Analysis: 10 GHz vs. 40 GHz

Figure 3.11 illustrates the effect of an insect on the radar return amplitude at two different operating frequencies: 10 GHz and 40 GHz. In Fig. 3.11(a), both traces (with and without the insect) remain relatively flat, indicating limited sensitivity to the insect at 10 GHz.

In contrast, Fig. 3.11(b) shows a clear difference at 40 GHz. While the no-insect signal is stable, the presence of the insect produces distinct fluctuations in amplitude. This confirms that higher mm-wave frequencies offer greater sensitivity to small targets such as flying insects.

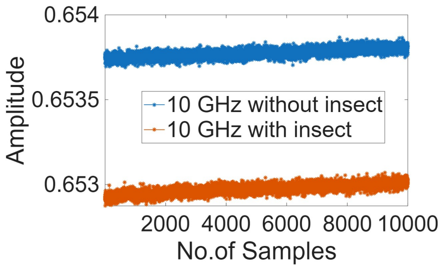

(a)

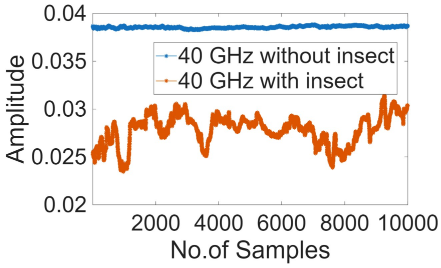

(b)

FIGURE 3.11: Amplitude variation of radar signals at (a) 10 GHz and (b) 40 GHz frequencies with and without the presence of an insect.

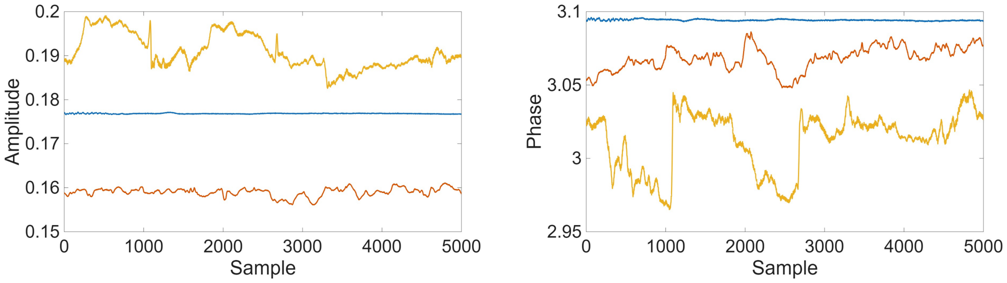

(a) (b)

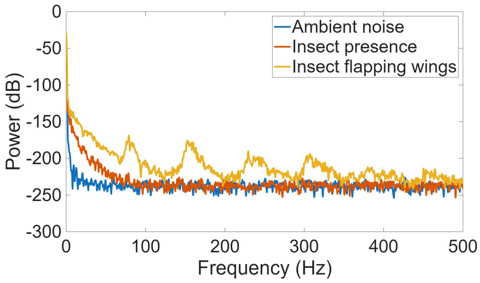

(c)

FIGURE 3.12: Time and frequency domain responses of a radar system detecting insect activity. (a) Amplitude variation, (b) phase variation, and (c) power spectral density across three scenarios: ambient noise (blue), insect presence (orange), and insect with flapping wings (yellow).

3.6.3 Rationale for 30 GHz Operation and Sampling Rate

To further explore a system model capable of capturing object dynamics through time-varying frequency and Doppler shifts for pollinator monitoring, a frequency of 30 GHz and a sampling rate of 1 kHz were selected. This frequency provides a balance between sensitivity and propagation attenuation.

Most pollinating insects exhibit wingbeat frequencies in the range of approximately 100–200 Hz. Based on the Nyquist criterion, a 1 kHz sampling rate is sufficient to capture signals up to 500 Hz, leaving adequate margin for detecting wingbeat harmonics and more complex motion components.

3.6.4 Experimental Results at 30 GHz

Figure 3.12 shows the S_{11} responses at 30 GHz and 1 kHz sampling rate under three experimental conditions: (i) insect absence (noise floor), (ii) insect present but stationary, and (iii) active wing flapping. The results are presented using amplitude, phase, and power spectrum representations.

Noise Floor: Insect Absent

In the absence of any insect, the mm-wave signal remains steady with flat amplitude and phase response. The corresponding spectrum shows negligible power, representing the nominal noise floor of the measurement.

Stationary Insect: No Wing Motion

When the insect is present but not flapping its wings, subtle amplitude variations are observed. These small fluctuations slightly increase the received signal power, enabling detection of the insect even in stationary conditions. The phase response remains largely stable but exhibits minor drifts. The spectrum shows a noticeable increase in power at low frequencies (below ~ 50 Hz), clearly differentiating this case from the noise-only scenario. This broadband elevation confirms that even a stationary insect introduces low-frequency dynamics detectable by the mm-wave signal.

Active Wing Flapping: Micro-Doppler Signatures

With the insect actively flapping its wings, the mm-wave response becomes strongly time-varying. Pronounced periodic modulations are observed in both the amplitude and phase signals. The spectrum exhibits distinct harmonic peaks corresponding to the WBF and its higher-order harmonics, confirming the presence of micro-Doppler features induced by wing motion.

3.6.5 Impact of Environmental Clutter on Insect Wing Flap

In the time domain, clutter appears as high-amplitude, slowly varying components that can mask the much weaker reflections from insects. Wind-driven vegetation motion, such as moving branches or grass, creates low-frequency fluctuations in amplitude, producing a slowly varying baseline. Airborne clutter, including drifting leaves or birds, produces short transient peaks when they enter the radar beam. In contrast, insect wingbeats generate fast, quasi-periodic modulations in both amplitude and phase, resulting in clear micro-Doppler features.

In the frequency domain, insect wing motion produces distinct spectral components at the WBF and its harmonics. Clutter, on the other hand, concentrates energy near zero Doppler. Static or very slow objects (e.g., ground or tree trunks) contribute a strong DC component, while vegetation motion broadens the spectrum around low frequencies, often forming an exponential-like decay near 0 Hz. Bird wingbeats may introduce low-frequency micro-Doppler signatures (typically 2–20 Hz), but these remain well separated from the higher-frequency components produced by insects [78]. Consequently, clutter dominates the low-frequency region, whereas insects introduce higher-frequency signatures characteristic of wing motion.

Figure 3.12(c) compares the amplitude spectra for ambient noise, insect presence, and active wing flapping. A strong component at 0 Hz corresponds to ambient noise, while the wing-flapping case shows symmetric peaks at the WBF. The noise floor acts as the baseline for these spectra, reflecting sensor and environmental noise, and may reduce the visibility of spectral peaks when sufficiently high.

3.7 Summary

This chapter introduced the fundamental principles of the Doppler and micro-Doppler effects and developed a theoretical framework for describing the micro-Doppler signatures generated by flying insects. Based on this formulation, a dynamic insect model was proposed to investigate how wingbeat-induced motion influences the antenna response in the near-field. Electromagnetic simulations were used to evaluate the impact of the insect's periodic wing motion on the antenna gain and reflection coefficient (S_{11}) as the insect passes near the antenna aperture.

The simulation results showed that insect wingbeats produce characteristic periodic fluctuations in both S_{11} and gain, directly corresponding to the WBF and its harmonic structure. To validate these findings, experiments were performed using live insects. The measurements demonstrated that a 30 GHz radar system sampled at 1 kHz can reliably distinguish between three cases: no insect, stationary insect, and active wing flapping. Notably, even when the insect is stationary, small signal modulations are observable, indicating that the radar is sensitive to subtle biological dynamics beyond overt wing motion.

Since different insect species exhibit distinct wingbeat frequencies and motion patterns, the resulting harmonic composition of $s_{\text{wing beat}}(t)$ forms a species-specific motion signature. The following chapters show that these spectral features can be extracted and used for automatic identification and classification of insects. Different insect species exhibit distinct wing movement patterns, which can be seen in the harmonic spectrum of $s_{\text{wing beat}}(t)$, as demonstrated in the following chapters.

Chapter 4

Micro-Doppler Feature Extraction and Analysis

This chapter presents the development and analysis of an automated signal processing framework for isolating micro-Doppler activity. By automatically identifying and segmenting relevant signal portions, the framework provides a structured foundation for subsequent feature extraction and machine learning-based classification.

To guide the feature extraction strategy, the temporal and spectral signatures of wing-flapping micro-Doppler signals were first examined for two representative pollinator species: *Bombus terrestris* and *Apis mellifera*. To quantitatively describe these patterns, the micro-Doppler–active signal segments were analyzed to extract temporal, harmonic, spectral, and band power features. These features provide a compact and informative representation of key signal properties, including oscillation rates, frequency content, harmonic structure, and energy distribution across Doppler frequencies. The feature analysis explained in this chapter was presented at [79]. These observations establish a clear spectral and temporal basis for subsequent step toward automated, species-level insect monitoring using radar sensing.

4.1 Wingbeat-Induced Micro-Doppler Signal Segments Selection

Processing continuously recorded signal data for real-time insect detection presents a significant computational challenge, as it requires analyzing large volumes of raw signals and

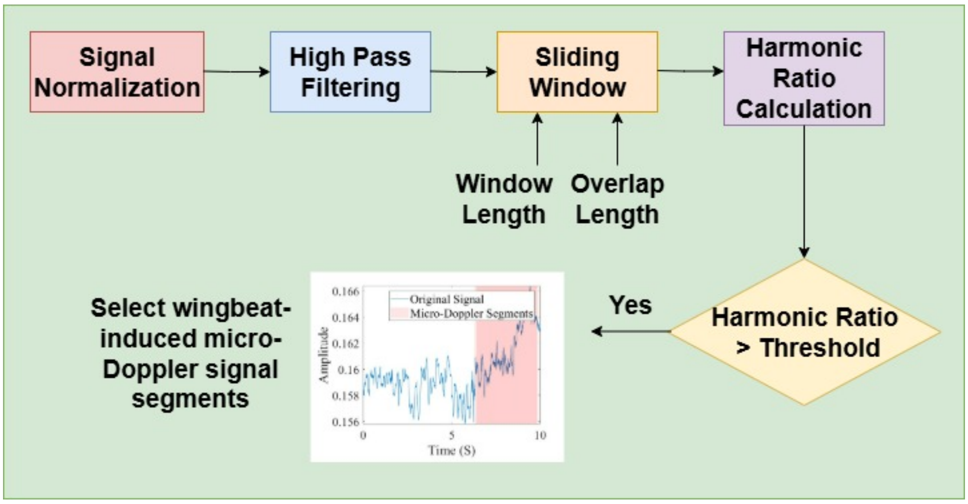

FIGURE 4.1: Wingbeat-induced micro-Doppler signal segments.

spectrograms. To address this, the proposed automated detection framework isolates relevant micro-Doppler segments, reducing manual inspection and facilitating future machine learning-based insect identification. Insect wing flapping is characterized by patterns of harmonics in the signal. This periodic structure allows the determination of whether or not a signal segment has a micro-Doppler contribution due to the presence of insects. For this, a micro-Doppler segment extraction algorithm is implemented as depicted in Figure. 4.1. The signal is first normalized to reduce the effects of noise. Then, it is high-pass filtered using a 2nd-order Chebyshev high-pass filter with a cut-off frequency of 50 Hz to remove slow-moving background noise. This choice of filter frequency was based on the reported wing-beat frequency of insect pollinators, which is typically above 50 Hz [80].

The mmWave signal is segmented into overlapping frames using a 2 s Hann window with a 1 s overlap. The selected window length ensures that multiple wingbeat cycles are captured within each frame. The use of a Hann window reduces spectral leakage and improves the reliability of frequency-domain feature extraction. A 50% overlap is employed to avoid loss of transient micro-Doppler events at frame boundaries and to increase the number of valid samples without introducing significant redundancy. For each frame, a harmonic ratio is computed to quantify the degree of periodicity present in the signal. The harmonic ratio reflects the relative contribution of harmonic components to the total signal energy and is derived from the normalized autocorrelation function, which measures the similarity between a signal segment and its time-shifted versions [81].

Given a signal frame x of length L, the normalized autocorrelation $\Psi(k)$ is evaluated

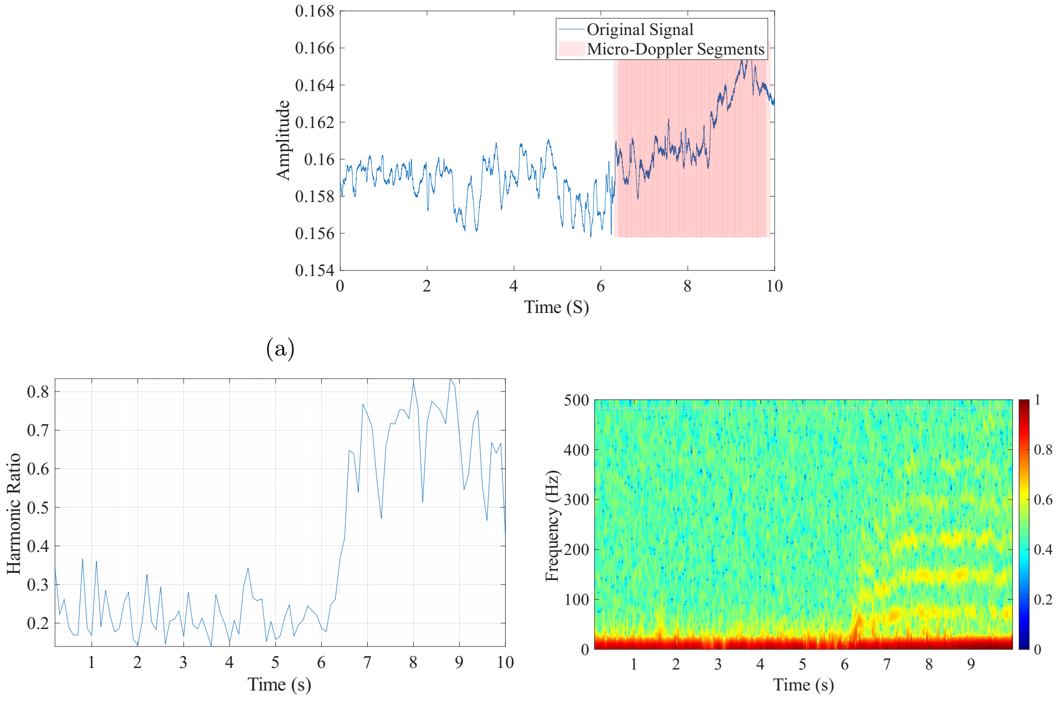

(a)

(b)

(c)

FIGURE 4.2: Example of micro-Doppler segment extraction from an insect radar signature. The insect remains stationary for the first 6 s, after which flight begins, as confirmed by video. (a) Raw signal with the micro-Doppler segment highlighted. (b) Harmonic ratio over time, increasing sharply with the onset of wing flapping. (c) Short-Time Fourier Transform (STFT) spectrogram showing periodic micro-Doppler bands between 6 and 10 s.

for each lag k, and the harmonic ratio η_{HR} is defined as the maximum value of $\Psi(k)$ over a predefined lag interval $[K_0, K]$. Higher harmonic ratio values indicate a stronger periodic structure, making this metric well suited for detecting micro-Doppler effects caused by repetitive motions such as insect wing flapping. Signal frames with a harmonic ratio exceeding a predefined threshold (0.4) are therefore retained for further analysis. A threshold of 0.4 was selected empirically as a trade-off between retaining weak but valid insect micro-Doppler signatures and rejecting noise-dominated or non-periodic segments. This value was found to provide consistent separation between insect flight activity and background clutter under the present measurement conditions

As shown in Fig. 4.2, the insect remained stationary during the first 6 s, resulting in harmonic ratio values below 0.4. At approximately 6 s, the onset of hovering behavior led to a noticeable increase in the harmonic ratio, accompanied by the emergence of periodic micro-Doppler patterns in the spectrogram. This behavioral transition was confirmed by the corresponding video footage.

4.2 Observed Signal Patterns and Feature Analysis Motivation

The temporal and spectral signatures shown in Fig. 4.3 illustrate the characteristic differences in radar backscatter generated by wing-flapping insects. The raw time-domain signals capture the overall oscillatory energy associated with wing motion, while the high-pass filtered segments isolate the fast variations corresponding to micro-Doppler components induced by wingbeat. The accompanying spectrograms reveal clear harmonic structures, with the *B. terrestris* exhibiting lower fundamental frequencies and slightly more concentrated harmonic energy around the fundamental and its harmonics. Whereas *A. mellifera* shows higher wingbeat frequencies and a broader energy distribution across frequencies. To quantitatively describe these patterns, the micro-Doppler–active signal segments were analyzed to extract discriminative features that reflect the underlying temporal and spectral characteristics of wingbeat dynamics.

4.3 Micro-Doppler Feature Extraction and Analysis

This study aims to capture micro-Doppler patterns by extracting harmonic, spectral, and temporal features from the detected signal segments obtained from three individuals each of *A. mellifera* and *B. terrestris.* In total, 254 micro-Doppler segments were extracted for *A. mellifera* and 277 for *B. terrestris.* To the best of our knowledge, this is the first study to quantitatively characterise these complementary feature domains from active micro-Doppler signal segments in order to represent different aspects of insect wingbeat dynamics. This provides sufficient samples for feature-level statistical analysis, while highlighting the need for future measurements on a larger population to improve generalisability.

4.3.1 Harmonic Features

Harmonic features characterize the periodic structure of the radar signal produced by wing flapping. Periodic wing motion creates a distinct harmonic pattern in both the time and frequency domains, which can be used to estimate fundamental wingbeat frequency and quantify signal periodicity.

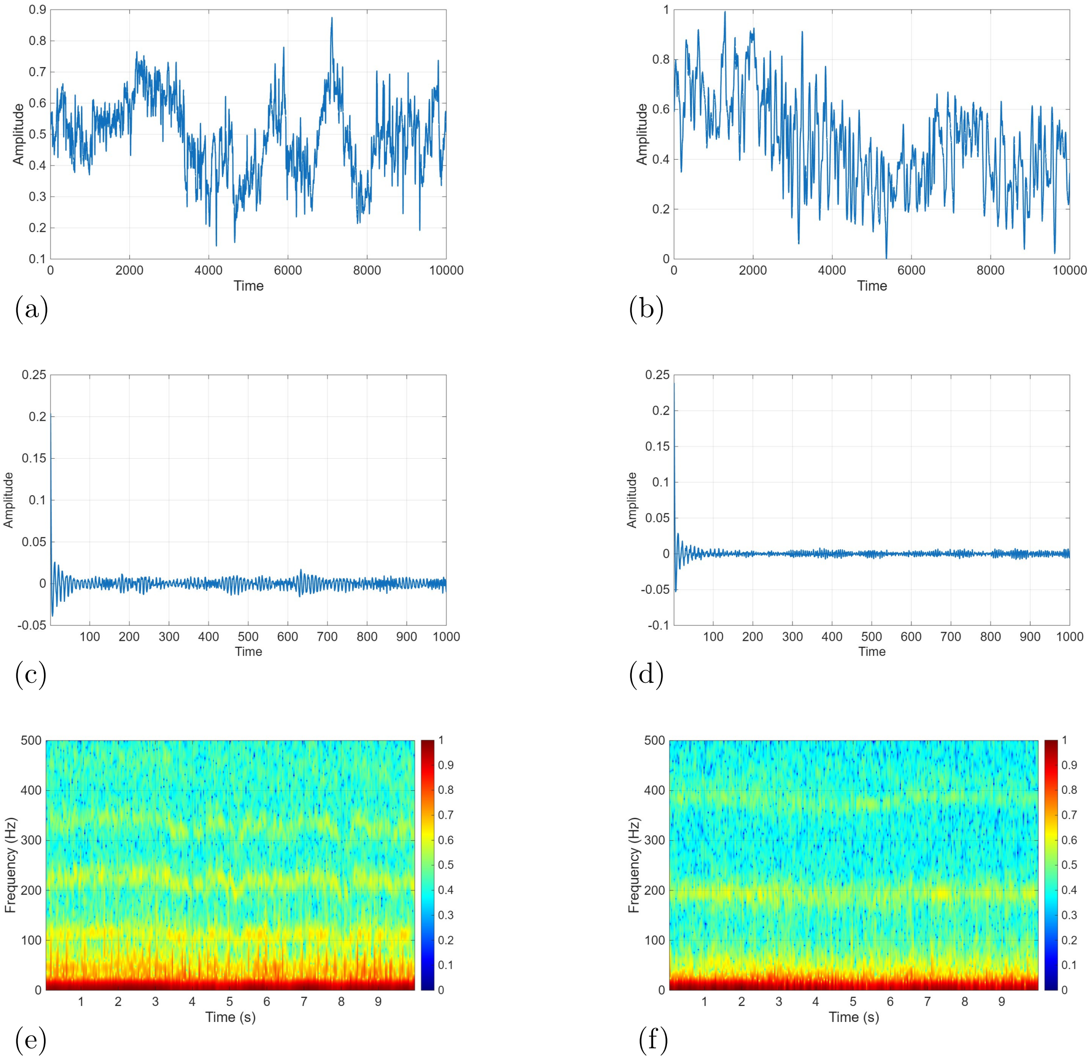

(a) (b) (c) (d) (e) (f)

Figure 4.3: Temporal and spectral characteristics of wing-flapping micro-Doppler signals from *Bombus terrestris* (left) and *Apis mellifera* (right). (a–b) Raw reflected signal amplitude over the full observation window. (c–d) High-pass filtered segments of the first 1 s, isolating wingbeat-induced micro-Doppler after background removal. (e–f) Spectrograms highlighting the fundamental and harmonic bands; *B. terrestris* exhibits a lower fundamental frequency, whereas *A. mellifera* shows higher wingbeat frequency.

1. Harmonic Ratio.

The Harmonic Ratio (η_{HR}) is a measure of the periodicity of the signal. Autocorrelation can be used to calculate the harmonic ratio by taking a short fragment of the signal and comparing it with future samples. The normalized autocorrelation function $\Psi(k)$ can be expressed as:

$$\Psi(k) = \frac{\sum_{i=1}^{L} x(i)x(i-k)}{\sqrt{\sum_{i=1}^{L} x(i)^2 \sum_{i=0}^{L} x(i-k)^2}} \quad \text{for } 1 \leq k \leq K \tag{4.1}$$

where x is a single frame of signal with L elements and K is the maximum lag in the calculation. The harmonic ratio η_{HR} is determined as the maximum value of the normalized autocorrelation within the given range [81]:

$$\eta_{HR} = \max_{K_0 \leq k \leq K} \{\Psi(k)\} \tag{4.2}$$

η_{HR} represents how strongly the signal repeats itself over time. A high harmonic ratio indicates clean, periodic wingbeats with strong harmonic structure, while lower values reflect more irregular motion. Because it relies on time-domain autocorrelation, this feature is less affected by amplitude variations. As shown in the Fig. 4.4, *B. terrestris* exhibits higher harmonic ratio values than *A. mellifera*, reflecting stronger and more stable harmonic components. This stems from flight biomechanics: bumblebees, with lower wingbeat frequencies and steadier flight, generate more regular Doppler harmonics.

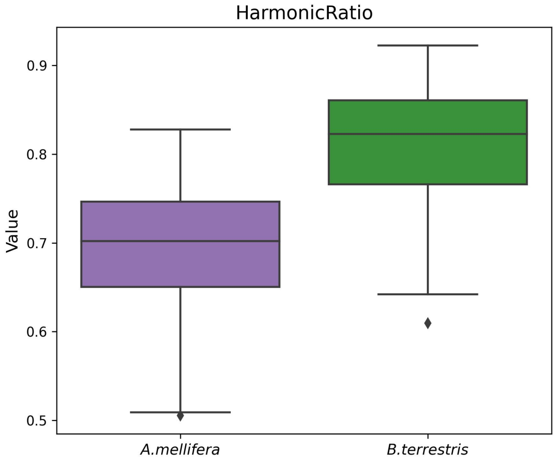

FIGURE 4.4: Harmonic ratio distribution for *A. mellifera* and *B. terrestris*.

2. Fundamental Frequency (STFT_F0).

The fundamental frequency $\hat{f}_0$ is estimated from the Doppler spectrum using a Welch-type periodogram. In this method, 39% of the available samples in each frame are used per segment to compute the averaged power spectrum:

$$\hat{S}(f) = \frac{1}{M} \sum_{m=1}^{M} \frac{1}{U} \left| X_m(f) \right|^2,$$

where $X_m(f)$ is the short-time Fourier transform of segment m, U is a normalization factor, and M is the number of segments.

The fundamental frequency is identified as the location of the lowest-frequency peak among the six strongest peaks:

$$\hat{f}_0 = \min\{f_{\text{peak},i}\}, \qquad i \in \{1, \ldots, 6\}.$$

The Welch method provides a smoothed spectral estimate that is less sensitive to noise compared to a single FFT. By selecting the lowest dominant peak, $\hat{f}_0$ corresponds to the fundamental wingbeat frequency, while the remaining peaks at integer multiples correspond to harmonics. Fig. 4.5 indicates a clear difference in $\hat{f}_0$ between the two species. *A. mellifera* shows higher $\hat{f}_0$, while *B. terrestris* displays lower $\hat{f}_0$. This pattern is consistent with the general tendency for smaller insects to have higher wingbeat frequencies, whereas larger insects typically flap more slowly.

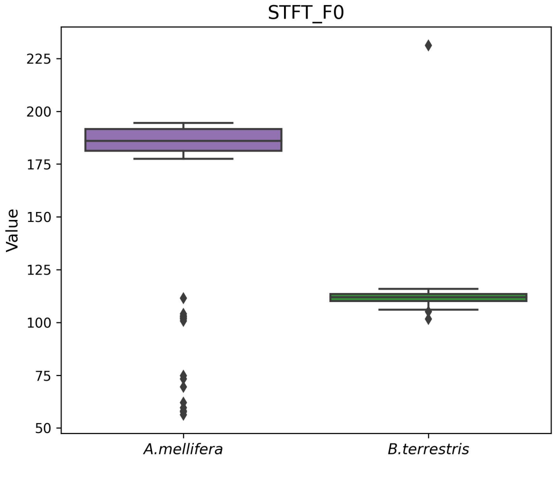

FIGURE 4.5: STFT_F0 distribution for *A. mellifera* and *B. terrestris*.

4.3.2 Temporal Features

Temporal features describe properties of the signal directly in the time domain. They are particularly useful for capturing the overall activity level and oscillatory behavior produced by insect wingbeats before moving into spectral analysis. While simple, these features often carry strong discriminative information and complement the spectral analysis.

1. Zero-Crossing Rate (ZCR)

The ZCR measures how frequently the signal waveform crosses the zero-amplitude axis within a given frame:

$$\text{ZCR} = \frac{1}{N-1} \sum_{n=1}^{N-1} \mathbf{1}\Big(\text{sign}(x[n]) \neq \text{sign}(x[n-1])\Big),$$

where $\mathbf{1}(\cdot)$ is the indicator function.

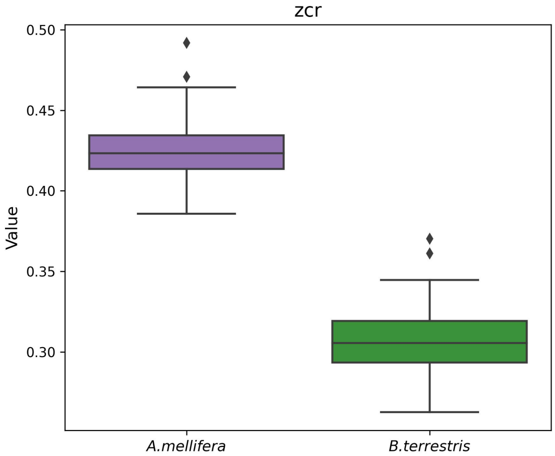

Figure 4.6: ZCR distribution for *A. mellifera* and *B. terrestris*

Fig. 4.6 shows that *A. mellifera* exhibits higher ZCR compared to *B. terrestris*. Higher ZCR values reflect more rapid fluctuations in the signal, which are typically associated with higher wingbeat frequencies and faster oscillatory motion. In contrast, the lower ZCR values observed for *B. terrestris* are consistent with slower wingbeat rates and less frequent signal oscillations. This difference aligns with the expected relationship between insect body size, wingbeat frequency, and temporal signal characteristics.

2. Root Mean Square Energy (RMS) Energy (RMS Energy)

The RMS Energy quantifies the overall energy content of the signal:

$$\mathrm{RMS} = \sqrt{\frac{1}{N}\sum_{n=0}^{N-1}|x[n]|^2}.$$

RMS Energy measures the signal's magnitude over time, reflecting the strength of the radar return caused by insect motion. Fig. 4.7 shows that *B. terrestris* has higher RMS energy values compared to *A. mellifera*. This is consistent with the expectation that larger insects or those producing stronger radar reflections generate higher signal energy. In contrast, the lower RMS energy observed for *A. mellifera* likely reflects its smaller body size and consequently weaker backscatter.

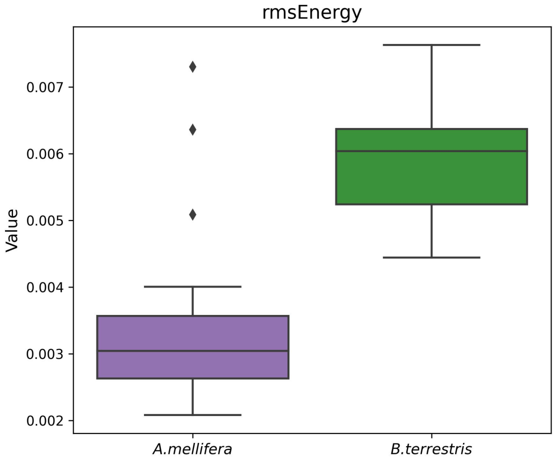

FIGURE 4.7: RMS Energy distribution for *A. mellifera* and *B. terrestris*

4.3.3 Spectral Features

Spectral features describe the distribution and variation of signal energy across frequency. For radar-based insect detection, these features capture how the wingbeat-induced micro-Doppler energy is structured in the frequency domain.

Let the short-time complex radar signal be $x[n] = I[n] + jQ[n]$, windowed by $w[n]$ of length N and sampled at rate F_s. The discrete Fourier transform (DFT) and corresponding power spectrum are:

$$X[k] = \sum_{n=0}^{N-1} x[n]w[n]e^{-j2\pi kn/N}, \qquad P[k] = \frac{1}{N}|X[k]|^2,$$

where $f[k] = kF_s/N$ is the Doppler frequency bin. The normalized spectrum is defined as $\tilde{P}[k] = P[k]/\sum_k P[k]$.

1. Spectral Centroids

The spectral centroids represents the frequency "center of gravity" of the power spectrum [82]:

$$C = \frac{\sum_k f[k]P[k]}{\sum_k P[k]},$$

where $P[k]$ is the power spectrum and $f[k]$ is the Doppler frequency corresponding to the k-th spectral bin.

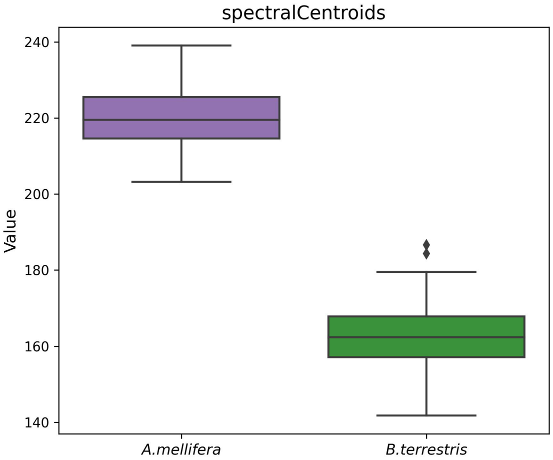

Figure 4.8: Spectral Centroid distribution for *A. mellifera* and *B. terrestris*

Fig. 4.8 shows that *A. mellifera* exhibits higher centroid values compared to *B. terrestris*. A higher spectral centroid indicates that more signal energy is concentrated at higher frequencies, which is consistent with the faster wingbeat rates of honeybees. Conversely, the lower centroid values for *B. terrestris* reflect energy concentrated in lower Doppler regions, aligning with their slower wing motions and lower fundamental frequencies.

2. Spectral Flatness

The Spectral Flatness quantifies how evenly the energy is distributed across frequencies: It is defined as the ratio of the geometric mean to the arithmetic mean of the power spectral density, indicating how uniform the spectral power distribution is across the frequency range [83]:

$$\text{Spectral flatness} = \frac{\left(\prod_{k=0}^{N-1} P(k)\right)^{\frac{1}{N}}}{\frac{1}{N}\sum_{k=0}^{N-1} P(k)} \tag{4.3}$$

where $P(k)$ is the power spectral density at frequency bin k, N is the number of frequency bins.

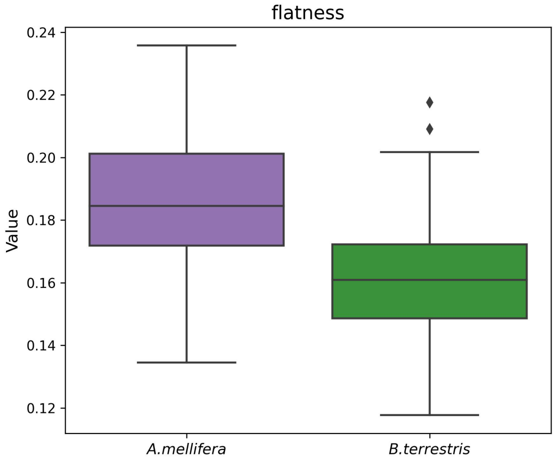

FIGURE 4.9: Spectral flatness distribution for *A. mellifera* and *B. terrestris*

Fig. 4.9 shows that *A. mellifera* has higher flatness values compared to *B. terrestris*. Higher spectral flatness indicates a more broadband signal distribution. In contrast, the lower flatness observed for *B. terrestris* suggests a more concentrated harmonic energy.

3. Spectral Flux

The Spectral Flux measures the amount of spectral change between consecutive time frames:

$$\text{Flux}(m) = \sum_k \left(\tilde{P}_m[k] - \tilde{P}_{m-1}[k]\right)^2$$

Quantifies frame-to-frame spectral variation [84]. Fig. 4.10 shows that *B. terrestris* has higher flux values compared to *A. mellifera*. Larger flux values indicate greater frame-to-frame changes in the spectrum, which may result from more pronounced wing or body motion dynamics.

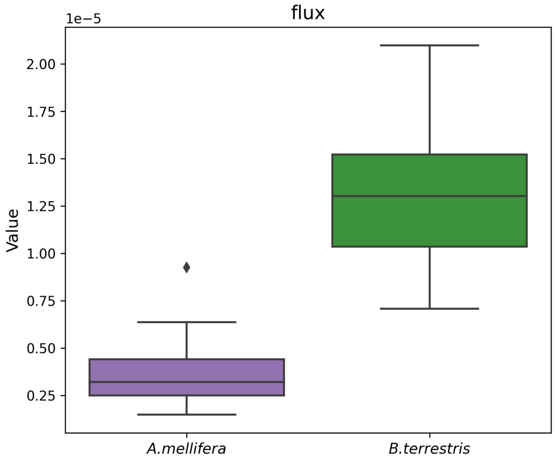

FIGURE 4.10: Spectral flux distribution for *A. mellifera* and *B. terrestris*

4. Spectral Roll-Off

The spectral roll-off frequency is defined as the frequency bin i at which a fixed proportion ρ of the total spectral energy is accumulated [84]. Formally, this is determined by finding the smallest index i that satisfies

$$\sum_{k=b_1}^{i} P[k] = \rho \sum_{k=b_1}^{b_2} P[k],$$

where $P[k]$ represents the spectral power at bin k, b_1 and b_2 denote the lower and upper frequency band edges in bins, and ρ is the chosen energy percentage threshold (e.g., $\rho = 0.95$). This feature effectively characterizes the frequency range over which most of the signal energy is concentrated and tends to shift upward for smaller or faster-flapping insects with higher Doppler content.

Fig. 4.11 shows that *A. mellifera* has higher roll-off frequencies than *B. terrestris*, indicating more energy concentrated at higher Doppler frequencies. This aligns with the faster wingbeat rates of honeybees, while the lower roll-off for bumblebees reflects slower wing motions and lower fundamental frequencies. Fig. 4.11 shows that *A. mellifera* has higher roll-off values compared to *B. terrestris*. Higher roll-off indicates that a greater portion of the signal energy is concentrated in higher Doppler frequency regions, which is consistent with the faster wingbeat rates of honeybees. In contrast, the lower roll-off values observed for bumblebees reflect energy concentrated at lower Doppler frequencies, aligning with their slower wing motions.

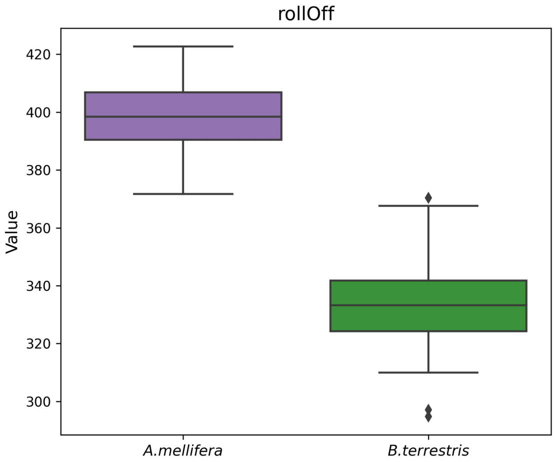

FIGURE 4.11: Spectral roll-Off distribution for *A. mellifera* and *B. terrestris*

5. Spectral Bandwidth

The spectral bandwidth (occupied bandwidth) is defined as the frequency range that contains a fixed percentage of the total spectral energy of the signal. It is computed from the cumulative distribution of the power spectral density obtained using a periodogram with a rectangular window. The spectral bandwidth is given by

$$\mathrm{BW} = f_{p_2} - f_{p_1},$$

where f_{p_1} and f_{p_2} are the lower and upper frequency bounds at which the cumulative spectral energy reaches the percentages p_1 and p_2 of the total energy, respectively. Typically, p_1 and p_2 are set to 0.5% and 99.5% [85].

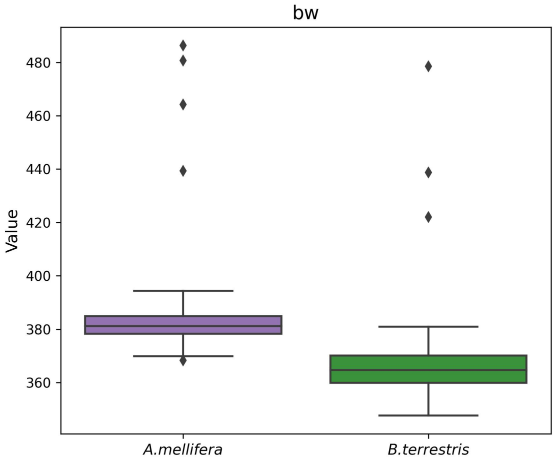

FIGURE 4.12: Spectral bandwidth distribution for *A. mellifera* and *B. terrestris*

Fig. 4.12 shows that *A. mellifera* exhibits a wider occupied Doppler bandwidth compared to *B. terrestris*. This indicates that a larger portion of the signal energy in honeybees is distributed over higher frequencies, consistent with their faster wingbeat rates and more dynamic flight patterns. In contrast, the narrower BW for bumblebees reflects energy concentrated within a smaller frequency range, aligning with their lower and more stable wingbeat frequencies.

6. Spectral Skewness and Kurtosis

Spectral Skewness and Kurtosis describe the shape of the spectral distribution:

$$\text{Skew} = \frac{\sum_k (f[k]-C)^3 P[k]}{(\sum_k P[k])\,\text{BW}^3}, \qquad \text{Kurt} = \frac{\sum_k (f[k]-C)^4 P[k]}{(\sum_k P[k])\,\text{BW}^4}$$

Skewness indicates asymmetry in spectral energy distribution (bias toward higher or lower Doppler) [86]. Higher skewness indicates that the spectral energy is more asymmetrically distributed, with stronger dominance toward lower frequencies. This is consistent with bumblebees' lower fundamental wingbeat frequency and energy concentration in lower Doppler regions (Fig. 4.13). Honeybees, with lower skewness, have a more balanced spectral distribution due to their broader frequency spread. Kurtosis quantifies the peakedness of the spectral peaks [86], higher values signify sharp harmonic peaks from stable wingbeats. Fig. 4.14 shows that *B. terrestris* has higher kurtosis values compared to *A. mellifera*. A higher kurtosis reflects a sharper, more peaked spectral distribution, indicating energy

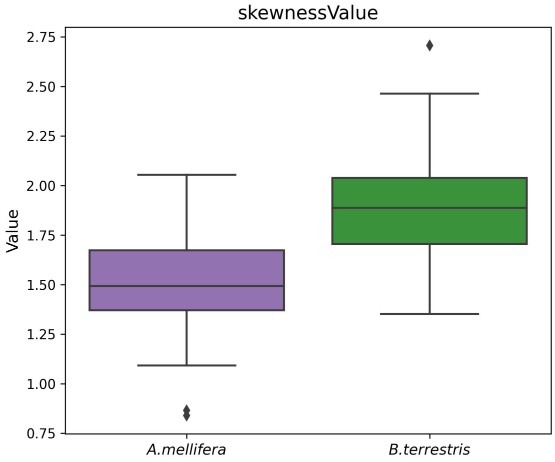

FIGURE 4.13: Skewness distribution for *A. mellifera* and *B. terrestris*

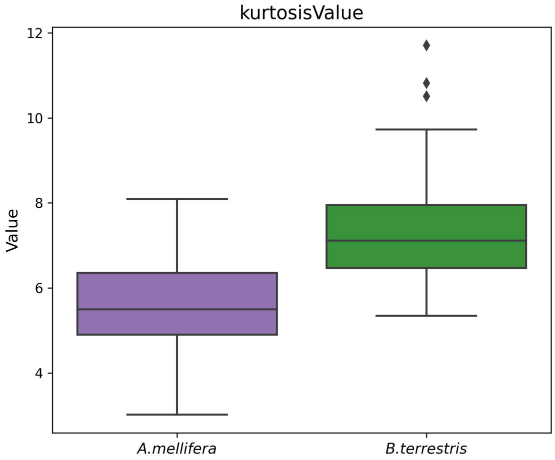

FIGURE 4.14: Kurtosis distribution for *A. mellifera* and *B. terrestris*

concentrated near the fundamental frequency with less spread. In contrast, the lower kurtosis in honeybees suggests a flatter spectral profile with more distributed harmonic energy, aligning with their faster wingbeat rates and broader spectral content.

7. Spectral Decrease

The spectral decrease quantifies how rapidly spectral amplitude decays at higher frequencies [82]:

$$\text{Spectral decrease} = \frac{\sum_{k=2}^{N} \frac{P(k)-P(1)}{k-1}}{\sum_{k=2}^{N} P(k)}$$

where $P(k)$ represents the power spectral density at the k-th frequency bin and N is the total number of frequency bins.

This expression quantifies the rate at which the spectral amplitude decreases with increasing frequency, where larger values correspond to a steeper decay of energy across the spectrum. Fig. 4.15 shows that *B. terrestris* has notably higher values compared to *A. mellifera*, suggesting that most of the energy for bumblebees is concentrated near the fundamental frequency with a rapid drop-off at higher frequencies. In contrast, the lower decrease values for honeybees indicate a more gradual decay, consistent with their broader spectral energy distribution caused by faster wingbeats and stronger harmonic content.

A more negative slope corresponds to tonal, periodic wingbeats; a flatter slope indicates broadband scattering or turbulent motion.

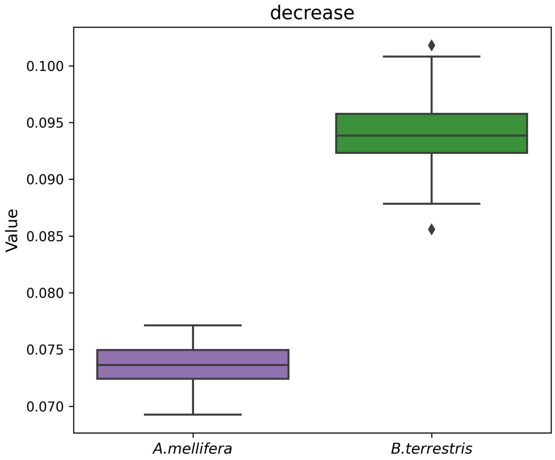

FIGURE 4.15: Spectral decrease distribution for *A. mellifera* and *B. terrestris*

8. Band Power Features

Band power features represent the total energy contained within fixed frequency intervals:

$$\mathrm{BP}_{[a,b]} = \sum_{f[k]\in[a,b]} P[k]$$

Total energy within fixed Doppler frequency bands. Different insect taxa distribute their wingbeat energy in distinct frequency intervals, enabling class discrimination.

The box plots of band power across different frequency ranges reveal distinct spectral energy distributions between *B. terrestris* and *A. mellifera.* In the lower frequency band (100–150 Hz), *B. terrestris* exhibits consistently higher energy, reflecting its lower fundamental wingbeat frequency and strong harmonic components concentrated at the lower end of the Doppler spectrum. This is clearly visible in the spectrogram, where the bumblebee signal shows bright, stable harmonic bands in the lower frequency region.

In contrast, *A. mellifera* shows higher energy in the mid- and high-frequency bands (150–200 Hz and 350–400 Hz), consistent with its higher wingbeat rate and broader spectral spread. The honeybee spectrogram displays elevated energy at higher Doppler frequencies, corresponding to more intense wingbeat harmonics and possibly more dynamic flight.

Cepstral Features: Mel Frequency Cepstral Coefficients (MFCCs)

MFCCs provide a compact and robust representation of the spectral envelope of a signal. They are derived by first computing the power spectrum of the signal using the STFT,

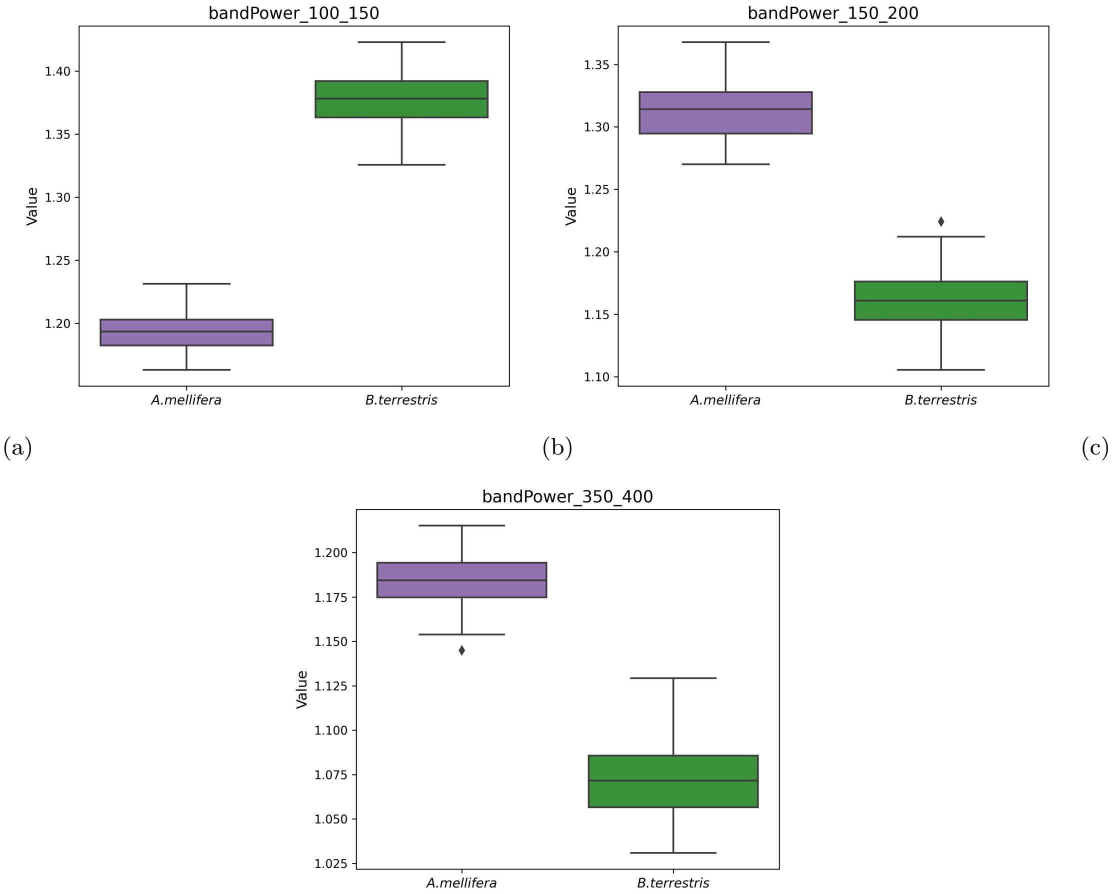

(a) (b) (c)

FIGURE 4.16: Band Power distribution for *A. mellifera* and *B. terrestris*

which represents the frequency content over time. The resulting spectrum is then passed through a Mel-scale filterbank, a perceptually motivated frequency warping that provides finer resolution at lower frequencies and coarser resolution at higher frequencies. For each filter m, the energy is computed as

$$E_m = \sum_f P(f)\, H_m(f),$$

where $P(f)$ denotes the power spectrum and $H_m(f)$ represents the weighting function of the m-th Mel filter. The logarithm of the filterbank energies is then taken to compress the dynamic range and emphasize relative differences. The discrete cosine transform is finally applied to decorrelate the log energies and obtain the cepstral coefficients:

$$C_n = \sum_{m=1}^{M} \log(E_m)\, \cos\left[\frac{\pi n}{M}\left(m - \frac{1}{2}\right)\right], \qquad n = 0, 1, \ldots, N_c - 1.$$

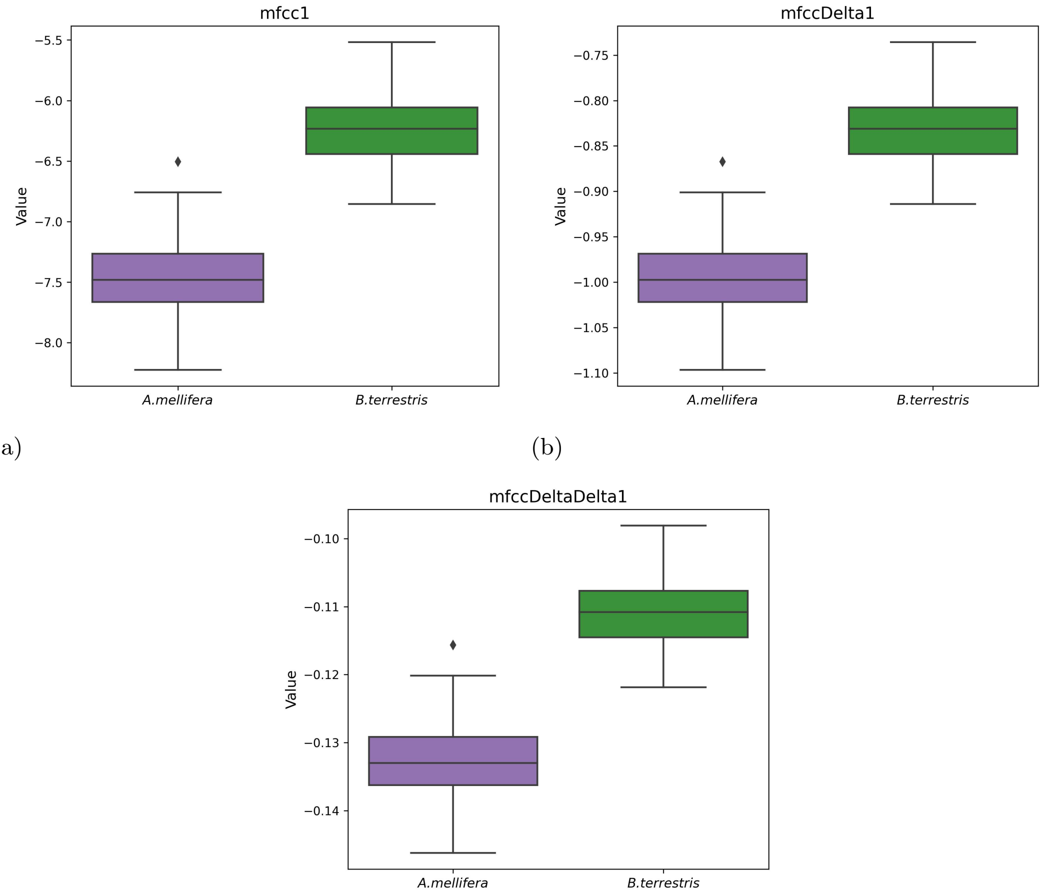

(a) (b) (c)

FIGURE 4.17: mfcc1, mfccDelta1, and mfccDeltaDelta1 distribution for A. mellifera and B. terrestris

These coefficients collectively form the MFCC representation, where lower-order coefficients capture the coarse spectral envelope and higher-order coefficients describe finer spectral details.

MFCCs are extracted as a vector of cepstral coefficients (indexed as mfcc0, mfcc1, . . .), representing the spectral envelope of the reflected signal. First-order temporal derivatives (mfccDelta) are computed for each MFCC coefficient and capture the rate of change of the spectral envelope over time, while second-order derivatives (mfccDeltaDelta) capture the acceleration of these changes, reflecting the smoothness or abruptness of temporal spectral evolution associated with insect wing-beat motion. The box plots of MFCC1, mfccDelta1, and mfccDeltaDelta1 show clear differences between *A. mellifera* and *B. terrestris*. *B. terrestris* consistently exhibits higher values across all three representations, reflecting its lower and more stable wingbeat frequencies that produce stronger low-frequency harmonic components. In contrast, *A. mellifera* shows lower MFCC values, consistent with its higher wingbeat frequencies and broader spectral distribution.

4.4 Feature Analysis Summary

Each spectral and temporal feature captures a distinct characteristic of the wingbeat-induced micro-Doppler signature, enabling clear discrimination between the two insect species. Features related to periodicity and tonal structure, including harmonic ratio, spectral flatness, kurtosis, and spectral decrease, indicate that *B. terrestris* exhibits more stable and tonal wingbeat patterns, with higher harmonic ratio, lower spectral flatness, and higher kurtosis, reflecting energy concentration near the fundamental frequency. In contrast, *A. mellifera* demonstrates lower harmonic ratio and kurtosis together with a slower spectral decay, suggesting reduced harmonic stability and a broader distribution of spectral energy.

Spectral balance metrics, such as centroid, roll-off, and bandwidth, further distinguish the species, with *A. mellifera* showing consistently higher values, in line with its higher wingbeat frequency and increased harmonic energy in higher Doppler regions. Conversely, *B. terrestris* concentrates energy at lower frequencies, consistent with slower and more stable wing motion. Temporal dynamics captured by spectral flux reveal higher variability for *B. terrestris*, indicating more pronounced transitions between wing strokes and fluctuations in harmonic structure, whereas *A. mellifera* exhibits lower flux, reflecting a more uniform spectral profile despite operating at higher frequencies.

Energy localization metrics, including band power, highlight species-specific frequency dominance, with bumblebees exhibiting stronger energy in lower frequency bands (100–150 Hz), while honeybees dominate higher frequency bands (150–200 Hz and 350–400 Hz), corresponding to their distinct wingbeat frequencies and harmonic distributions. Finally, compact spectral representations provided by MFCCs and their temporal derivatives offer clear separability between species: higher MFCC values for *B. terrestris* reflect concentrated low-frequency energy, whereas lower values for *A. mellifera* indicate greater high-frequency spread and increased spectral complexity.

Together, these temporal and spectral features provide a distinctive multi-domain fingerprint of wingbeat dynamics, enabling reliable differentiation between the two species and forming a strong basis for downstream classification.

4.5 Summary

This chapter first introduced an automated signal processing framework designed to efficiently isolate micro-Doppler activity from continuously recorded radar data.

To motivate the feature extraction strategy, temporal and spectral signatures of wing-flapping micro-Doppler signals were compared and illustrated for two representative species: *B. terrestris* and *A. mellifera.* To quantitatively capture these patterns, the micro-Doppler active signal segments were analyzed to extract features that characterize different aspects of wingbeat dynamics. Temporal, harmonic, spectral, and band power features were computed to describe oscillation rates, frequency content, harmonic richness, and energy distribution across Doppler frequencies. The feature analysis revealed consistent and interpretable patterns between the bumblebee and the honeybee. Bumblebees exhibited lower fundamental frequencies, narrower bandwidth, and higher harmonic stability, whereas honeybees showed higher wingbeat frequencies, broader spectral spread, and increased energy at higher Doppler frequencies.

While the extracted features already demonstrate clear separability between the two pollinating insect species with distinct body sizes, achieving fine-grained classification among closely related species remains more challenging. This motivates the use of advanced machine learning models capable of learning complex decision boundaries and subtle feature interactions, which is addressed in the subsequent chapter.

Chapter 5

Taxonomic Classification of Insects

Chapter 5 introduces an innovative method for classifying individual pollinating insects taxonomically using mmWave signal technology along with a hierarchical Machine Learning (ML) framework. It systematically examines signal features related to wing flapping and utilizes SHAP (SHapley Additive exPlanation) analysis to pinpoint the most influential features for classification success. A hierarchical ML model was developed, achieving an 85% accuracy rate in classifying five major pollinator species. With mmWave systems increasingly integrated into communication infrastructure, this approach provides a scalable, cost-effective, and contactless means of high-resolution insect biodiversity monitoring.

5.1 Methodology

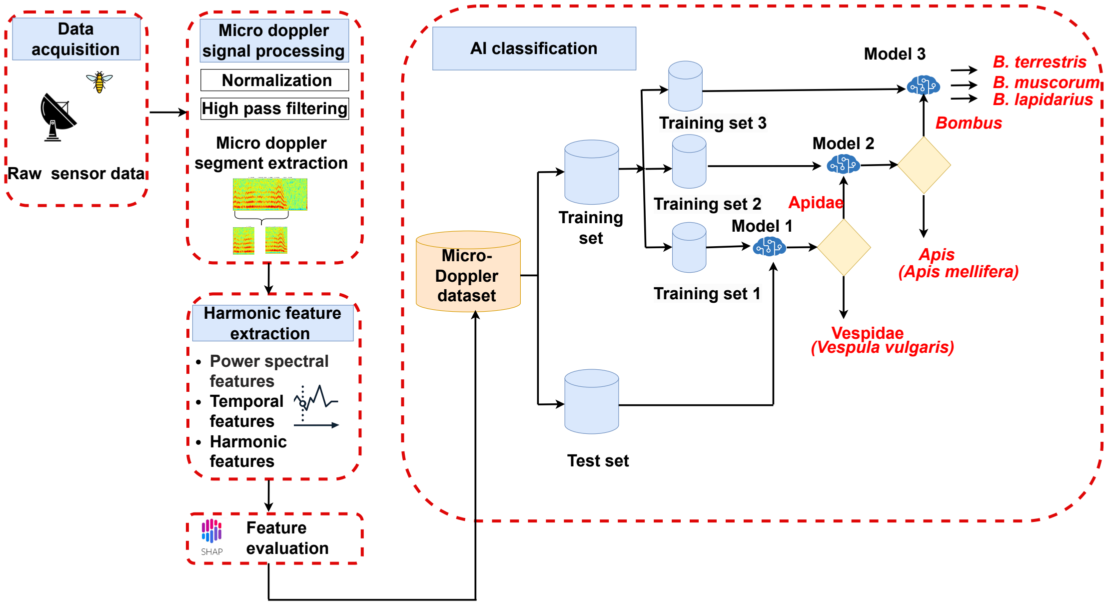

Figure 5.1: Overview of the proposed methodology for micro-Doppler–based insect taxonomic classification

Figure 5.1 provides an overview of the proposed methodology for micro-Doppler–based insect taxonomic classification. The process begins with radar data acquisition, in which reflected signals from flying insects are recorded following the transmission of a single-frequency CW signal. The acquired signals are subsequently preprocessed to identify and isolate time segments containing wingbeat-induced micro-Doppler activity. From these segments, a set of discriminative features describing wing-flapping dynamics is extracted. Feature relevance is then assessed using SHAP to interpret the contribution of individual features to the classification process, and a labeled micro-Doppler dataset is constructed across multiple insect species.

To ensure subject-independent evaluation, the dataset is partitioned into training and testing subsets based on individual insect identifiers, preventing signals from the same insect from appearing in both sets. Finally, a three-tier hierarchical classification framework is employed to perform taxonomic identification at the family, genus, and species levels.

5.1.1 Data Collection

The data acquisition for the taxonomic classification experiments followed the experimental setup described in Chapter 3. Measurements were conducted between May and November 2023 using live insects from the order *Hymenoptera*, which were released back into their natural environment after data collection. CW measurements were performed at 30 GHz using a Rohde & Schwarz Vector Network Analyzer and a broadband horn antenna (BBHA 9170). For each trial, the reflected signal was recorded for 60 s, resulting in 60,001 samples of amplitude and phase. Synchronized video recordings were used to establish ground truth for flight activity. Video data were used only as a coarse temporal reference and were not employed for analysis, filtering, or signal identification, which were conducted solely using radar data. As the insects were free to move during observations, they exhibited diverse behaviors, including flight, wing flapping, idling, and various movement patterns such as vertical and circular navigation within the containers. Measurements were obtained only from individuals that displayed at least one instance of wing flapping, which constituted the primary focus of the analysis. Although data were collected from multiple specimens per species, only a subset demonstrated the required wing flapping behavior; the number of such specimens is listed in Table 5.1. Different insect species likely exhibit different patterns of wing movements (Fig. 5.2), while differences

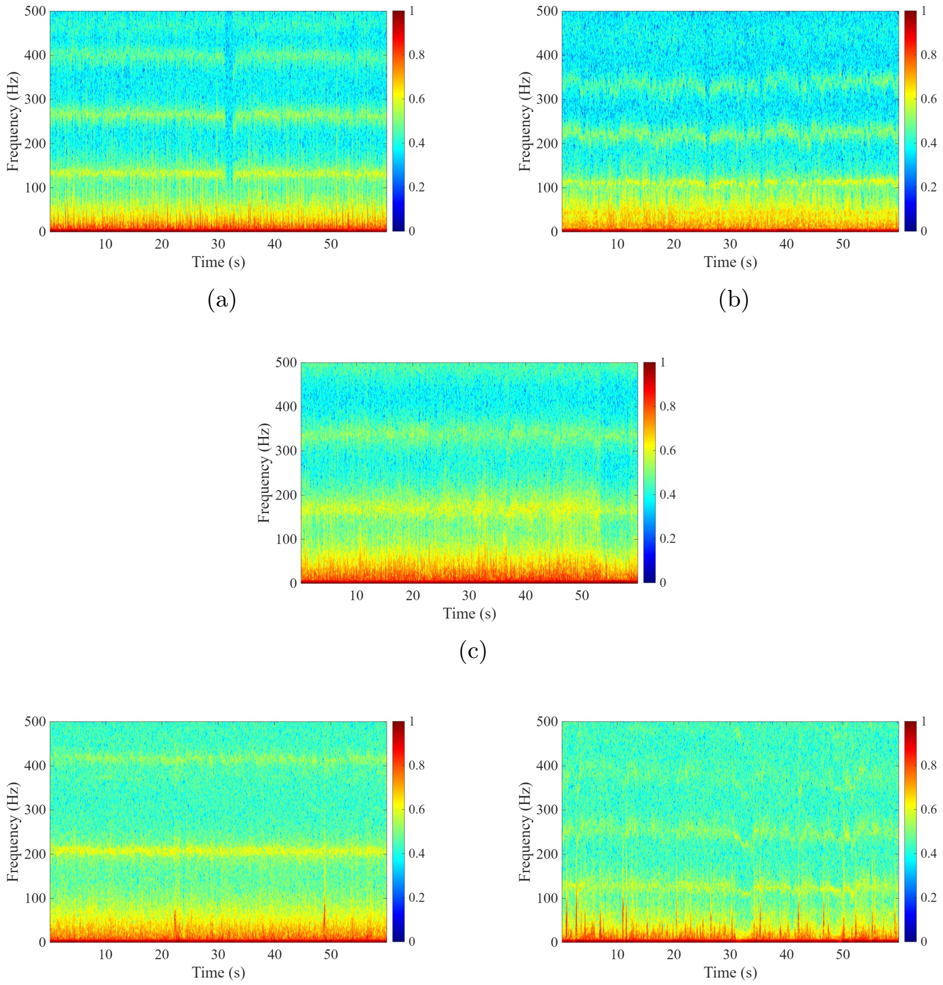

(a) (b) (c) (d) (e)

Figure 5.2: Exemplary reflected micro-Doppler spectrograms from wing flapping of five different pollinating insect species. (a) *Bombus lapidarius*, (b) *Bombus terrestris*, (c) *Bombus muscorum*, (d) *Apis mellifera*, and (e) *Vespula vulgaris*.

among some species can be observed visually, a trained machine learning algorithm can identify differences that are less apparent to the naked eye.

5.1.2 Preprocessing of the Signal

The signal preprocessing steps follow the methodology detailed in Chapter 4 and are briefly summarized here for completeness. The recorded signals are first normalized to mitigate amplitude variations and reduce the influence of noise. A second-order Chebyshev high-pass filter with a cut-off frequency of 50 Hz is then applied to suppress slow-varying background components.

Table 5.1: Numbers of live insect subjects and flight segments of various durations used for training machine learning classification models

Class	**Subjects**	2 s	1 s	0.8 s	0.6 s	0.4 s	0.2 s	0.1 s
A. mellifera	11	1244	2416	3002	3950	5860	11491	22320
B. lapidarius	4	1168	2122	2620	3358	4815	9085	17335
B. terrestris	6	1070	2416	2626	3434	5116	10073	19742
B. muscorum	5	680	1372	1716	2253	3334	6572	12925
V. vulgaris	7	931	1755	2106	2729	3995	7772	14756

Following signal conditioning, a coarse micro-Doppler segmentation is performed to identify time intervals containing wingbeat-induced activity. The preprocessed mmWave signal is divided into overlapping frames using a 2 s Hann window with a 1 s overlap. For each frame, the harmonic ratio is computed, and segments exceeding a predefined threshold are classified as containing micro-Doppler features and retained for subsequent analysis. Therefore, the number of flight segments reported in Table 5.1 corresponds directly to the number of overlapping frames selected based on this harmonic thresholding approach. Additionally, the segmentation was repeated using shorter window lengths ranging from 1 s down to 0.1 s to generate additional segment sets, also summarized in Table 5.1.

5.1.3 Micro-Doppler Feature Extraction

Species-specific flight characteristics are captured through the extraction of micro-Doppler features from wingbeat signal segments. For brevity, the detailed definitions of the extracted features are not repeated here and can be found in Chapter 4.

The extracted feature set comprises harmonic, spectral, and temporal descriptors. Harmonic features include the harmonic ratio (*HarmonicRatio*), which quantifies the proportion of energy contained in harmonic components, as well as estimates of the fundamental WBF and its associated harmonics. These include the STFT-based fundamental frequency (*STFT_F0*) and the first- to fifth-order harmonics (*Harmonics_1–5*). While the STFT-based fundamental frequency estimation was detailed in Chapter 4, additional complementary estimators are employed in this work to improve robustness and capture algorithm-dependent variations. These include pitch estimation filter–based fundamental frequency estimation (*PEF_F0*) [87], cepstrum-based fundamental frequency estimation

(*CEP_F0*) [88], wavelet transform–based estimation (*WT_F0*), and normalized correlation–based estimation (*NCF_F*) [89]. The use of multiple fundamental-frequency estimators provides diverse representations of wingbeat periodicity, enabling a more comprehensive characterization of insect flight dynamics.

Spectral features extracted from the micro-Doppler spectra include spectral centroid (*SpectralCentroids*), spectral bandwidth (*SpectralBW*), spectral roll-off (*SpectralRollOff*), spectral flatness (*SpectralFlatness*), spectral flux (*SpectralFlux*), spectral skewness (*SkewnessValue*), spectral kurtosis (*KurtosisValue*), and spectral decrease (*SpectralDecrease*). Cepstral features are represented by Mel-frequency cepstral coefficients (*mfcc*) and their first- and second-order temporal derivatives (*mfccDelta* and *mfccDeltaDelta*), which capture the short-term spectral envelope and its temporal dynamics. In addition, band-power ratio features (*BPR_0_50Hz*, …, *BPR_450_500Hz*) quantify the relative distribution of spectral energy across predefined frequency bands.

Temporal features include the zero-crossing rate (*zcr*), which reflects oscillatory characteristics of the high-pass filtered signal, and the root-mean-square energy (*rmsEnergy*), which represents the overall signal energy within each frame.

Feature extraction was performed in MATLAB using established spectral, cepstral, and pitch estimation functions, as well as MFCC analysis [90].

5.1.4 Hierarchical Classification of Insects

We employed a hybrid multistage classification framework based on CatBoost and ExtraTrees, selected from a broader range of machine-learning approaches. In general, classification models range from simple linear methods to highly complex deep learning architectures such as convolutional neural networks. Linear models are computationally efficient but limited in their ability to capture the nonlinear relationships and feature interactions present in micro-Doppler signatures, whereas deep neural networks typically require substantially larger datasets to achieve good generalisation and involve significantly higher training complexity and hyperparameter tuning effort [91], [92]. Given the moderate size of the present dataset and the structured hand-crafted feature set, ensemble tree-based methods provide a suitable balance between model capacity and generalisation performance while inherently reducing the risk of overfitting [93].

Tree-based ensembles are particularly well matched to the extracted micro-Doppler features, which include harmonic, spectral, temporal, and band-power descriptors with different numerical ranges and partial correlations. These models can handle heterogeneous features without normalisation, capture nonlinear decision boundaries, and remain robust when the number of training samples is limited [94].

Within this class of models, CatBoost was selected for the initial classification stages because its gradient-boosting formulation effectively learns high-level nonlinear feature interactions and achieves low bias. Its ordered boosting mechanism reduces prediction shift and prevents the model from memorising the training data at successive iterations, thereby improving generalisation for moderately sized datasets. In addition, its symmetric tree structure and built-in regularisation provide stable performance with minimal hyperparameter tuning [95].

For the final stage, where the classes exhibit highly similar micro-Doppler signatures and the separability depends on subtle variations in spectral and temporal features, an ExtraTrees classifier was employed. Compared with Random Forest, ExtraTrees uses fully randomised split selection, which increases tree diversity and provides stronger variance reduction through ensemble averaging, making it more robust in the presence of overlapping class distributions and noise [93].

Model Initialization and Training

A micro-Doppler dataset was constructed by extracting relevant features from all micro-Doppler segments obtained from various insect species. For model initialization and training, the dataset was divided into training and test sets, with 80% allocated for training and 20% for testing. Care was taken to ensure that data from the same subject did not appear in both the training and test sets, thereby preventing potential data leakage.

A hierarchical classification framework was developed to predict insect species in a sequential manner, mirroring the natural taxonomic hierarchy of the dataset. In the first stage, a CatBoost classifier was trained to distinguish between the families Vespidae and Apidae, using all available training samples. Instances classified as Vespidae at this stage were directly assigned the species *V. vulgaris*, as no further subclass differentiation was required. Samples classified as Apidae proceeded to the second stage, where a separate CatBoost model predicted the genera *Apis*, and *Bombus*. Predictions of *Apis* were mapped directly to the species *A. mellifera*, while samples identified as *Bombus* were passed to a third-stage classifier. This final model, implemented using an ExtraTrees classifier, was trained to discriminate between the three *Bombus* species (*B. lapidarius*, *B. muscorum*, and *B. terrestris*).

Model Evaluation

The trained hierarchical classifiers were evaluated using a test set comprising samples from individuals excluded from the training process. At each stage of the hierarchy, predictions were generated and, when applicable, forwarded to the next level for further classification. The overall performance was assessed at the species level by comparing the final predicted labels with the corresponding ground-truth labels.

Performance Metrics

Model performance was evaluated using standard classification metrics, including accuracy, precision, recall, and F1-score. Confusion matrices were generated to visualise misclassification patterns and to report cumulative end-to-end predictions across the hierarchical classification stages. Predictions finalised at earlier stages were retained in the overall evaluation, even though the corresponding classes were excluded from training in subsequent stages.

Accuracy is defined as the proportion of correctly classified samples and is computed as the ratio of the sum of the diagonal elements of the confusion matrix to the total number of samples. To provide a more informative assessment under class imbalance, precision, recall, and F1-scores were computed on a per-class basis [96]. For a given class, true positives (TP) denote samples correctly assigned to that class, false positives (FP) correspond to samples incorrectly assigned to the class, false negatives (FN) represent samples belonging to the class but incorrectly classified as another class, and true negatives (TN) denote samples correctly identified as not belonging to the class.

The F1-score, which balances precision and recall, is defined as

$$\mathrm{F1} = \frac{2 \times \mathrm{Precision} \times \mathrm{Recall}}{\mathrm{Precision} + \mathrm{Recall}}, \tag{5.1}$$

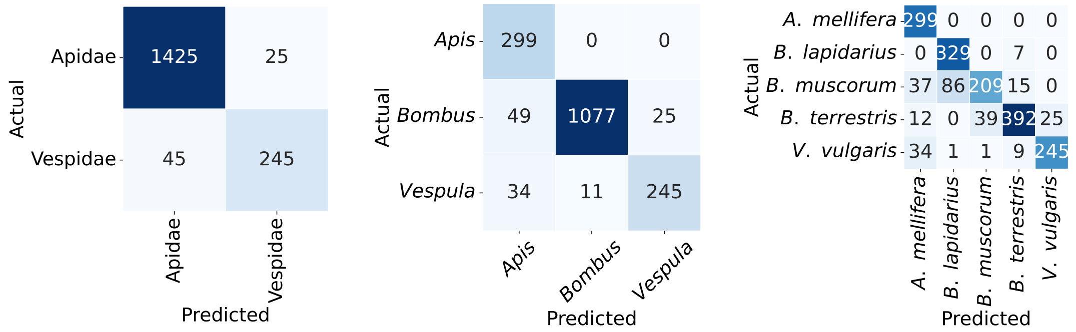

(a) (b) (c)

FIGURE 5.3: Confusion matrices showing results of (a) the first-level classification distinguishing between Vespidae and Apidae families, (b) second-level classification differentiating among the genera *Apis*, *Bombus*, and *Vespula*, (c) third-level classification identifying species *V. vulgaris*, *A. mellifera*, *B. lapidarius*, *B. muscorum*, and *B. terrestris*

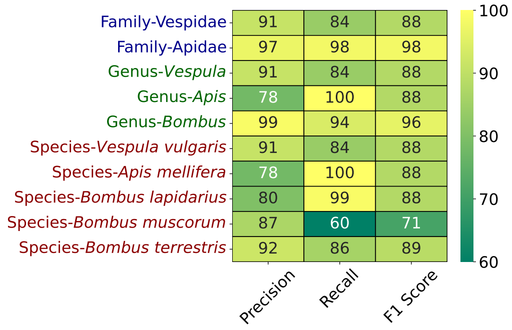

FIGURE 5.4: Performance of the hierarchical classification model at different taxonomic levels. Hierarchical performance metrics (precision, recall and the F1 Score), heatmap across various categories. Precision indicates the accuracy of positive predictions, recall shows the model's ability to find all relevant instances and the F1 Score represents the balance between precision and recall.

where precision and recall are given by Precision $= \frac{TP}{TP+FP}$ and Recall $= \frac{TP}{TP+FN}$, respectively.

5.2 Classification Results

At the family level, the first-stage classifier distinguished between the Apidae and Vespidae families with an accuracy of 96% (Fig. 5.3a). Additional performance metrics, including precision, recall, and F1 score (a measure of the balance between precision and recall; see *Methods*), further indicate robust classification performance (Fig. 5.4a). Samples classified as Vespidae at this stage were directly assigned to *V. vulgaris*.

Samples classified as Apidae were passed to a second-stage classifier that differentiated between the genera *Apis* and *Bombus.* Predictions finalised in the previous stage (*V. vulgaris*) were retained unchanged, and the cumulative end-to-end classification accuracy at this stage was 93% (Fig. 5.3b). Samples classified as *Apis* were directly mapped to *A. mellifera*, while those classified as *Bombus* were forwarded to the third-stage model.

The third-stage classifier operated only on samples identified as *Bombus* and discriminated among the species *B. lapidarius*, *B. muscorum*, and *B. terrestris.* Predictions for *A. mellifera* and *V. vulgaris*, finalised in earlier stages, were carried forward unchanged. Considering all species jointly, the cumulative species-level classification accuracy was 85% (Fig. 5.3c). Notably, the F1 scores for these species were comparable, except for *B. muscorum*, which showed lower values likely due to smaller sample size (Table 5.1).

5.3 Feature Importance and Species-Level Interpretation

The influence of radar-derived features on model predictions was evaluated using SHAP [97], offering both overall and species-level perspectives on how the classifier makes decisions. SHAP values quantify each feature's marginal effect on the model's output, allowing for straightforward interpretation of feature–response relationships and highlighting biologically relevant signals that contribute to distinguishing among species.

Species-specific SHAP summary plots (Figs. 5.5–5.6) illustrate how individual features contribute to each class prediction. For *A. mellifera*, high values of *WT_F0*, *PEF_F0*, and *mfcc1* yield strong positive SHAP effects, aligning with its characteristically higher wingbeat frequency and wider spectral distribution. *B. lapidarius* is primarily influenced by *harmonicRatio* and several higher-order *mfccDelta* features, pointing to its stable, harmonic-rich wingbeat signature. In *B. muscorum*, *harmonicRatio*, *mfcc7*, and moderate contributions from *WT_F0* are most impactful, suggesting a blend of harmonic consistency and moderately elevated F_0. *B. terrestris* exhibits a more diverse pattern of sensitivity across *WT_F0*, *PEF_F0*, and *mfccDelta* components, reflecting its lower fundamental frequency coupled with a structured spectral profile. In contrast, *V. vulgaris* predictions are shaped strongly by *mfccDelta1*, *mfcc1*, and low-frequency band-power features (100–350 Hz), typical of its low F_0 and steeper spectral slope, which differentiate it clearly from Apidae taxa.

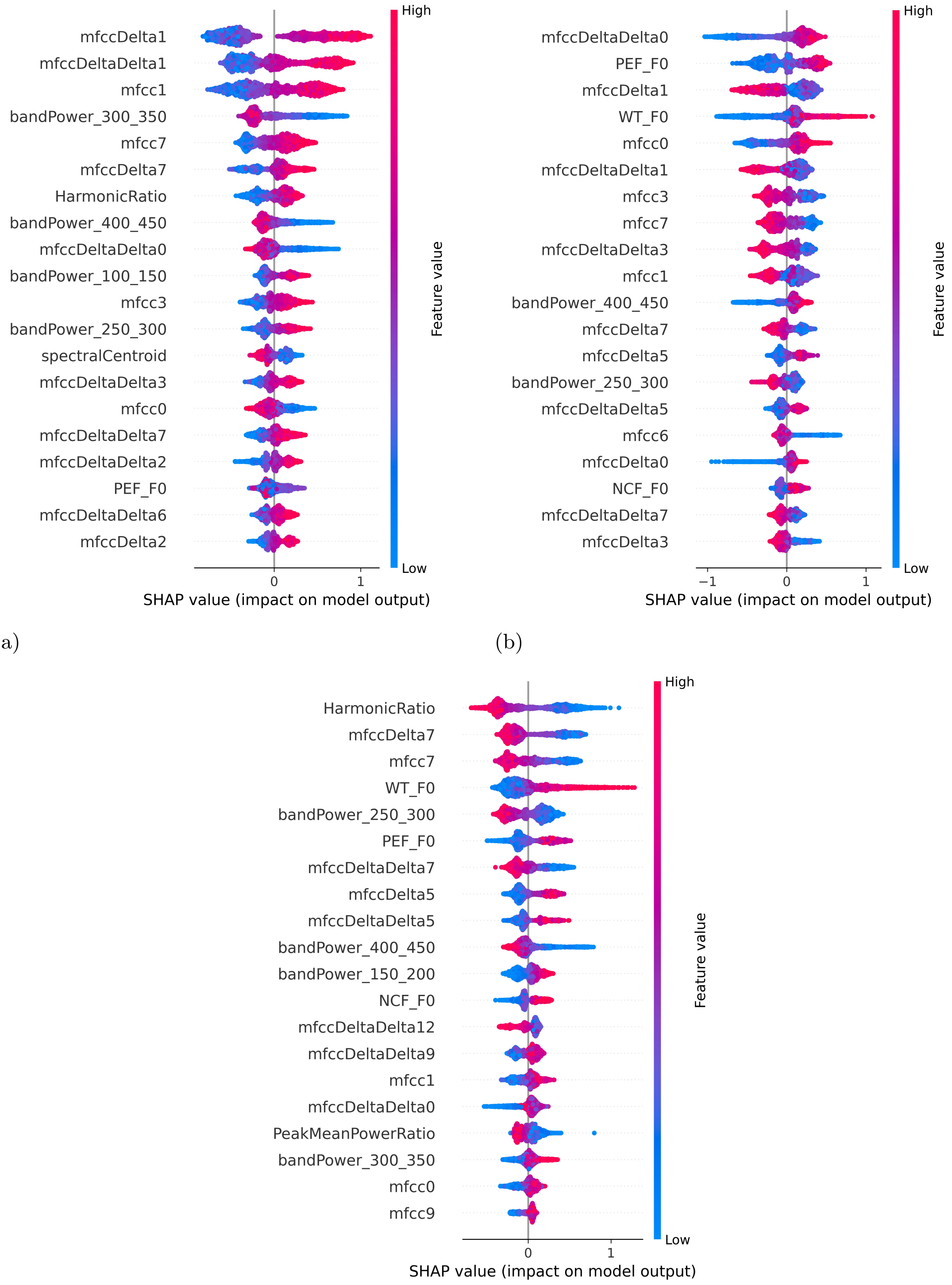

(a) (b) (c)

FIGURE 5.5: Species-specific SHAP summary plots for (a) *B. lapidarius*, (b) *A. mellifera*, and (c) *B. muscorum*.

The global SHAP bar plot (Fig. 5.7) identifies the twenty most influential features driving overall classification outcomes. The leading contributors include a mixture of temporal–spectral descriptors and fundamental-frequency estimators, with *mfccDelta1*, *WT_F0*, *mfcc1*, *mfccDeltaDelta1*, *PEF_F0*, and *nCF_F0* ranking highest. These are

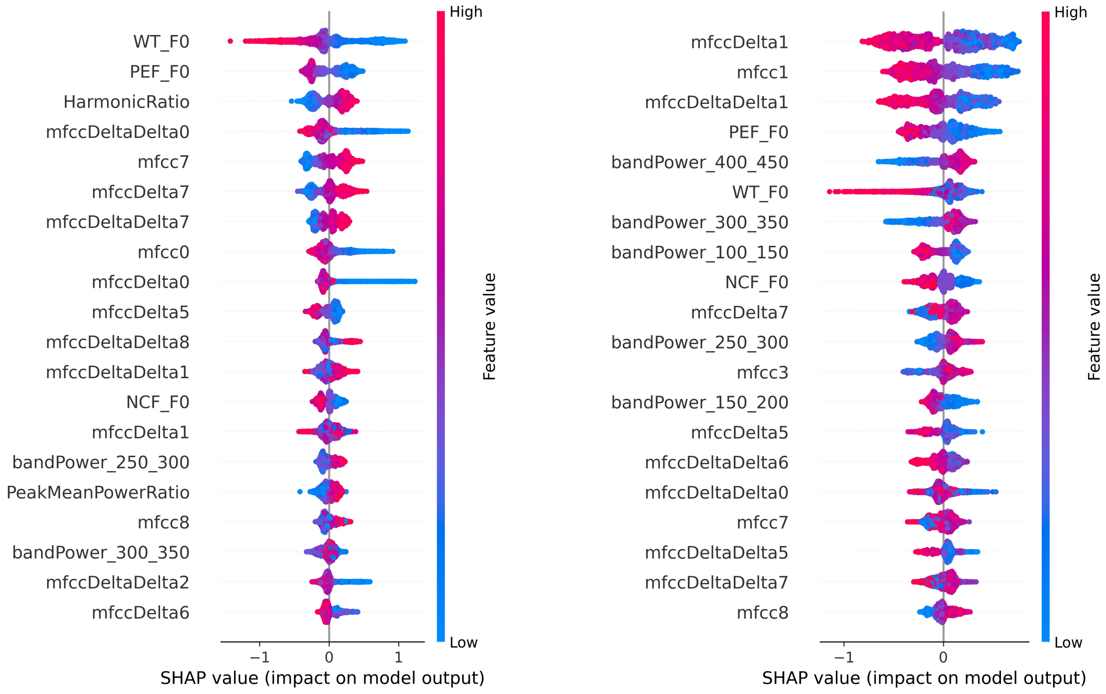

(a) (b)

FIGURE 5.6: Species-specific SHAP summary plots for (d) *B. terrestris* and (e) *V. vulgaris* .

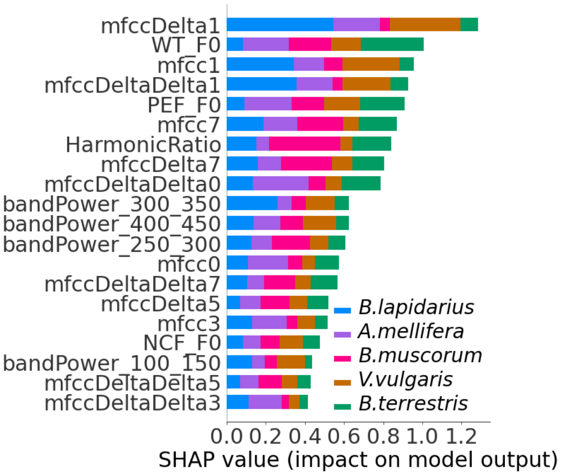

FIGURE 5.7: Features importance and their contribution to prediction evaluation using SHAP, showing the top 20 features influencing species classification.

followed by higher-order spectral features such as *mfcc7*, *harmonicRatio*, and Doppler band-power ratios within the 100–450 Hz range. Collectively, the SHAP patterns indicate that fundamental-frequency features predominantly govern broad-scale taxonomic separation (family/genus), whereas MFCC-based temporal–spectral attributes are critical for distinguishing species within genera. From a biomechanical standpoint, these relationships

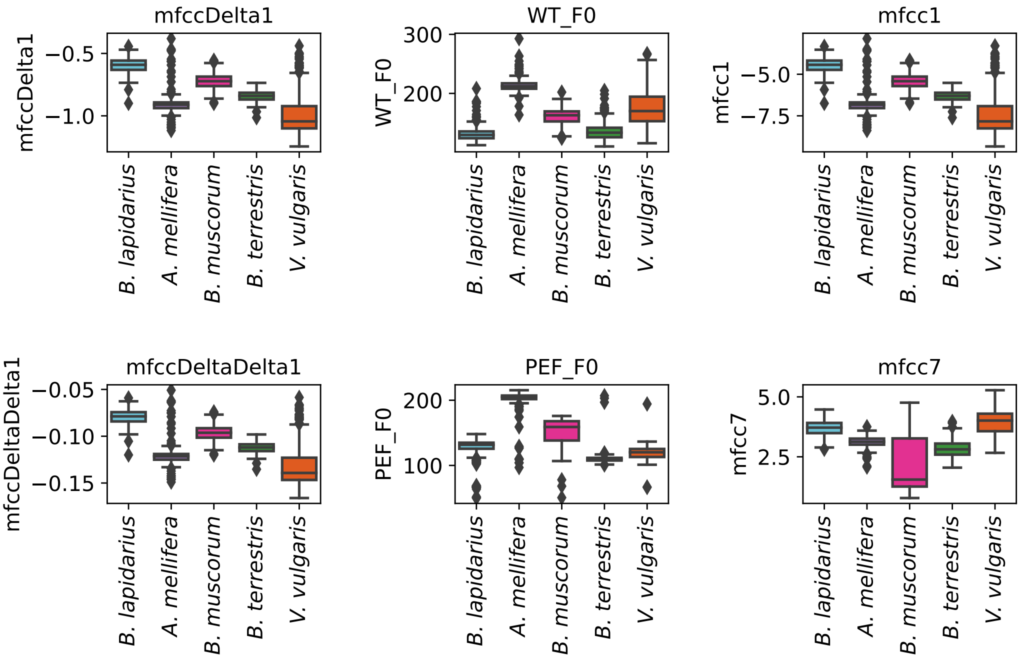

Figure 5.8: Box plots of the six features that contributed most to the classification of our focal insect species (see Fig. 5.7).

reflect established morphological scaling patterns: smaller insects typically generate higher wingbeat frequencies and broader Doppler spectra, while larger bumblebees produce lower F_0 values and more consistent harmonic structure. The harmonic ratio captures stroke periodicity and symmetry, aiding in differentiating species with stable wingbeat patterns (e.g., *B. lapidarius*) from those with greater variability. Meanwhile, MFCC delta and delta-delta coefficients track temporal changes in the spectral envelope, effectively encoding subtle differences in stroke dynamics that help discriminate closely related *Bombus* species.

5.3.1 Boxplots of the Most Discriminative Features

To assess inter-species separability, six of the most influential features (*mfccDelta1*, *WT_F0*, *mfcc1*, *mfccDeltaDelta1*, *PEF_F0*, *mfcc7*) were visualized using boxplots (Fig. 5.8). Clear, non-overlapping medians in *WT_F0* and *PEF_F0* between *A. mellifera* and *V. vulgaris* support their role in family-level discrimination. Within the *Bombus* genus, substantial overlap in F_0 distributions indicates the necessity of higher-order descriptors: *mfccDelta1*, *mfccDeltaDelta1*, and *mfcc7* show pronounced distributional differences among *B. lapidarius*, *B. muscorum*, and *B. terrestris*, aligning with SHAP-derived patterns of intra-genus separability. The feature *mfcc1* further differentiates *V. vulgaris* through its characteristically lower (steeper) spectral slope. Collectively, these six features encapsulate both broad taxonomic distinctions (family, genus) and fine-scale species-level variation in Doppler-derived signatures.

5.4 Duration of Recorded Wing Flapping

To capture species-specific temporal characteristics, the algorithm processes signal fragments of varying lengths. Although longer segments generally enhance classification performance, they are more challenging to obtain because insects must remain airborne and within the radar beam for the entire duration. Figure 5.9a shows F1 scores for segment lengths of 0.1, 0.2, 0.4, 0.6, 0.8, 1, and 2 seconds across the five study species, with corresponding sample counts provided in Table 5.1. Each recording was used only at its longest available segment length to avoid reuse across durations. Durations exceeding 2 seconds were explored by extending analysis windows on the raw recordings, but too few valid samples were available for statistical evaluation. Durations shorter than 0.1 seconds were excluded because such brief intervals yield insufficient frequency resolution to reliably capture wingbeat harmonics.

Across species, F1 scores generally increase with segment duration, with the exception of *B. muscorum.* As the length of airborne signal segments increases, model performance improves correspondingly (Fig. 5.9b), as expected. With 2-second micro-Doppler segments, the classifier achieved an accuracy of 85%. However, shorter wingbeat segments led to reduced performance, with overall accuracy decreasing to 75% at a duration of 0.1 seconds (Fig. 5.9b).

5.5 Target Detection Range Evaluation

Time–frequency analysis based on the STFT was employed to examine signals recorded at different target distances. The STFT representations of the micro-Doppler harmonic components (Fig. 5.11) show clearly distinguishable spectral patterns at both the minimum

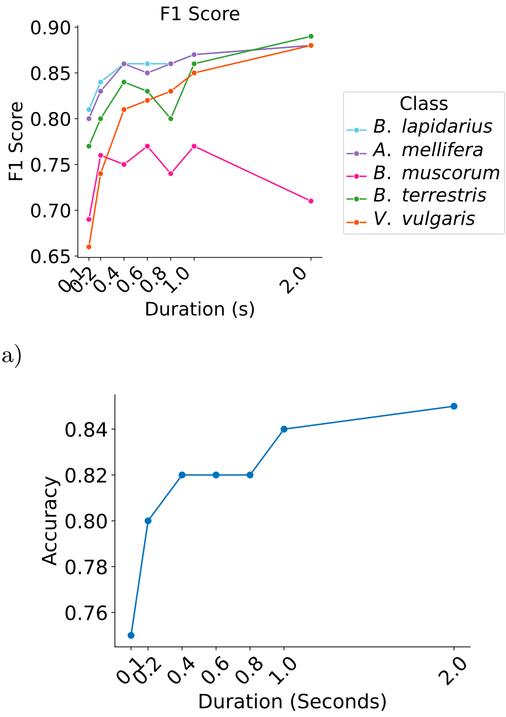

(a)

(b)

FIGURE 5.9: Performance of the hierarchical classification model at different taxonomic levels. (a) Changes in the F1 score with airbourne signal duration (0.1 – 2 seconds) for our five focal species (*V. vulgaris*, *A. mellifera*, *B. lapidarius*, *B. muscorum*, and *B. terrestris*). (b) Variation in overall classification accuracy with signal duration.

separation (0 cm) and the maximum experimentally evaluated distance (18 cm), indicating that the wingbeat-induced harmonic structure remains observable across this range.

A theoretical estimate of the maximum detection range of the proposed radar system was obtained using the monostatic radar range equation

$$R = \left(\frac{P_t G^2 \lambda^2 \sigma}{P_r (4\pi)^3} \right)^{1/4}, \tag{5.2}$$

where P_t and P_r denote the transmitted and received powers, respectively, G is the antenna gain, λ is the operating wavelength, and σ represents the radar cross section (RCS) of the target.

For the experimental configuration, the transmitted power was set to 20 dB and the antenna gain to 19.92 dB. A target positioned at the antenna aperture (0 cm) produced a received signal power of approximately -70 dB, which was taken as an estimate of the minimum detectable received power. The operating wavelength was 1 cm, corresponding to a carrier frequency of 30 GHz. The target RCS was assumed to be 0.002 cm^2, consistent with reported radar cross-section values for bee-sized insects in the literature [16], [98].

Substituting these parameters into the radar range equation yields a theoretical detection range of approximately 55.8 cm. This value represents an idealised upper-bound estimate under free-space assumptions and does not imply reliable experimental detection at this distance.

The range trials were conducted for a single species and were intended to illustrate the detectability of micro-Doppler harmonics at varying distances rather than to establish an empirical maximum detection range or to evaluate classification performance. Under the present measurement conditions, reliable micro-Doppler signatures were experimentally observed up to a distance of 18 cm.

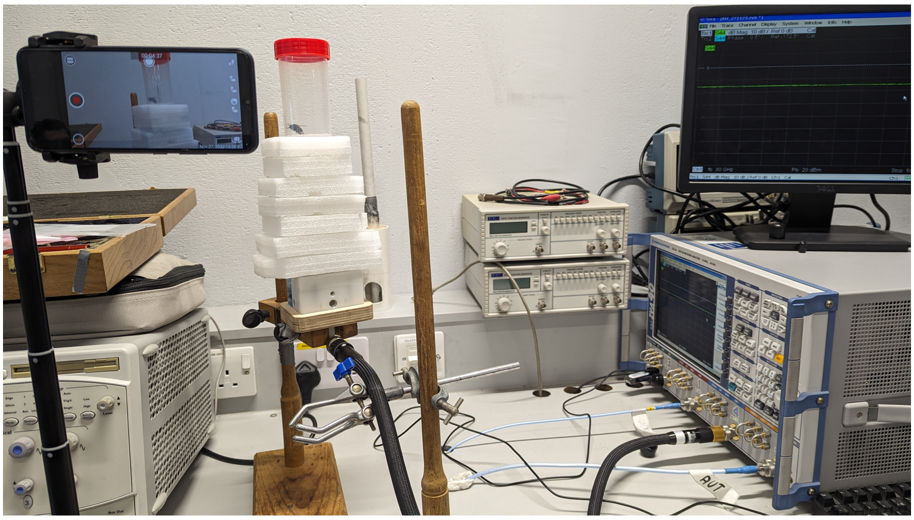

FIGURE 5.10: Photograph of the experimental setup to analyze the efficient range of the proposed radar. A container with live insect positioned on a 2 cm wide thermostyrofoam was utilized to maintain a consistent controlled separation.

5.6 Summary

This study introduces a method capable of effectively analyzing the micro-Doppler spectrum generated by insect wing movements, providing sufficient information for reliable classification at the species level. Although some individuals were incorrectly classified, the findings remain highly encouraging, showing that the system performs dependably at broader taxonomic levels, such as genus or family, indicating strong potential for higher-level identification. Longer wing-flapping durations were found to markedly enhance classification accuracy.

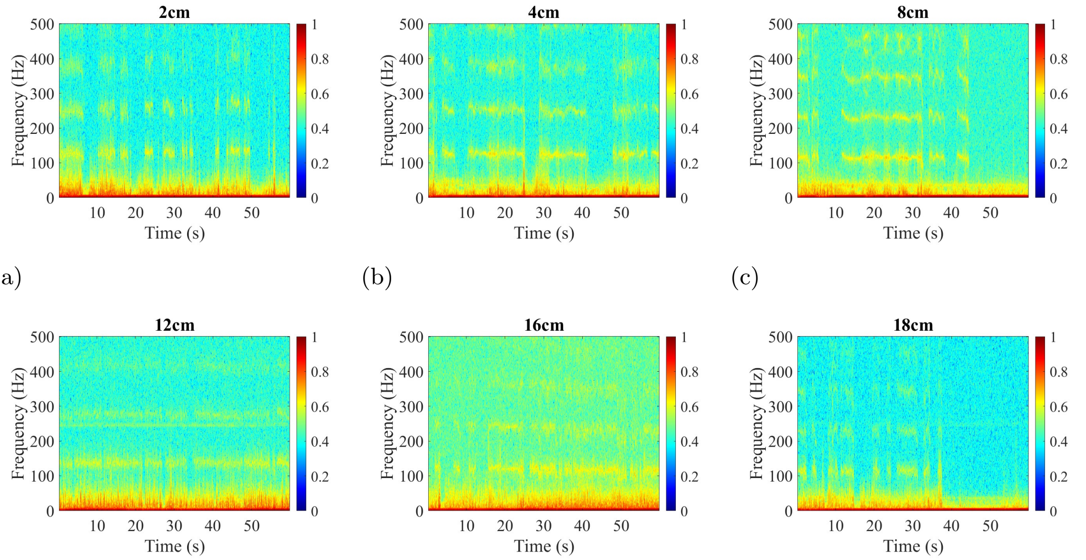

(a) (b) (c) (d)

(e) (f)

Figure 5.11: Time-frequency analysis using Short-Time Fourier Transform on reflected signals from wing flapping *B. terrestris* obtained at distances ranging between 2 and 18 cm from the antenna.

SHAP analysis further revealed that successful species discrimination depends not only on wingbeat frequency but also on additional spectral features, including cepstral coefficients, bandpower across multiple frequency ranges, and several MFCC-derived parameters.

The proposed framework employs a supervised hierarchical classifier in which predictions are made sequentially at the family, genus, and species levels. At each stage the model operates under a closed-set assumption, with the class structure defined during training. In practical deployment, observations from previously unseen taxa can either be assigned to the closest known class or identified as potential novel classes using confidence-based rejection or anomaly-detection strategies. Incorporating such new taxa into the taxonomy-aware classifier subsequently requires the acquisition of labelled training data and model retraining.

Despite this constraint, the framework is scalable because the same feature extraction and learning pipeline is used at all hierarchical levels and does not rely on species-specific analytical or biomechanical models.

The reported classification performance reflects the current dataset and controlled laboratory conditions, with measurements collected from five species and a limited number of individuals.

While the use of ensemble tree-based models can down-weight less informative variables, reduce overfitting risk and physically meaningful micro-Doppler features provides a degree of robustness, the results primarily demonstrate separability within the measured population.

To strengthen the robustness of this approach, future work will incorporate more extensive evaluation strategies such as cross-validation and repeated trials. Broader validation is required to assess performance across the biological and environmental variability encountered in real-world deployment. In particular, future work should include additional species spanning a wider range of body sizes, intra-species variation (e.g., caste and individual differences), and recordings obtained under different geographical locations, temperature conditions, and radar–target geometries.

Future developments may extend the system's capabilities to deliver not only species-level identification and biodiversity monitoring but also detection of behavioral changes through recognition of atypical variations in wingbeat patterns.

Chapter 6

Insect Detection with QPSK and 8-PSK Modulated Signals

This chapter explores integrating biodiversity sensing with communication systems using mm-Wave signals. The study focuses primarily on detecting insect wing-flapping micro-Doppler signatures from modulated signals, being the first step to JSC. This chapter shows how insect wing flapping induces micro-Doppler signatures on a digitally modulated signal, with minimal impact on the constellation of the digital signals. This approach introduces a semi-supervised algorithm that autonomously identifies and segments signal portions exhibiting micro-Doppler effects caused by insect wing flapping. The work presented in this chapter was published in [75].

6.1 Joint Communication and Insect Sensing

If an insect is present, part of the transmitted signal is reflected back toward the source. In a modulated transmission, this creates the challenge of isolating the communication signal from the backscattered echo and processing the sampled data for both information decoding and insect characterization. The goal is to develop a system model capable of capturing object dynamics and properties through temporal, spectral, and Doppler variations in the reflected waveform, thereby supporting efficient monitoring of pollinating insects. The overall concept of joint communication and insect sensing is illustrated in Figure. 6.1.

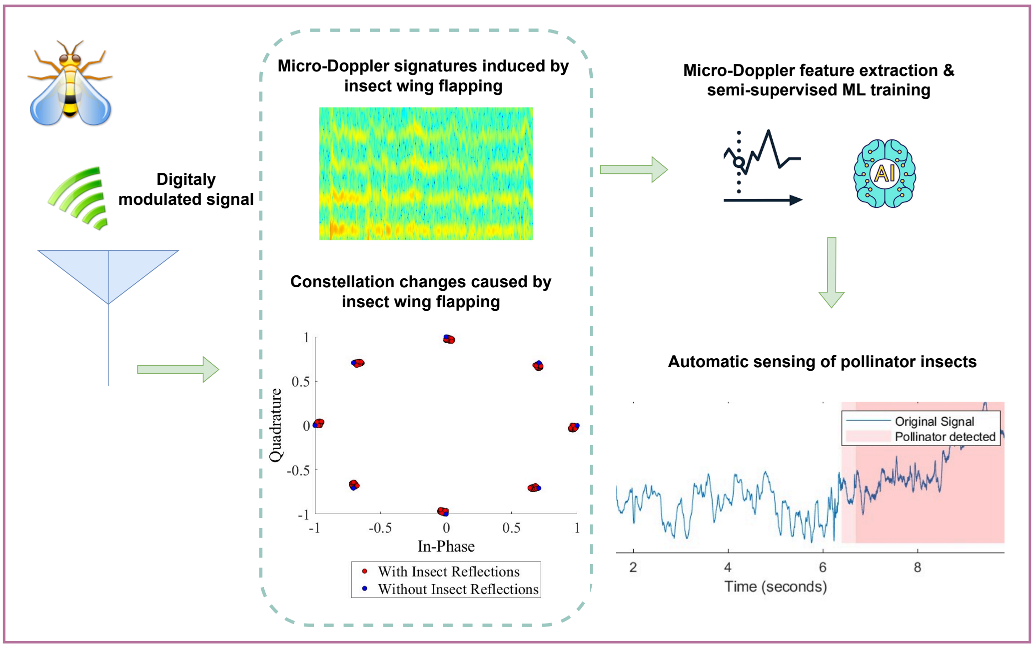

FIGURE 6.1: Joint communication and Insect sensing. Reproduced from [75].

6.1.1 Signal Model

The micro-Doppler signal model for insect detection was introduced in Chapter 3, where the received complex baseband signal was expressed as the superposition of a slowly varying component due to body motion, a rapidly periodic component arising from wing flapping, and additive noise (cf. Eq. (3.3.6)). In the present chapter, this formulation is extended to account for digitally modulated transmission, in which, the downconverted signal at the receiver can be expressed as a combination of the digitally modulated component (s_{DMS}) and reflections originating from noise (which, in this context, also encompasses background reflections from surrounding structures such as walls and the ceiling), insect wing flapping, and body motion, as shown below:

$$A(t)e^{j(\phi(t)+\theta_k)} = s_{\text{DMS}}\left(s_{\text{noise}} + s_{\text{wing flapping}} + s_{\text{body movement}}\right) \tag{6.1}$$

or equivalently,

$$A(t)e^{j(\phi(t)+\theta_k)} = e^{j\theta_k}\left(s_{\text{noise}} + A_w(t)e^{j\phi_w(t)} + A_b(t)e^{j\phi_b(t)}\right) \tag{6.2}$$

Here, the phase of the k-th symbol in the digital modulation scheme is given by $\theta_k =$

$\frac{2\pi k}{M}$, where $k = 0, 1, \ldots, M - 1$, and M denotes the number of possible symbols in the modulation constellation. In this study, 8-Phase Shift Keying (8-PSK) and Quadrature Phase Shift Keying (QPSK) are employed as representative modulation schemes.

The term $\phi_b(t)$ represents the Doppler phase variation induced by the translational motion of the insect's body, while $\phi_w(t)$ captures the micro-Doppler modulation produced by wing flapping. The wing motion is considered harmonic, since both $\phi_w(t)$ and $A_w(t)$ exhibit periodic variations corresponding to the wingbeat cycle, although their evolution need not be strictly sinusoidal.

Equations 6.1 and 6.2 describe a synthetic emulation of a modulated radar return, in which the digitally modulated signal is combined with experimentally measured continuous-wave micro-Doppler signatures. This allows the influence of different modulation schemes on the micro-Doppler signature to be studied while retaining physically realistic insect motion, without requiring a fully implemented JSC measurement.

6.1.2 Semisupervised Insect Detection from Digitally Modulated Signals

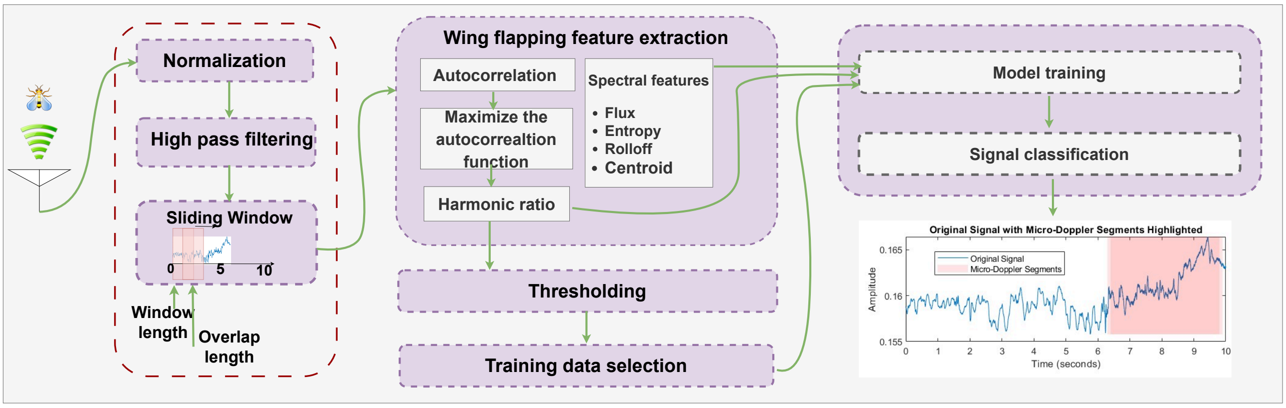

Figure 6.2: Semisupervised insect detection from digitally modulated signal. Reproduced from [75].

Semi-supervised algorithm is employed to extract micro-Doppler segments from digitally modulated signals, as illustrated in Figure 6.2. The received signal is first normalized and high-pass filtered using a 50 Hz cut-off frequency, after which it is segmented into overlapping frames using a Hann window of 0.2 s duration with a 0.1 s overlap. Micro-Doppler features are then extracted from each segment. The features of interest are given in Table 6.1.

Table 6.1: Summary of Extracted Micro-Doppler Features

Feature	Mathematical Definition	Interpretation
Harmonic Ratio	$\Psi(k) = \frac{\sum x(i)x(i-k)}{\sqrt{\sum x(i)^2 \sum x(i-k)^2}},$ $\eta_{\text{HR}} = \max\{\Psi(k)\}$	Measures harmonicity; higher values indicate stronger periodic wingbeat components.
Short-Time Energy (STE)	$E(i) = \frac{1}{N} \sum_{n=0}^{N-1} \lvert x(i+n) \rvert^2$	Reflects instantaneous signal power; highlights active motion frames.
Spectral Spread	$\sigma = \sqrt{\frac{\sum (f_k - \mu)^2 P(k)}{\sum P(k)}},$ $\mu = \frac{\sum f_k P(k)}{\sum P(k)}$	Quantifies how widely spectral energy is distributed around its centroid.
Spectral Flatness	$\text{SF} = \frac{(\prod P(k))^{1/N}}{\frac{1}{N} \sum P(k)}$	Describes how noise-like or tonal the spectrum is (1 = flat/noisy).
Spectral Decrease	$\text{SD} = \frac{\sum_{k=2}^{N} \frac{P(k)-P(1)}{k-1}}{\sum_{k=2}^{N} P(k)}$	Indicates how rapidly spectral amplitude decreases with frequency.

Threshold Determination

The harmonic ratio values are first sorted to establish thresholds that differentiate between signal segments containing micro-Doppler components and those without. The presence of micro-Doppler activity is initially assessed by evaluating the peak value of the normalized autocorrelation function within a defined lag range. Segments exhibiting harmonic ratio values above this threshold are identified as containing insect-induced micro-Doppler signatures and are used to train the model. This enables the machine learning classifier to subsequently recognize and classify all micro-Doppler segments with high accuracy.

Training Data Selection

Signal segments with harmonic ratio values below the lower threshold are designated as background motion samples, while those above the upper threshold represent wing-flapping activity. These two groups are used to train a semi-supervised k-Nearest Neighbors (kNN) classifier. The training data are derived from the same recording being analyzed, ensuring that the classifier adapts to the specific characteristics and dynamics of each signal instance.

The kNN classifier is a nonparametric algorithm that assigns a class label to an unknown sample based on the majority class of its nearest neighbors [99]. It operates in two stages:

first, identifying the samples that are closest to the point under consideration, and second, assigning a class based on the dominant label among those neighbors. Several distance measures can be employed to determine neighborhood proximity, such as the Euclidean or Manhattan distances. In this work, the Euclidean distance metric is used and defined as:

$$D_{\text{Euclid}}(x, y) = \sqrt{\sum_i (x_i - y_i)^2} \tag{6.3}$$

Testing Data Classification

Once trained, the model is applied to the entire signal sequence to classify each segment as either micro-Doppler activity resulting from wing flapping or background noise. The classification performance is then validated by comparing the detected micro-Doppler segments against ground truth observations obtained from synchronized video recordings of the insect's wing motion.

6.1.3 Wing Flapping Frequency Estimation

The fundamental wing flapping frequency is estimated using the Pitch Estimation Filter (PEF) method [87]. The signal $x(t)$ is divided into overlapping frames of length N with an overlap of O samples. For each frame $x_n(t)$, the power spectrum $P(f)$ is obtained using the Fast Fourier Transform (FFT):

$$P(f) = |X(f)|^2, \tag{6.4}$$

where $X(f)$ denotes the Fourier transform of the frame. To enhance periodic components linked to wingbeat harmonics, a logarithmic compression is applied to the spectrum:

$$S(f) = \text{PEF}\big(\log|X(f)|^2\big)\,. \tag{6.5}$$

The spectral envelope $E(f)$ is then estimated and subtracted from the log spectrum to obtain the flattened spectrum $F(f)$:

$$F(f) = \log P(f) - E(f), \tag{6.6}$$

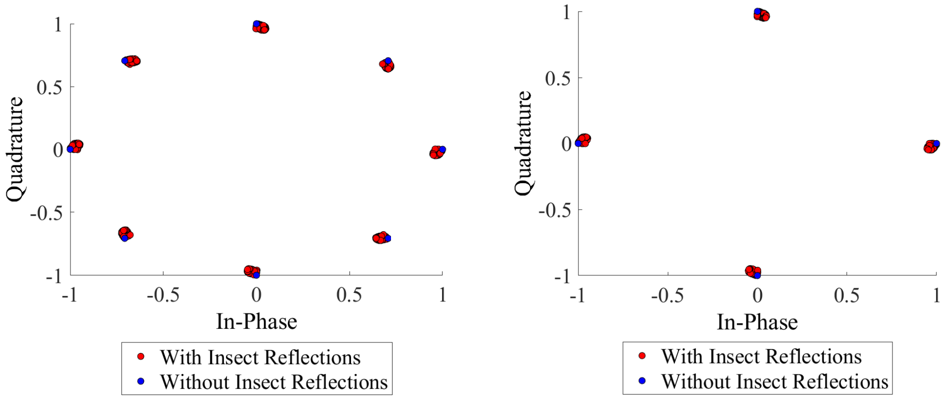

(a) (b)

Figure 6.3: Constellation diagrams showing signal points with (red) and without (blue) insect reflections. (a) PSK 8 (b) QPSK. Reproduced from [75].

and the fundamental frequency f_0 is identified as

$$f_0 = \arg\max_f F(f). \tag{6.7}$$

The logarithmic compression amplifies weak periodic components relative to nonperiodic noise, while the PEF functions as a comb-like filter aligned with the harmonic structure of the wingbeat. The combination of harmonic enhancement and spectral envelope subtraction enables robust estimation of f_0, even under noisy environmental conditions.

6.2 Experimental Observations

Figure 6.3 illustrates the constellation diagrams for 8-PSK and QPSK modulation schemes, comparing signal points in the presence and absence of insect reflections. The introduction of insects causes minor deviations in the constellation points, resulting from micro-Doppler modulations generated by wing flapping. Although these variations are subtle and do not significantly degrade the communication signal quality, their periodic nature enables reliable detection of insect activity when the signal is observed over an extended duration.

Figure 6.4 presents the color-coded classification results obtained from the proposed algorithm (top), compared with the corresponding STFT representations for each measurement (bottom).

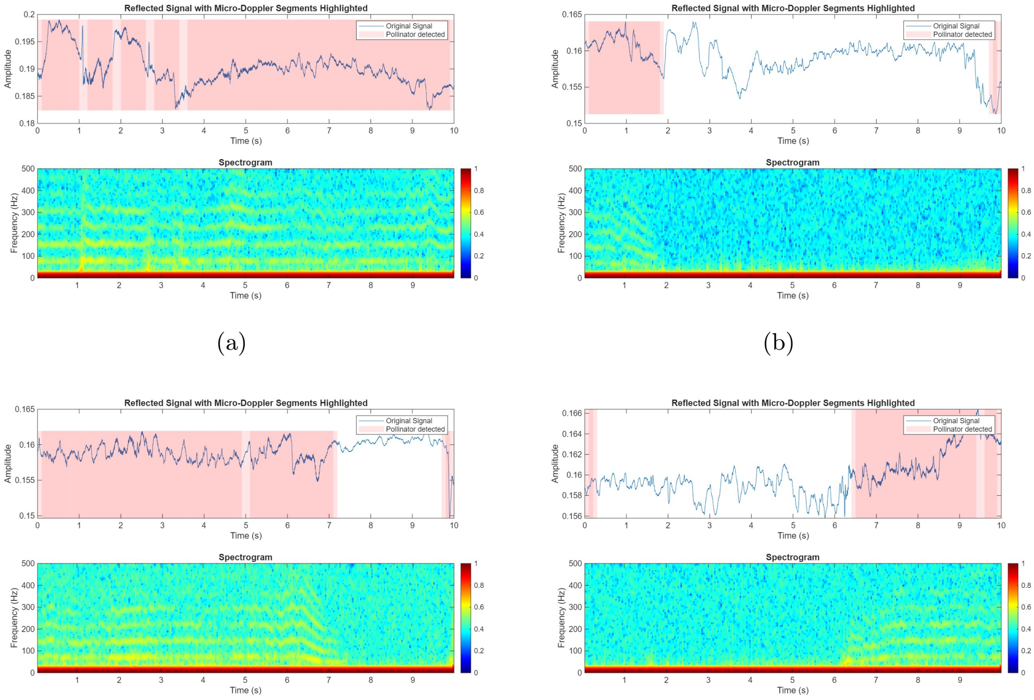

(a) (b)

(c) (d)

Figure 6.4: Spectrograms of wing-beat modulated micro-Doppler signals and classification results. (a) Continuous wing flapping throughout. (b) Wing flapping for the first 2 seconds, then stopping. (c) Wing flapping for the first 7 seconds. (d) No flapping for 7 seconds, followed by 3 seconds of wing flapping. The classification algorithm correctly identified all segments, verified by video footage. Reproduced from [75].

Figure 6.4(a) illustrates a case where a wingbeat-modulated micro-Doppler signature is observed throughout the entire sample duration. The proposed classification algorithm consistently labeled this segment as wing flapping, in agreement with the corresponding video validation. In Fig. 6.4(b), the micro-Doppler effect appears only during the first two seconds before fading out, which aligns with the classification results indicating wing flapping during the initial 2 s followed by insect presence without flapping. Video observations confirmed this behavior, showing the insect ceasing wing motion after two seconds.

In Fig. 6.4(c), the insect exhibits continuous wing flapping for approximately 7 s, as evidenced by the persistent micro-Doppler pattern in the STFT. The classification algorithm likewise detected wing flapping for the same interval. Conversely, Fig. 6.4(d) corresponds to a scenario where the insect moved without flapping during the first seven seconds, initiating wingbeats only in the final three seconds. Both the STFT and the classification algorithm correctly captured this transition, identifying wing flapping exclusively in the

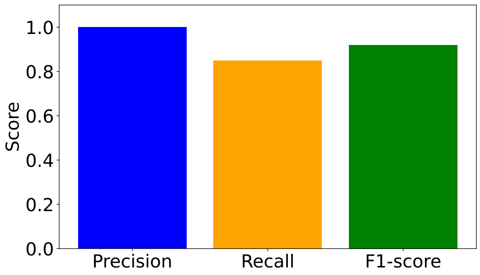

FIGURE 6.5: Performance metrics of the proposed method. Reproduced from [75].

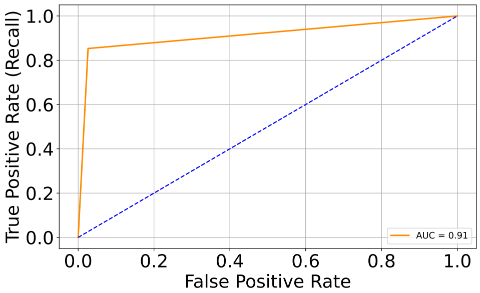

FIGURE 6.6: ROC curve of the proposed method. Reproduced from [75]

last 3 s. Across all 60 analyzed signal segments, the algorithm's classifications matched the ground truth obtained from video recordings.

6.3 Performance Metrics

After classification, the segment-wise labels indicating the presence or absence of micro-Doppler effects were compared with the corresponding ground truth annotations. Performance metrics were calculated using 0.2-second signal segments derived from 60 reflected recordings collected from *A. mellifera*, *B. terrestris*, and *V. vulgaris*. Each recording lasted 10 s and contained 10,001 samples. Figure 6.5 summarizes the performance of the proposed micro-Doppler classification algorithm. The bar chart displays the Precision, Recall, and F1-score values. A Precision value close to 1.0 indicates that nearly all segments identified as wing flapping were correctly classified. The slightly lower Recall value suggests that most true wing flapping events were detected, though a few were missed. The high F1-score, reflecting the harmonic mean of precision and recall, demonstrates the strong overall accuracy and reliability of the proposed algorithm in detecting micro-Doppler activity.

Figure 6.6 presents the Receiver Operating Characteristic (ROC) curve for the proposed micro-Doppler signal classification algorithm. The curve illustrates the relationship between the True Positive Rate (Recall) and the False Positive Rate across different decision thresholds. The Area Under the Curve (AUC) is approximately 0.91, demonstrating the algorithm's excellent capability to distinguish between positive and negative classes. The curve's proximity to the ideal upper-left corner further confirms the strong discriminative performance of the classifier.

6.4 Wing-flapping Frequency Analysis

Figure 6.7 illustrates the wingbeat frequencies extracted from signal segments identified as containing micro-Doppler effects for three insect species: *A. mellifera*, *B. terrestris*, and *V. vulgaris.* The plot displays the frequency distributions for each species, showing both central tendencies and variability. Distinct frequency ranges are evident across species, with *A. mellifera* exhibiting the highest median wingbeat frequency, followed by *V. vulgaris* and *B. terrestris.*

Workers of *A. mellifera* typically weigh about 0.09 g and flap their wings at approximately 230 Hz, with an average wing area of 0.6 cm^2 and a wing loading near 0.15 g/cm^2 [57]. In contrast, *B. terrestris* workers are about two to three times heavier (0.2–0.3 g), exhibit wingbeat frequencies around 150–160 Hz, have a larger wing area exceeding 2 cm^2, and maintain a moderate wing loading of 0.1–0.15 g/cm^2 [100]. *V. vulgaris* workers, comparable in mass to *A. mellifera* (0.08–0.09 g), possess similar wing morphology (about 0.6 cm^2 area and 0.15 g/cm^2 loading) but display wingbeat frequencies intermediate between those of the honeybee and bumblebee [57].

The estimated wingbeat frequencies correspond closely with species-specific body size and flight biomechanics, consistent with the relationship expressed in Equation 2.2. The observed variability reflects natural differences in wing dynamics among species. Although explicit species classification was not performed, the distinct frequency distributions indicate the potential for distinguishing closely related species such as *A. mellifera*, *B. terrestris*, and *V. vulgaris.*

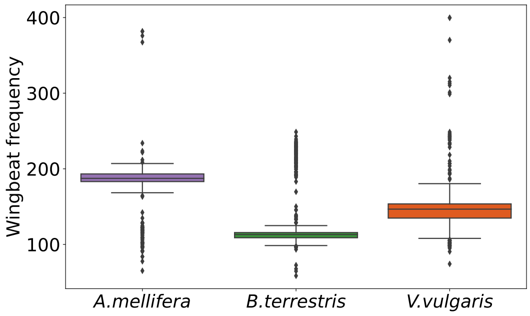

FIGURE 6.7: Extracted wing-beat frequencies for *A. mellifera*, *B. terrestris*, and *V. vulgaris* from micro-Doppler signal portions. Reproduced from [75].

6.5 Summary

This chapter demonstrated the simultaneous dual functionality of communication and insect sensing within a single system. The methodology proved effective for both continuous-wave and digitally modulated signals. The proposed classification algorithm successfully identified signal segments associated with wing flapping, with validation performed using synchronized video recordings. Performance indicators, including high Precision, Recall, F1-scores, and an AUC of 0.91 highlight the robustness and reliability of the approach.

The realisation of a fully modulated radar sensing system, in which the micro-Doppler is measured directly on the communication waveform, forms part of future work and will enable validation under real-time and field-operating conditions.

Although the measurements in this work are based on CW radar, the proposed micro-Doppler feature extraction and classification framework is directly transferable to FMCW waveforms. In an FMCW system, body motion would be represented in the range–Doppler domain, while wing flapping would appear as micro-Doppler modulation on the range-resolved target. After range gating, the same temporal and spectral features can be extracted. Direct validation using real FMCW measurements, including the influence of chirp design and hardware effects, is part of future work.

The technique provides a straightforward means of integrating a pollinator monitoring capability into an existing mmWave communication link without compromising its primary telecommunication performance. With the ongoing adoption of Open Radio Access Network (O-RAN) architectures, this approach could be readily implemented in existing base station infrastructures, enabling large-scale biodiversity monitoring, particularly within urban environments.

Chapter 7

Virtual Modes for Compact Multi-Target AoA Estimation

Although the primary objective of this thesis is micro-Doppler–based insect classification, real-world ecological monitoring would also benefit from accurate spatial localization, particularly in multi-insect scenarios. Traditional SISO radar systems provide temporal signatures but lack directional awareness. AoA estimation could address this limitation. However, conventional phased arrays are often too large, power-intensive, and impractical for deployment in natural environments such as crop fields or pollinator habitats, and densely packed antennas introduce non-negligible mutual coupling.

Recent advances in SM antenna design offer a promising alternative: compact, multi-port antennas that leverage spherical harmonic expansions to achieve high angular resolution with minimal hardware complexity [26]. Motivated by this potential, this chapter evaluates the applicability of ESPRIT for AoA estimation in SM-based antennas, alongside classical approaches such as delay-and-sum (DAS), MVDR, and MUSIC. Among these, ESPRIT offers attractive advantages low computational cost, minimal memory footprint, and fast convergence making it ideal for compact low-power ecological sensing devices. However, its performance depends on the presence of a Vandermonde structure in the phase progression across antenna ports. Lack of Vandermonde structure reduces the degrees of freedom and limiting the achievable angular resolution compared with algorithms such as MUSIC. Furthermore, the achievable resolution of compact antennas is fundamentally constrained by limited physical aperture, bandwidth, and the increased losses associated with generating higher-order modes.

(a) (b)

FIGURE 7.1: Spherical Modes Beamforming (SMB): (a) Exploded-view of the proposed antenna. Dimensions (in mm): feed points P1 = P2 = 16.5, P3 = 0, P4 = P5 = 9.5, $R_1 = 36.9$, $R_2 = 28$, $R_3 = 26.9$, $r_c = 5.25$, radius of the vias (shown in red dots) $r_p = 0.25$, $d_p = 15$, $\alpha_1 = 225°$, $\alpha_2 = 30°$; and (b) phase patterns reproduced from [105].

To address these trade-offs, this chapter introduces a novel virtual mode (VM) framework. The concept synthesises additional effective spherical modes without requiring additional physical antenna elements, thereby expanding the available angular degrees of freedom and enhancing spatial resolution. By reconstructing a richer modal basis, the VM approach improves multi-target AoA estimation performance while preserving low hardware complexity enabling high-resolution subspace algorithms such as ESPRIT to operate effectively under stringent platform constraints.

Key findings from this work have been published in [101], [102] and [103].

7.1 SM Based AoA Estimation

SMs are fundamental solutions to Maxwell's equations expressed in spherical coordinates, representing specific patterns of electromagnetic field distributions that arise in systems with spherical symmetry [104].

As described in [105], the SMB technique allows for seamless beam steering across the full azimuthal plane by simultaneously exciting multiple SMs. Each of these modes exhibits a distinct phase pattern, and their superposition leads to constructive interference in targeted directions.

In contrast to conventional antenna arrays that rely on spatially separated elements to form beams, the SMB design employs collocated radiators. Directional control is achieved by rotating the electric field around the antenna rather than depending on element spacing. This design enables precise AoA estimation while significantly reducing the overall antenna size. As illustrated in Fig. 7.11 (a), the SMB antenna from [105] uses five feeding ports to excite five orthogonal omnidirectional SMs, all within a compact structure measuring just 0.55λ in its largest dimension.

Figure 7.11 (b) illustrates the phase profiles of radiation patterns produced by five SMs with indices $m = -3, -2, 0, +2, +3$. The modes with $m = \pm 3$ exhibit three full phase rotations around the azimuth, while $m = \pm 2$ show two rotations. The $m = 0$ mode corresponds to the fundamental mode with a uniform phase across all directions.

Modes with $m = \pm 1$ are not used due to practical constraints. These modes produce omnidirectional patterns, but their radiation is primarily directed along the vertical axis (toward the poles), emitting right-hand circular polarization in one direction and left-hand in the opposite. This results in a bidirectional radiation pattern that lies in a different plane compared to the other modes, making them unsuitable for the intended beamforming application.

The signal received at each antenna port is added with white Gaussian noise $n(t)$. Then the received vector can be represented as

$$\mathbf{x}(t) = \mathbf{E}\mathbf{s}(t) + \mathbf{n}(t) \tag{7.1}$$

where $\mathbf{x}(t)$ is the received vector output, $\mathbf{s}(t)$ is the signal vector, $\mathbf{n}(t)$ is the noise vector, and $\mathbf{E}$ is the array manifold that consists of steering vectors corresponding to each source given as

$$\mathbf{E} = \begin{bmatrix} \mathbf{e}(\theta_1) & \mathbf{e}(\theta_2) & \cdots & \mathbf{e}(\theta_D) \end{bmatrix} \tag{7.2}$$

$$\mathbf{e}(\theta_i) = \begin{bmatrix} \mathbf{e}_1(\theta_i) & \mathbf{e}_2(\theta_i) & \mathbf{e}_3(\theta_i) & \mathbf{e}_4(\theta_i) & \mathbf{e}_k(\theta_i) \end{bmatrix}^H . \tag{7.3}$$

The theoretical radiation pattern of the proposed multimode antenna containing k ports can be simplified as:

$$\mathbf{e}_k(\theta) = e^{-jM_k\theta} \tag{7.4}$$

where M_k represents the phase delays at the k^{th} port to a reference port. For the investigated case, $k = 1, 2, \cdots, 5$, which corresponds to the antenna implemented in [105]. Phase delays of each port are $\pm 3, \pm 2, 0$, respectively, which corresponds to the index number of the SMs azimuthal phase changes m.

7.2 Spherical Mode-Based Antenna AoA Techniques: Multi-Target Detection Performance

The power spectra for DAS, MVDR, and MUSIC for the SMs driven multi-port antenna can be written as:

$$P_{\text{DAS}}(\theta) = \mathbf{e}^H(\theta)\,\mathbf{R}_x\,\mathbf{e}(\theta) \tag{7.5}$$

$$P_{\text{MVDR}}(\theta) = \mathbf{w}^H(\theta)\,\mathbf{R}_x\,\mathbf{w}(\theta) \tag{7.6}$$

$$P_{\text{MUSIC}}(\theta) = \frac{1}{\mathbf{e}^H(\theta)\,\mathbf{U}_n\mathbf{U}_n^H\,\mathbf{e}(\theta)} \tag{7.7}$$

where the MVDR weight vector is given by

$$\mathbf{w}(\theta) = \frac{\mathbf{R}_x^{-1}\mathbf{e}(\theta)}{\mathbf{e}^H(\theta)\,\mathbf{R}_x^{-1}\mathbf{e}(\theta)}. \tag{7.8}$$

Here, $\mathbf{U}_n$ denotes the noise–subspace eigenvectors obtained from the eigen-decomposition of the spatial covariance matrix $\mathbf{R}_x$, computed using (4) or derived from full-wave simulation results. ESPRIT is distinguished among AoA techniques by its search-free formulation, as it avoids exhaustive scanning of the spatial spectrum. The method exploits the translational invariance of a structured antenna array by partitioning it into two identical, displaced subarrays. Owing to this geometry, the corresponding signal subspaces are related through a rotational transformation. ESPRIT estimates the angles of arrival by directly solving for this rotation using pairs of matched sensors (often referred to as sensor doublets), thereby achieving efficient and accurate AoA estimation without spectral peak searching. While ESPRIT is highly effective for uniformly spaced arrays, applying it to SM-based multiport antennas is more complex. The challenge lies in the non-linear

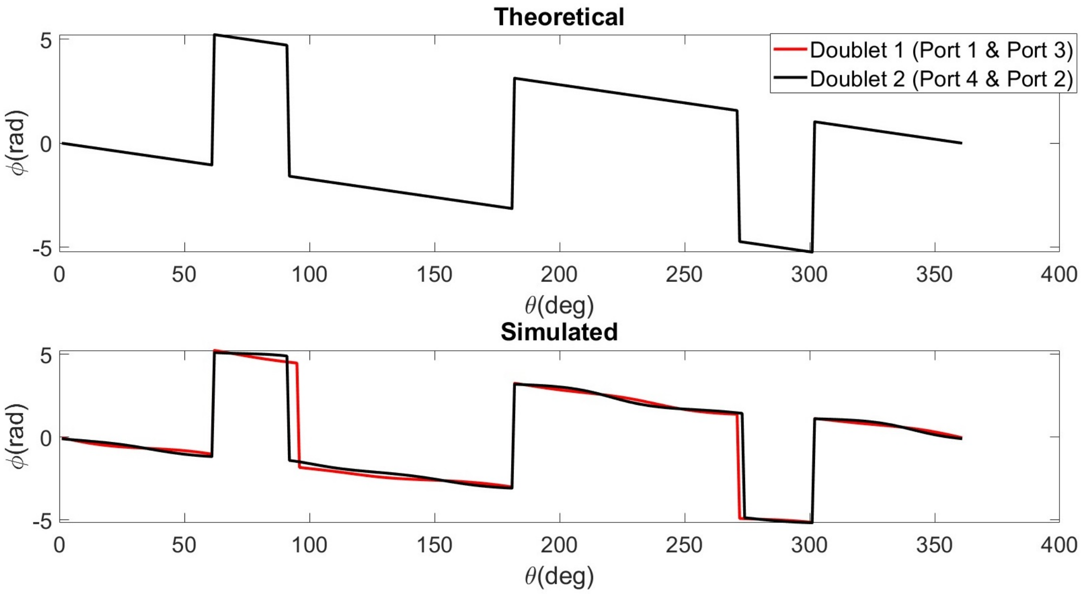

FIGURE 7.2: Phase differences between chosen doublets: (a) theoretical; and (b) full-wave simulated results. Reproduced from [101].

and mode-dependent phase delays between ports, which disrupt the required translational symmetry. As a result, adapting ESPRIT to such antennas presents an interesting research problem.

For the discussed 5-port SM driven beamforming antenna, the phase patterns from ports 1 and 3 are grouped as a first doublet, while patterns of port 4 and port 2 form doublet 2. The phase difference between these doublets is illustrated in Fig. 7.2 for both theoretical and simulated scenarios. Notably, in the theoretical scenario, the phase difference between the two doublets remains consistent across all angles. However, in the full-wave simulated case, the phase differences exhibit variability across different angles. This is most likely due to small inaccuracies between the ports generated patterns in the antenna implementation.

Given the received signal at each antenna port, the signal space can be decomposed into two subspaces: the signal subspace and the noise subspace. The decomposition usually employs the eigenvectors of the covariance matrix of the received signals.

Mathematically, if $\mathbf{E}_s$ represents the matrix containing the eigenvectors of the signal subspace, the invariance between the two subarrays can be expressed as:

$$\mathbf{E}_{s_1} = \mathbf{E}_{s_2}\mathbf{R} \tag{7.9}$$

where $\mathbf{E}_{s_1}$ and $\mathbf{E}_{s_2}$ are the portions of $\mathbf{E}_s$ corresponding to the two doublets; $\mathbf{R}$ is a diagonal matrix whose diagonal elements contain information about the AoAs.

Table 7.1: Computational complexity comparison of different methods.

Method	**Main computational steps**	**Overall complexity**
DAS	Sample covariance computation $O(SK^2)$, angular grid search $O(PK^2)$	$O(SK^2 + PK^2)$
MVDR	Sample covariance computation $O(SK^2)$, matrix inversion $O(K^2)$, angular grid search $O(PK^2)$	$O(SK^2 + K^2 + PK^2)$
MUSIC	Sample covariance computation $O(SK^2)$, eigenvalue decomposition $O(K^3)$, angular grid search $O(PK^2)$	$O(SK^2 + K^3 + PK^2)$
ESPRIT	Sample covariance computation $O(SK^2)$, eigenvalue decomposition $O(K^3)$, AoA estimation via rotational invariance $O(D^3)$	$O(SK^2 + K^3 + D^3)$

Table 7.1 shows the general computational complexity associated with each classical AoA method on the multiport antenna, where K is the number of ports, D is the number of sources, S is the number of snapshots, and P is the number of possible angles used to search over a grid of angles.

All AoA computations were carried out using MATLAB R2022a (64-bit) on a Windows 10 Pro (64-bit) system, featuring an 11th Generation Intel® Core™ i5-1135G7 processor running at 2.40 GHz and 8 GB of RAM. The radiation patterns were generated with a full-wave electromagnetic solver, namely CST Microwave Studio. The examined AoA estimation approaches were applied to both the analytical expression in (7.4) and the CST-simulated radiation patterns. Figure 7.3 presents the results for single-source and multi-source scenarios in subfigures (a) and (b), respectively.

Fig. 7.3 (a) illustrates the AoA estimation for a single source arriving from an angle of 100°, with an Signal-to-Noise Ratio (SNR) of 20 dB and 100 snapshots considered. The results indicate that all four methods successfully and accurately estimate the angle of arrival of the incident signal. Fig. 7.3 (b) presents the concurrent detection of four sources located at 0°, 90°, 180°, and 270°. It should be noted that the ESPRIT implementation is unable to resolve multiple sources, as its subarray comprises only two elements. All incident signals share identical amplitudes and an SNR of 20 dB, with the AoA estimation again performed using 100 snapshots. The results demonstrate that all four sources are correctly identified by the AoA estimation techniques. Among the grid-search-based approaches, DAS exhibits the lowest angular resolution, whereas MUSIC achieves the highest resolution.

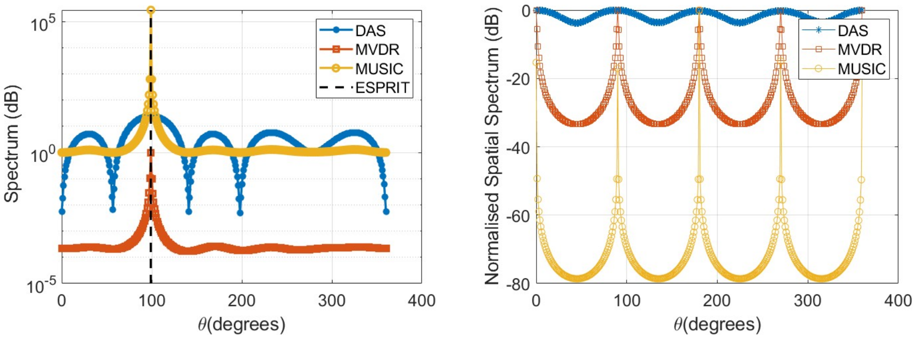

(a) (b)

FIGURE 7.3: Source detection using the theoretical SMs:(a) Single source (b) Multiple source. Reproduced from [101].

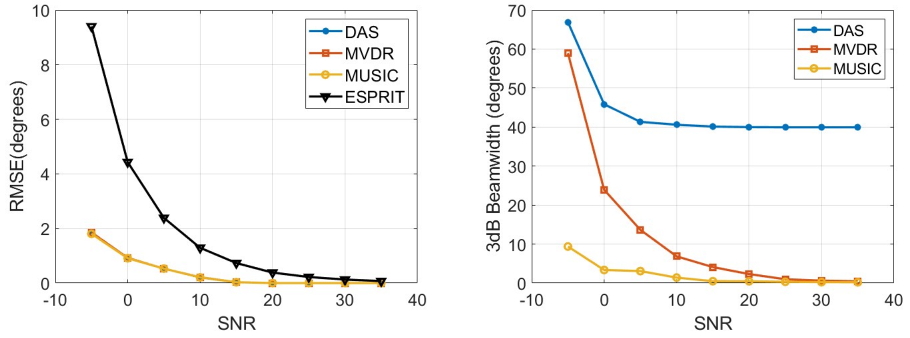

(a) (b)

FIGURE 7.4: AoA estimation using theoretical analysis (a) RMSE vs SNR (b) Resolution vs SNR. Reproduced from [101].

Fig. 7.4 (a) and (b) depict the accuracy and resolution for varying SNR. The accuracy is quantified using the Root Mean Square Error (RMSE), formulated as:

$$\mathrm{RMSE} = \sqrt{\frac{1}{NM_C}\sum_{i=1}^{N}\sum_{m_c=1}^{M_C}(\theta_i - \hat{\theta}_i, m_c)^2} \tag{7.10}$$

where M_C represents the number of Monte Carlo simulations, and N is the number of directions utilized in Root Mean Square Error (RMSE) calculations. For this study, M_C is set to 100, and angles spanning from 0° to 360°, separated by 1°, were used to compute the RMSE.

As shown in Fig. 7.4 (a), ESPRIT demonstrates a comparatively larger RMSE at very low SNR levels. Nevertheless, its estimation accuracy improves progressively as the SNR increases. By comparison, the remaining methods exhibit nearly constant accuracy over the full SNR range. Figure 7.4 (b) illustrates the dependence of angular resolution on SNR

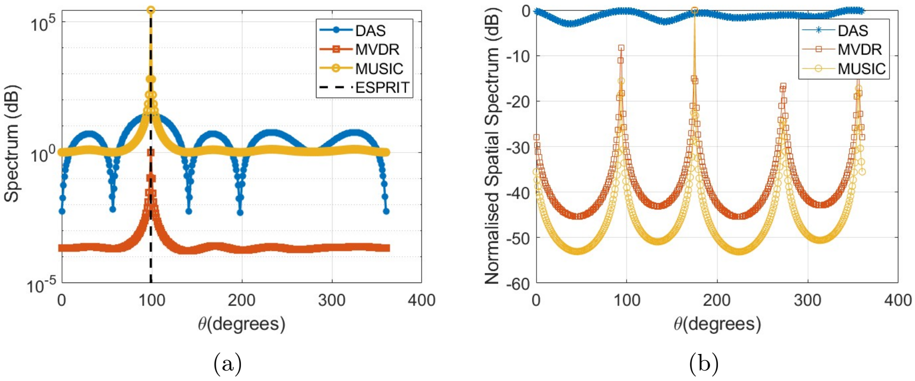

FIGURE 7.5: Source detection using the simulated SMs: (a) Single source (b) Multiple source. Reproduced from [101].

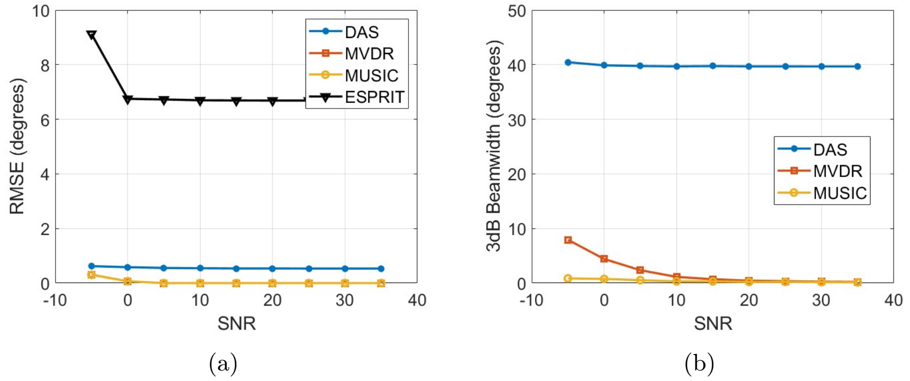

FIGURE 7.6: AoA estimation using radiation patterns (a) RMSE vs SNR (b) Resolution vs SNR. Reproduced from [101].

TABLE 7.2: Execution time comparison of AoA estimation methods.

Method	**Time (s) @ 1° resolution**	**Time (s) @ 0.1° resolution**
DAS	0.002886	0.0099
MVDR	0.0030	0.010
MUSIC	0.0042	0.062
ESPRIT	0.00296	0.00296

for various search-based AoA estimation algorithms. The resolution is evaluated using the 3 dB beamwidth, defined as the angular span of the main lobe between the points where the received power drops to half of its maximum value, thus serving as a direct indicator of angular resolution. It is evident that DAS produces a wider 3 dB beamwidth, while MUSIC achieves the narrowest one. As a result, DAS provides the lowest angular resolution, whereas MUSIC offers the highest resolution.

Fig. 7.5 illustrates the detection of a single source located at 0° as well as multiple sources at 0°/360°, 90°, 180°, and 270°, using far-field radiation patterns obtained at each port of the multiport antenna through CST simulations. The results demonstrate that, under CST-simulated conditions, all considered methods are able to accurately estimate the angles of arrival. In addition, DAS, MVDR, and MUSIC successfully resolve all four sources simultaneously.

Figure 7.6 presents the accuracy and angular resolution as functions of SNR. In comparison with the theoretical cases, ESPRIT exhibits a noticeably higher RMSE across the full angular range from 0° to 360° when simulated phase patterns are employed. This degradation is likely attributable to phase inconsistencies between the subarrays. Moreover, the estimation accuracy of all methods converges more rapidly than in the analytical scenarios. Both MVDR and MUSIC maintain accuracy levels comparable to those observed in the theoretical cases, despite the presence of phase imperfections. Similarly, the resolution-versus-SNR behavior of DAS, MVDR, and MUSIC closely matches the performance obtained in the theoretical results shown in Fig. 7.4.

Table 7.2 summarizes the computational time required by the different AoA estimation techniques. The results indicate that MUSIC is the most computationally demanding approach, incurring the highest CPU processing time. In contrast, for a 1° grid search, DAS demonstrates superior computational efficiency, requiring substantially less CPU time than the remaining methods. This observation is consistent with the complexity analysis reported in Table 7.1, which shows that DAS involves considerably fewer computational operations compared to the other techniques. However, this computational advantage comes at the expense of reduced angular resolution, highlighting an inherent trade-off between processing efficiency and estimation accuracy.

ESPRIT is commonly preferred for AoA estimation owing to its high resolution and estimation accuracy. One of its key advantages is the elimination of angular grid searches, which leads to reduced computational complexity and faster execution. Nevertheless, when ESPRIT is directly employed with a multiport antenna, its AoA estimation performance may degrade due to phase mismatches between the selected element pairs. In addition, the maximum number of resolvable sources is effectively reduced by half.

In summary, among the conventional AoA estimation techniques applied to multiport spherical-modes-driven beamsteering antennas, MUSIC stands out as the most suitable choice when high accuracy is of primary importance. ESPRIT offers a practical alternative by reducing computational complexity at the expense of DoF and estimation accuracy.

Improving angular resolution requires the excitation of additional modes; however, exciting a large number of modes within a limited physical volume may adversely affect bandwidth and lead to increased losses.

7.3 Virtual Modes for Compact Systems and Multiple Target Detection

Consider an SMB antenna receiving D narrowband signals S_d arriving from distinct directions $\{\theta_d, d = 1, 2, \ldots, D\}$, each with power σ_d^2. The radiation pattern of the antenna in the azimuthal plane is characterized by a set of integers m, which specify the phase variations across the antenna's ports. The radiation pattern of the k^{th} mode is given by:

$$\mathbf{e}_k(\theta) = e^{-jm_k\theta}, \tag{7.11}$$

where m_k is the k^{th} element of the set m. The received signal at the SMB antenna can be represented by the column vector $\mathbf{X}_m$, expressed as:

$$\mathbf{X}_m = \sum_{d=1}^{D} S_d \mathbf{E}_m(\theta_d) + \mathbf{n}_m, \tag{7.12}$$

where $\mathbf{E}_m(\theta)$ is the antenna response vector containing elements $e^{-jm_k\theta}$ for each $m_k \in m$, and $\mathbf{n}_m$ is an additive white Gaussian noise vector with covariance $\sigma^2\mathbf{I}$.

The covariance matrix of the received signal $\mathbf{X}_m$ is given by:

$$\mathbf{R}_{X_m}(\theta) = E[\mathbf{X}_m\mathbf{X}_m^H] = \sum_{d=1}^{D} \sigma_d^2 \mathbf{E}_m(\theta_d)\mathbf{E}_m^H(\theta_d) + \sigma^2\mathbf{I}, \tag{7.13}$$

where $\mathbf{E}_m(\theta_d)\mathbf{E}_m^H(\theta_d)$ yields phase differences between the elements of m, represented as $e^{j\theta(m_i - m_j)}$ for each $m_i, m_j \in m$.

The concept of virtual modes is introduced through the pairwise differences between the phases of the antenna ports. These phase differences define a new set of effective modes, expanding the system's DoF without physically increasing the number of antenna elements. The set of all pairwise differences between the elements of m, denoted as $m_{\text{diff}} = \{m_i - m_j | m_i, m_j \in m\}$, forms the virtual mode set.

Sparse sensing techniques, utilizing second-order statistics, have been explored in various sparse arrays with different sensor arrangements [106]–[109]. Based on this, by vectorizing the covariance matrix $\mathbf{R}_{X_m}$, we can express the received signals as an equivalent form for a virtual antenna system. The vectorized covariance matrix is:

$$\mathbf{X}_{m_{\text{diff}}} = (\mathbf{E}_m^* \odot \mathbf{E}_m)\mathbf{P} + \sigma^2 \tilde{\mathbf{e}}, \tag{7.14}$$

where $\mathbf{E}_m^* \odot \mathbf{E}_m$ represents the Khatri-Rao product, which acts as the antenna response matrix for the virtual mode. The vector $\tilde{\mathbf{e}}$ accounts for the noise contribution, while $\mathbf{P}$ is a column vector of signal powers. This transformation enables the interpretation of the system as a virtual multi-port antenna, with each port corresponding to a different virtual mode in m_{diff}.

7.4 AoA Estimation Using Virtual Spherical Modes

The covariance-derived signal $\mathbf{X}_{m_{\text{diff}}}$ inherently captures data correlations, which effectively causes it to behave as a single snapshot. As a result, the covariance matrix formed from the received signal of this equivalent virtual SMB antenna is rank one. In order for AoA estimation techniques such as MUSIC [70] and ESPRIT [71] to resolve multiple sources, a higher-rank covariance matrix is required.

ESPRIT, in particular, exploits the rotational invariance property through the use of identical sensor pairs, commonly referred to as doublets. Extending this concept to the signal matrix $\mathbf{X}_m$ of multiport antennas introduces specific challenges [110]. This difficulty arises because the antenna manifold $\mathbf{E}_m$ embedded in $\mathbf{X}_m$ does not exhibit the Vandermonde structure required by ESPRIT. In contrast, when the differential-domain signal $\mathbf{X}_{m_{\text{diff}}}$ is considered, the resulting manifold $(\mathbf{E}_m^* \odot \mathbf{E}_m)$ assumes a Vandermonde form, thereby making it suitable for application within the ESPRIT framework.

Nevertheless, the covariance-derived signal $\mathbf{X}_{m_{\text{diff}}}$ inherently contains data correlations, which complicates the direct application of ESPRIT and MUSIC, as these algorithms typically assume mutually uncorrelated sources for reliable AoA estimation. To properly handle the correlations embedded in $\mathbf{X}_{m_{\text{diff}}}$, a decorrelation procedure is therefore required.

Hermitian symmetry implies that

$$\mathbf{x}_{m_{\text{diff}}}\bigg|_{d} = \mathbf{x}_{m_{\text{diff}}}\bigg|_{-d}^{*}, \quad d \in m_{\text{diff}},$$

which follows from the property $|w(d)|= |w(-d)|$ for all $d \in m_{\text{diff}}$. Leveraging this symmetry enables the construction of a positive semidefinite Toeplitz matrix $\mathbf{R}$ [108], thereby ensuring an appropriate matrix rank—an essential requirement for high-resolution AoA estimation algorithms to operate effectively. The matrix $\mathbf{R}$ is obtained by reshaping $\mathbf{X}_{m_{\text{diff}}}$ as follows:

$$\mathbf{R} = \begin{bmatrix} [\mathbf{X}_{m_{\text{diff}}}]_{L} & [\mathbf{X}_{m_{\text{diff}}}]_{L-1} & \cdots & [\mathbf{X}_{m_{\text{diff}}}]_{1} \\ [\mathbf{X}_{m_{\text{diff}}}]_{L+1} & [\mathbf{X}_{m_{\text{diff}}}]_{L} & \cdots & [\mathbf{X}_{m_{\text{diff}}}]_{2} \\ \vdots & \vdots & \ddots & \vdots \\ [\mathbf{X}_{m_{\text{diff}}}]_{2L-1} & [\mathbf{X}_{m_{\text{diff}}}]_{2L-2} & \cdots & [\mathbf{X}_{m_{\text{diff}}}]_{L} \end{bmatrix}, \tag{7.15}$$

where $L = (|\mathbf{m}_{\text{diff}}|+1)/2$, with $|\mathbf{m}_{\text{diff}}|$ representing the cardinality of the set $\mathbf{m}_{\text{diff}}$. Applying high-resolution algorithms such as MUSIC and ESPRIT to $\mathbf{R}$ enables the resolution of $L-1$ uncorrelated sources. With the proposed sparse-based approach, for an SMB antenna with M SM, the maximum number of identifiable sources $L-1$ can be constrained as $M-1 < L-1 \leq (M(M-1))/2$.

7.5 Virtual Mode Set and Redundancy

Virtual modes expand the system's effective DoF by creating new modes derived from the differences between the original modes. This allows the antenna system to simulate additional functionality without the need for more spherical modes.

The redundancy arises when certain phase differences repeat in the virtual mode set m_{diff}, i.e. when a given virtual mode can be synthesised by more than one pair of spherical modes. To quantify this, we define a redundancy function $w(d)$, which counts the number of occurrences of a particular difference d in m_{diff}. If a phase difference d appears multiple times, it increases the redundancy, effectively reducing the system's DoF.

For an SMB antenna with M spherical modes, the redundancy function at zero is

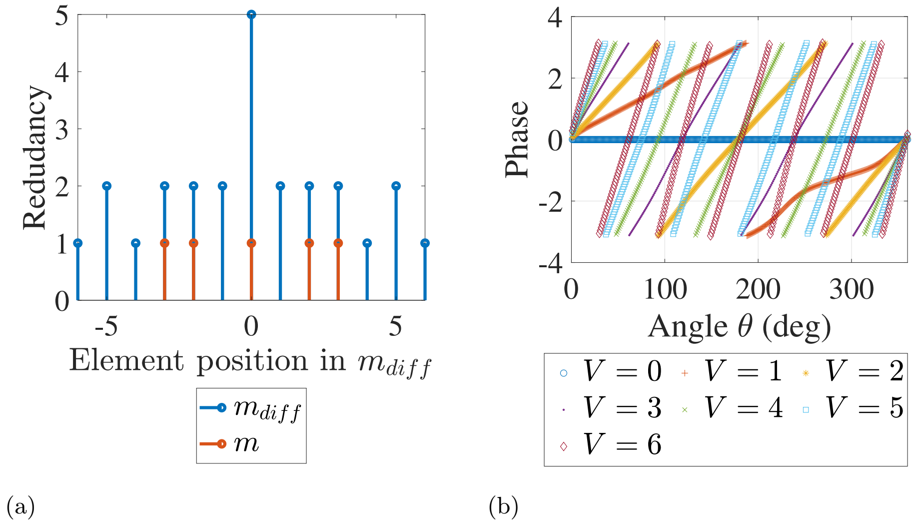

Figure 7.7: (a) Phase difference set m_{diff} of virtual SM (b) Phase patterns of virtual SM. Reproduced from [102]

.

equal to M, expressed as $w(0) = M$. For any non-zero element d in m_{diff}, the redundancy function satisfies $1 \leq w(d) \leq M-1$. The function is symmetric, meaning $w(d) = w(-d)$ for all $d \in m_{\text{diff}}$. The total redundancy across all non-zero elements in m_{diff} is $\sum_{d\in m_{\text{diff}}, d\neq 0} w(d) = M(M-1)$. Consequently, the maximum number of virtual modes can be achieved for m_{diff} is given by $M(M-1)+1$.

Therefore, by optimizing the modes within a compact-sized SMB antenna, the system can detect more sources simultaneously than the number of excited SM.

Fig. 7.7 (a) shows the elements and their redundancy in m_{diff} for an SMB antenna with $m = \{-3, -2, 0, +2, +3\}$, comprising 13 elements:

$$m_{\text{diff}} = \{-6, -5, -4, -3, -2, -1, 0, +1, +2, +3, +4, +5, +6\}.$$

These new modes correspond to distinct antenna response vectors, and the cardinality $|m_{\text{diff}}|-1$ indicates the maximum number of detectable simultaneous signals. However, by reshaping $\mathbf{X}_{m_{\text{diff}}}$ into a Toeplitz matrix, it acts as the covariance matrix of the received data from an antenna configured with seven distinct modes, with phase variances $V = \{0, +1, +2, +3, +4, +5, +6\}$. Fig. 7.7 (b) shows the phase patterns corresponding to these modes, facilitating the simultaneous detection of six uncorrelated signals using a 5-port antenna with $m = \{-3, -2, 0, +2, +3\}$.

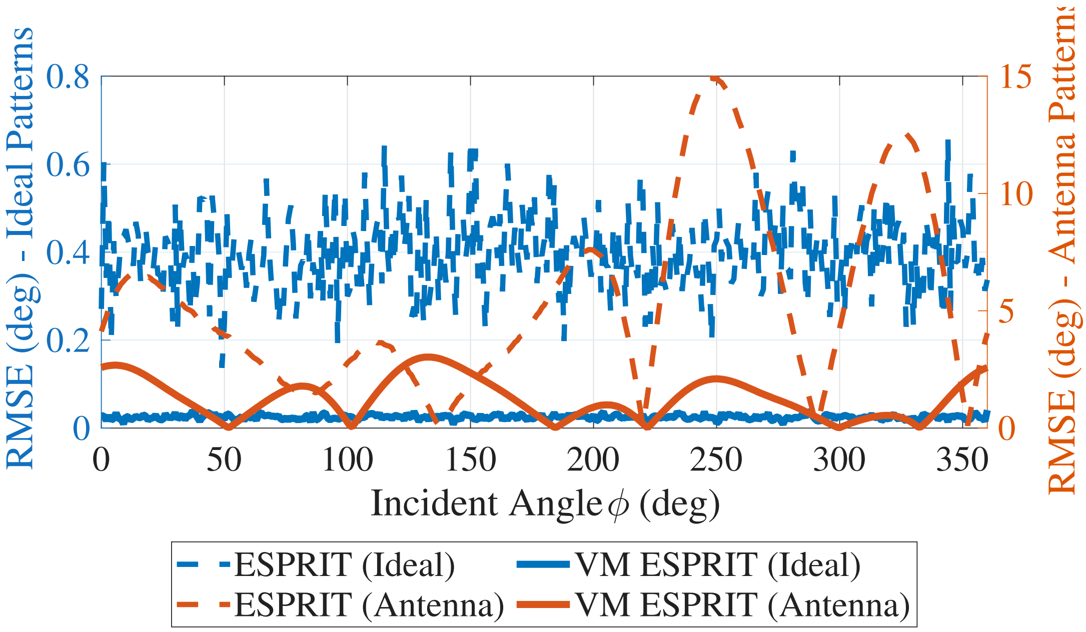

FIGURE 7.8: RMSE vs. angle for ESPRIT with and without virtual mode–based approach on ideal patterns and antenna patterns (SNR= 15 dB, $N = 100$). Reproduced from [102].

7.6 Performance Analysis

The proposed methodology was evaluated using representative radiation patterns of the antenna reported in [105]. Two scenarios were considered: ideal radiation patterns with perfect phase relationships, and full-wave simulated radiation patterns (including phase imperfections and mutual coupling effects) obtained from CST Microwave Studio.

The estimation accuracy is quantified using the RMSE, as defined in (7.10). Figure 7.8 compares the estimation accuracy of ESPRIT with and without the virtual mode–based approach, using both ideal radiation patterns and antenna-generated patterns from [105]. For reliable AoA estimation, ESPRIT conventionally relies on pairs of identical sensors, referred to as doublets. In the non–virtual mode ESPRIT implementation, doublets are constructed from the available phase patterns, where $m1$ and $m3$ form the first doublet, and $m4$ and $m2$ form the second.

When the virtual mode–based approach is applied, seven virtual modes with uniformly distributed phase variations are synthesized. This facilitates the application of ESPRIT and increases the number of usable doublets from two to six. As a result, a significant reduction in RMSE is achieved compared to the conventional ESPRIT implementation. The RMSE behavior observed for the antenna-generated radiation patterns, both with and

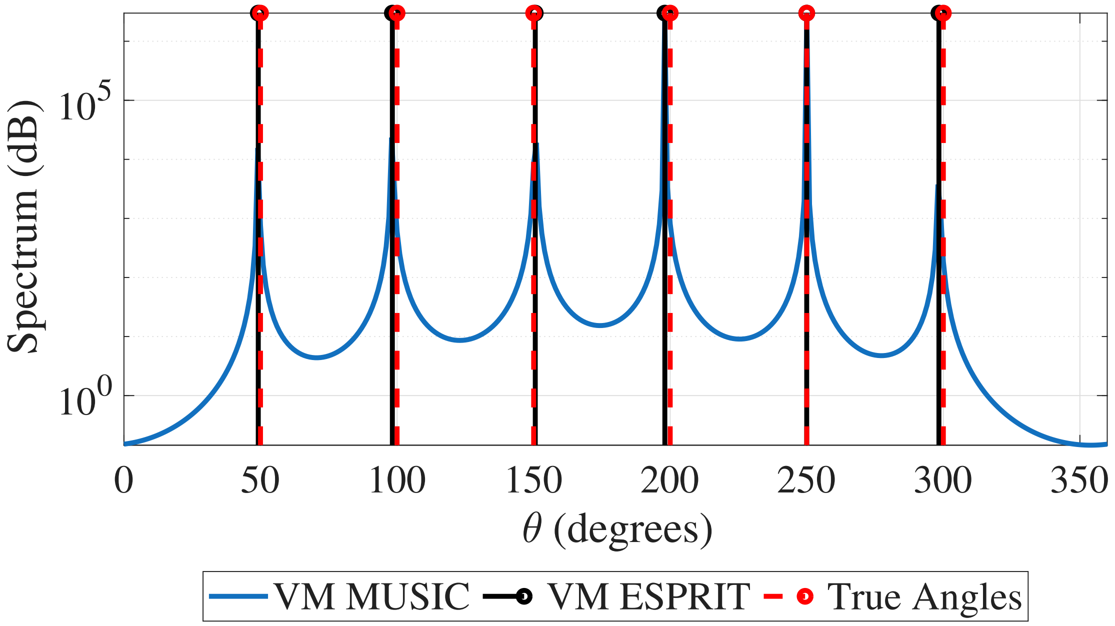

FIGURE 7.9: Multiple source estimation using virtual mode–based MUSIC and ESPRIT with 5 ports (SNR= 15 dB, $N = 100$). Reproduced from [102].

without virtual modes, arises from deviations at certain angles relative to the ideal radiation patterns. Nonetheless, the virtual mode–based approach exhibits enhanced robustness to phase imperfections, yielding lower estimation errors for the antenna-generated patterns.

For the five-port antenna considered in this work, $L = 7$. Accordingly, both MUSIC and ESPRIT are capable of resolving up to six uncorrelated sources. Figure 7.13 illustrates the detection of six uncorrelated sources arriving from 50°, 100°, 150°, 200°, 250°, and 300° using the virtual mode–based approach. Both algorithms exhibit six clearly distinguishable peaks at the corresponding directions.

Furthermore, as shown in Fig. 7.10, for ideal phase patterns, the RMSE of both MUSIC and ESPRIT decreases with increasing SNR. In contrast, when antenna-generated phase patterns are used, deviations at certain angles from the theoretically expected radiation patterns given in (7.4) hinder further improvements in estimation accuracy as the SNR increases. This behavior highlights a limitation of the approach, as it is sensitive to phase imperfections in the radiation patterns relative to the ideal case. Such phase errors can induce performance degradation that exceeds the impact of additive Gaussian noise on the proposed algorithm.

Despite this limitation, Fig. 7.8 shows that the errors caused by phase imperfections are significantly reduced when the proposed virtual mode–based approach is employed,

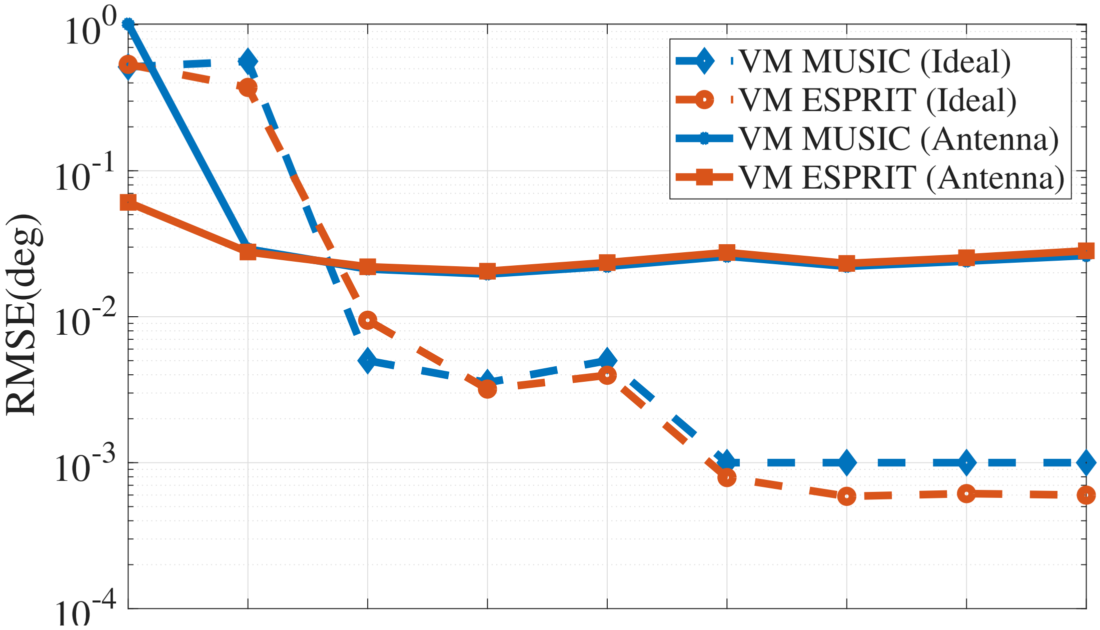

FIGURE 7.10: RMSE vs. SNR for virtual mode–based MUSIC and ESPRIT on ideal and antenna generated phase patterns of 5 port SMB antenna for two sources $\in (0°, 360°)$. Reproduced from [102].

compared to the non-virtual mode implementation on an SMB antenna. Nevertheless, the estimation accuracy achieved by MUSIC and ESPRIT remains comparable in both cases. ESPRIT, however, offers improved computational efficiency over MUSIC by eliminating the need for grid-based angle searches. Consequently, for AoA estimation applications, virtual mode–based ESPRIT applied to SMB antennas emerges as a compelling solution, combining compact antenna architecture, enhanced degrees of freedom, and reduced computational complexity.

7.7 Complexity Analysis of the Proposed Method

When employing the virtual mode–based MUSIC or ESPRIT approach, an SMB antenna excited with M spherical modes is capable of resolving up to $L-1$ sources. In conventional MUSIC, detecting $L-1$ sources requires L modes, with a computational cost of $O(S|L|^2)$ for covariance matrix estimation using S snapshots, $O(|L|^3)$ for eigenvalue decomposition, and $O(Q|L|^2)$ for the angular grid search, where Q denotes the number of grid points. This results in an overall computational complexity of $O(S|L|^2+|L|^3+Q|L|^2)$.

In the case of ESPRIT, the grid-based angle search is replaced by direct AoA estimation

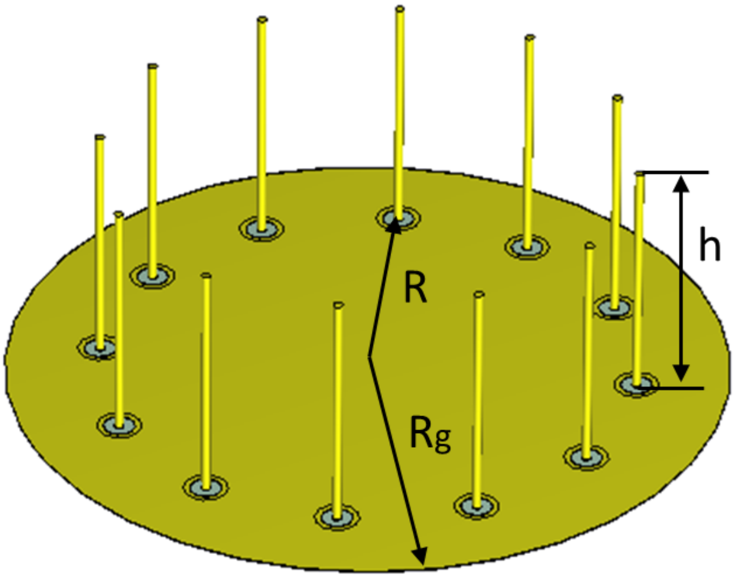

FIGURE 7.11: Simulated structure of the 12 element circular antenna array used to generate omnidirectional spherical modes. Reproduced from [103].

via the rotational invariance matrix, which requires only $O((L-1)^3)$ operations. Consequently, the total computational complexity of ESPRIT is reduced to $O(S|L|^2+|L|^3+(L-1)^3)$.

For both virtual mode–based MUSIC and ESPRIT, additional processing steps include the construction of $\mathbf{x}_{m_{\text{diff}}}$ and the formation of the matrix $\mathbf{R}$. Since $\mathbf{x}_{m_{\text{diff}}}$ is obtained directly from the covariance matrix $\mathbf{R}_{\mathbf{X}_m}$, and $\mathbf{R}$ is constructed through a rearrangement of $\mathbf{x}_{m_{\text{diff}}}$, these steps do not introduce additional multiplication operations. Therefore, the proposed virtual mode–based approach does not increase the overall computational complexity.

7.8 Exploration of a Different Set of Virtual Spherical Modes

For the exploration of a different set of virtual spherical modes, the omnidirectional spherical modes of interest are generated using a simple 12-element circular array (seen in Fig. 7.11), with monopole radiators spread evenly around a circle of radius $R = 29$ mm. The radius of the circular groundplane is $R_g = 39$ mm, with each monopole being $h = 27$ mm. Although much more sophisticated and compact SMB antennas have been proposed in the literature [111], [112], the use of circular array allows to generate relatively high-order

Table 7.3: Phase excitations used to generate spherical modes of different order m. For brevity, only phase progression between neighbouring ports is stated.

Mode	Phase progression between ports
$m = -5$	$-150°$
$m = -4$	$-120°$
$m = -3$	$-90°$
$m = -2$	$-60°$
$m = -1$	$-30°$
$m = 0$	$0°$
$m = +1$	$+30°$
$m = +2$	$+60°$
$m = +3$	$+90°$
$m = +4$	$+120°$
$m = +5$	$+150°$

modes and analyse the mode-related AoA estimation independently from most antenna specific effects. The modes are generated at 2.6 GHz.

To synthesize omnidirectional spherical modes, all antenna ports are excited with equal amplitudes, while appropriate phase variations are applied as specified in Table 7.3. For a 12-element array, this strategy enables the generation of spherical modes up to the $\pm 5^{\text{th}}$ order without violating the Shannon–Nyquist sampling criterion, which in this context requires the phase difference between adjacent antenna elements to remain below 180°. Accordingly, the following spherical modes are generated:

$$m = \{-5, -4, -3, -2, 0, +2, +3, +4, +5\}.$$

It should be noted that different modes exhibit varying radiation efficiencies [113]. Therefore, amplitude weighting is applied to each mode to ensure comparable received signal levels across all generated modes.

In this section, virtual mode generation is investigated using different combinations of spherical modes. Figure 7.12(a) presents the phase-difference set corresponding to an antenna excited with eleven spherical modes $\{-5, -4, -3, -2, -1, 0, 1, 2, 3, 4, 5\}$, which constitute the original modes obtained by applying appropriate phase shifts to the antenna illustrated in Fig. 7.11. This configuration enables the resolution of up to ten distinct targets, consistent with the availability of eleven modes.

Figure 7.12(b) shows the resulting virtual mode set spanning from -10 to 10, derived from the original spherical modes. Although the initial set contains only 11 modes, the pairwise phase-difference operation expands the virtual mode set to 21 modes. However, several of these virtual modes are redundant, thereby reducing the effective degrees of freedom.

Figure 7.12(c) illustrates a virtual mode set, also extending from -10 to 10, generated using a reduced subset of spherical modes $\{-5, -4, -3, -1, 1, 3, 4, 5\}$, where modes 0 and ± 2 are omitted. Despite this reduction, the same virtual modes as those obtained from the full set are preserved, while the redundancy is significantly decreased.

Finally, Fig. 7.12(d) depicts the virtual mode set produced using an even smaller subset of spherical modes $\{-5, -3, 1, 2, 4, 5\}$. In this case, redundancy within the virtual mode set is further minimized, yet the resulting virtual modes remain unchanged, demonstrating that fewer spherical modes can be sufficient to generate an equivalent virtual mode set.

The radiation patterns employed in this study, including the effects of phase imperfections and mutual coupling, were generated using CST Microwave Studio with the time-domain solver. For the selected subset of spherical modes $\{-5, -3, 1, 2, 4, 5\}$, both MUSIC and ESPRIT are able to resolve up to ten uncorrelated sources. Figure 7.13 demonstrates the detection of ten uncorrelated sources arriving from 33°, 65°, 98°, 131°, 163°, 196°, 228°, 261°, 294°, and 326° by exploiting the generated virtual modes. The outputs of both algorithms exhibit ten clearly distinguishable peaks at the corresponding directions, confirming accurate AoA estimation. For this experiment, the SNR is set to 10 dB, and 100 snapshots are used in the estimation process.

The accuracy of the estimates is quantified using the RMSE, which is formulated as as eq.7.10.

Figure 7.14 presents the RMSE as a function of SNR for the detection of ten sources using different spherical mode configurations. It is observed that the original set of eleven modes results in a higher estimation error across the entire SNR range when resolving ten sources, compared to the alternative configurations. In contrast, the use of virtual modes leads to a substantial reduction in error. In particular, virtual modes generated from the reduced spherical mode subsets $\{-5, -4, -3, -1, 1, 3, 4, 5\}$ and $\{-5, -3, 1, 2, 4, 5\}$ achieve the lowest RMSE.

These results demonstrate that an appropriate selection of spherical mode subsets can produce the same virtual mode set while minimizing redundancy and improving detection

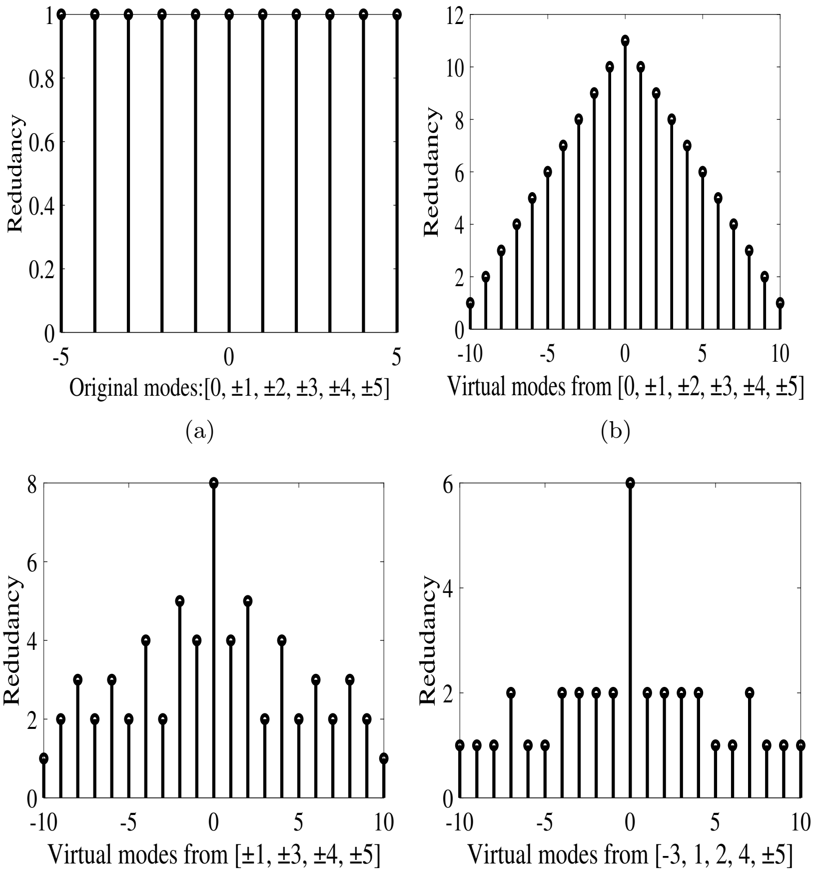

(a) (b)

(c) (d)

Figure 7.12: Virtual mode generation using different sets of spherical modes. (a) Phase difference set for an antenna with eleven spherical modes $\{-5, -4, -3, -2, -1, 0, 1, 2, 3, 4, 5\}$. (b) Virtual mode set created from the original mode set, expanding to 21 modes with some redundancy. (c) Virtual mode set generated using a reduced subset $\{-5, -4, -3, -1, 1, 3, 4, 5\}$, where modes 0 and ± 2 are excluded. (d) Virtual mode set created using an even smaller subset $\{-5, -3, 1, 2, 4, 5\}$. Reproduced from [103].

accuracy, without sacrificing the ability to resolve multiple targets. The findings further indicate that a reduced mode configuration can deliver performance comparable to that of the full mode set, thereby enhancing the efficiency of the antenna system. From a practical perspective, this enables a reduction in the number of RF chains required for AoA estimation in multiport antenna architectures.

7.9 Summary

This chapter begins by evaluating traditional AoA estimation algorithms applied to spherical-mode-driven antennas. The analysis shows that MUSIC offers the highest accuracy, making it the preferred option when precision is critical. In contrast, ESPRIT provides a viable

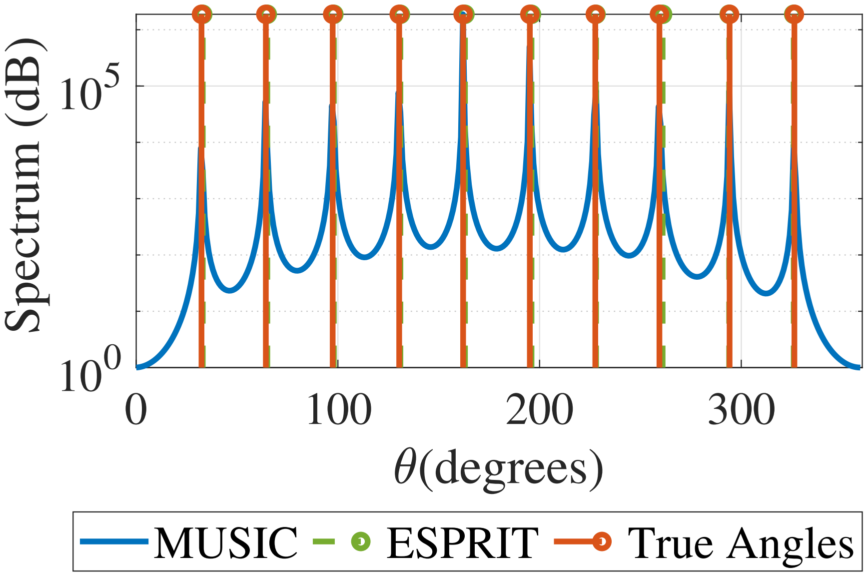

FIGURE 7.13: Detection of 10 uncorrelated sources from the directions $33°, 65°, 98°, 131°, 163°, 196°, 228°, 261°, 294°, 326°$ using the virtual modes generated from the subset $\{-5, -3, 1, 2, 4, 5\}$. Reproduced from [103].

alternative by sacrificing some DoF and accuracy in exchange for reduced computational complexity. This chapter then proposes a method for virtual mode generation using second-order statistics. This approach enhances DoF for multiple target detection while reducing the impact of phase imperfections compared to the conventional (non-virtual mode-based) method. Notably, the accuracy of MUSIC and ESPRIT remains comparable in both sparse and non-sparse implementations. However, ESPRIT demonstrates superior computational efficiency by eliminating the need for grid-based angle searches.

As a result, ESPRIT emerges as an optimal choice for spherical-mode-driven antennas, offering a balanced trade-off between compactness, extended DoF, and computational efficiency. Finally, the chapter explores various spherical mode configurations and demonstrates that it is possible to generate the same virtual mode set with reduced redundancy, thereby enabling more efficient and accurate multi-target detection.

These Advanced localization techniques hold promise as key components of future JSC systems, where a unified infrastructure could simultaneously support reliable wireless communications and precise environmental sensing.

These advanced AoA estimation algorithms form a key enabler for future JSC systems, where a shared sensing and communication infrastructure can provide both reliable

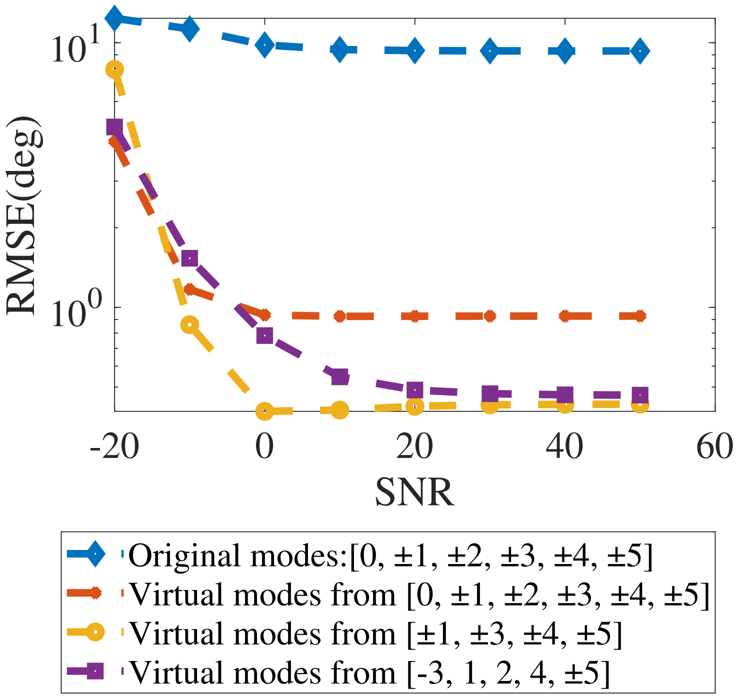

FIGURE 7.14: RMSE versus SNR for detecting 10 sources using different mode configurations. The configurations include: the original set of eleven spherical modes $\{-5,-4,-3,-2,-1,0,1,2,3,4,5\}$, the virtual mode set created from the original mode set, the virtual mode set generated using a reduced subset $\{-5,-4,-3,-1,1,3,4,5\}$, and the virtual mode set created using an even smaller subset $\{-5,-3,1,2,4,5\}$. Reproduced from [103].

wireless links and high-resolution environmental awareness within compact hardware footprints. Spherical-mode multi-port antennas enable multiple pollinating insect detection. In addition, the proposed virtual-mode framework increases the effective angular DoF while preserving low system complexity, making the architecture well suited to distributed, low-power IoT nodes for smart-agriculture applications and large-scale biodiversity monitoring.

Chapter 8

Conclusion and Future Work

This thesis introduced a novel, non-invasive framework for monitoring pollinating insects using mmWave radar and machine learning, with a focus on micro-Doppler signal analysis and advanced signal processing techniques. To address key limitations in radar entomology, the research integrated biologically inspired dynamic (EM) simulations, autonomous insect detection, hierarchical taxonomic classification, sensing via digitally modulated signals and enhanced Angle-of-Arrival (AoA) estimation for multi-target localisation using compact antenna systems.

8.1 Discussion of the Thesis Contributions

A dynamic electromagnetic insect model capable of simultaneously representing wing flapping and translational motion was developed to quantify micro-Doppler induced variations in antenna gain and reflection coefficient (S_{11}). Earlier electromagnetic representations of insects have predominantly relied on static geometries, which are inherently inadequate for analysing the time-varying scattering and radiation mechanisms produced during flapping flight. Because radar micro-Doppler signatures originate from the kinematics of moving body parts, a dynamic model that captures both periodic wing motion and bulk translation is required to establish a direct relationship between biological dynamics and measurable RF system parameters. The simulation results show that periodic insect motion produces corresponding fluctuations in both the radiated and backscattered fields, with spectral components that align with the WBF and its harmonic structure. To the best of the author's knowledge, this is the first study in which micro-Doppler effects are investigated using a fully dynamic electromagnetic insect model that incorporates both flapping motion and forward translation.

The principal limitation of the current model lies in the use of a simplified anatomical representation with homogeneous dielectric properties and without detailed morphological features such as multilayer tissue permittivity. While such refinements would influence the absolute magnitude of the scattered and radiated fields and enable more accurate species-dependent amplitude scaling, the micro-Doppler spectral structure is primarily governed by the motion of the dominant scattering components. Consequently, these simplifications are expected to affect signal amplitude rather than the fundamental frequency content or harmonic behaviour that underpins micro-Doppler–based detection and classification.

An autonomous detection algorithm was developed to identify micro-Doppler active segments within the radar signal, enabling insect presence to be inferred without manual annotation or continuous supervision. The method employs harmonic-ratio, based segmentation, where signal frames with $\eta_{\mathrm{HR}} >$ threshold are retained for further analysis. This threshold was determined empirically for the present dataset as a compromise between preserving weak but valid micro-Doppler signatures and rejecting noise-dominated or aperiodic segments. Under the measurement conditions considered, this value provided consistent separation between insect flight activity and background clutter, thereby ensuring reliable downstream feature extraction.

A limitation of this approach is that the fixed threshold is data-dependent and may not generalise directly to different radar configurations, signal-to-noise ratios, species compositions, or environmental conditions. However, the use of a constant threshold offers a transparent and computationally efficient solution that is well suited to low-power embedded implementations and provides a reproducible baseline for evaluating micro-Doppler activity. Moreover, the separability observed in the extracted wingbeat-related features for two pollinator species of different body sizes confirms that the segmentation preserves biologically meaningful signal components and supports subsequent species-level discrimination.

A hierarchical machine-learning framework was developed to enable taxonomic classification of insects down to the species level, while explainable AI was used to relate the most informative signal features to underlying biomechanical traits. Although machine-learning–based species recognition has been widely explored using visual images, its application to automated insect monitoring is often constrained by sensitivity to illumination, occlusion, and image quality. In contrast, the radar micro-Doppler signature encodes the periodic wingbeat motion and other flight dynamics, providing access to biomechanical characteristics that are not directly available in conventional image data. Systematic analysis of features associated with wing flapping, combined with SHAP-based interpretation, showed that classification is supported not only by wingbeat frequency but also by higher-order spectral descriptors such as cepstral coefficients and bandpower distributions. Using this feature space, the hierarchical model achieved an accuracy of 85% for five key pollinator species, demonstrating that radar micro-Doppler signatures contain sufficient discriminatory information for species-level recognition. While some misclassification remained at the finest taxonomic resolution, the model delivered consistent and reliable performance at genus and family levels, which are particularly relevant for ecological monitoring. Because the framework is data-driven rather than dependent on species-specific analytical formulations, it is inherently scalable and can be extended to other ecologically important groups, including pest and invasive insects.

The main limitations arise from the controlled measurement conditions and the size and diversity of the available training dataset. The insects were confined to a small enclosure, which reduced range-dependent variations in signal-to-noise ratio and occasionally introduced short-duration perturbations due to wall interactions that may have influenced some MFCC-derived features. In natural free-flight conditions, changes in range and aspect angle are expected to produce SNR fluctuations that may affect the stability of certain features. In addition, classification accuracy improved with longer micro-Doppler observation windows, indicating that reliable species-level discrimination benefits from maintaining the insect within the radar beam for sufficient time. As with all supervised learning approaches, the performance is fundamentally limited by the availability of labelled radar signatures, which are currently far fewer than image-based datasets.

Despite these constraints, the results demonstrate the feasibility of radar-based species classification and establish a foundation for scalable, non-invasive biodiversity monitoring.

While the hierarchical framework demonstrates that radar micro-Doppler signatures support reliable and interpretable species classification, embedding this sensing capability within existing wireless infrastructure facilitates practical large-scale deployment, motivating the investigation of digitally modulated mmWave communication signals for joint sensing and communication. Thus, the thesis further investigated insect detection using digitally modulated mmWave signals as an initial step toward joint sensing and communication (JSC) for pollinator monitoring. While most existing radar-based entomological studies rely on dedicated sensing waveforms, the integration of sensing functionality into communication signals remains largely unexplored. Enabling insect detection directly from communication waveforms would allow ecological monitoring to be performed using existing wireless infrastructure, significantly improving scalability and reducing deployment cost. In this work, a classification framework was developed to identify signal segments associated with wing flapping, and its performance was validated using synchronised video recordings to provide ground truth. The algorithm achieved high Precision, Recall, and F1-scores, together with an AUC of 0.91, demonstrating reliable discrimination between insect-induced micro-Doppler activity and background signal variations. These results show that micro-Doppler signatures can be preserved and detected in the presence of digital modulation, indicating that pollinator monitoring can be incorporated into a communication link without degrading its primary telecommunication functionality.

A key strength of the present study is the use of physically realistic micro-Doppler data derived from measured continuous-wave radar signals, which were combined with digitally modulated waveforms. This approach enabled a controlled and systematic investigation of how different modulation schemes influence the observability of insect-induced signatures, while avoiding the need for a fully integrated hardware implementation at this stage. It therefore provides a reproducible and flexible framework for analysing sensing–communication coexistence and establishes a clear proof of concept for JSC-based insect monitoring.

However, several limitations must be acknowledged. The micro-Doppler signatures were not measured directly from a live communication link, but were superimposed on modulated signals using experimentally acquired radar data. Although this preserves the physical realism of the insect motion, it does not fully capture real-time effects such as hardware impairments, channel dynamics, synchronization constraints, and mutual interference between sensing and communication processes. In addition, the experiments were conducted under controlled conditions, and the robustness of the approach in complex outdoor environments with multipath propagation, varying signal-to-noise ratio, and multiple simultaneous targets remains to be demonstrated.

Beyond coexistence of sensing and communication within a shared waveform, real-world ecological monitoring scenarios frequently involve multiple insects within the radar field of view, requiring spatial discrimination in addition to detection and classification. This thesis extended micro-Doppler–based insect sensing toward radar capable of angular target separation by investigating AoA estimation using spherical-mode multi-port antennas. The motivation arises from the fact that conventional SISO radar provides rich temporal signatures but cannot separate multiple insects occupying the same range–Doppler cell, while traditional phased arrays are difficult to deploy in compact, low-power ecological sensing nodes. By exploiting the orthogonality of spherical modes, a compact antenna architecture was shown to support AoA estimation. Among the algorithms evaluated, ESPRIT provided a favourable trade-off between computational complexity, memory requirements, and estimation accuracy, making it suitable for embedded implementations. To overcome the limited number of physically available modes and the absence of an inherent Vandermonde structure, a virtual-mode framework was introduced. This approach synthesises additional effective modes in the signal domain, increasing the available DoF and improving multi-target angular resolution without increasing hardware complexity. This establishes a practical pathway for integrating localisation capability into compact radar sensors for ecological monitoring.

The main limitation of this approach lies in the practical realisation and calibration of spherical-mode antennas. Accurate AoA estimation depends on maintaining the expected phase relationships between modes; however, manufacturing tolerances can distort the amplitude and phase of the excited modes, leading to angle estimation errors. Unlike conventional arrays, where phase progression is determined by element spacing, the modal phase structure must be precisely controlled through antenna design and calibration. In addition, the excitation of higher-order modes introduces increased losses, which constrains the achievable angular resolution within a compact aperture.

Despite these challenges, the virtual-mode formulation provides an effective mitigation by reconstructing a richer modal basis in the signal-processing domain, thereby restoring the degrees of freedom required for high-resolution subspace methods while preserving a compact and low-power hardware architecture. The absence of spatially separated elements also eliminates mutual coupling effects associated with dense phased arrays.

8.2 Future Research Directions

Although this thesis has addressed several key challenges in radar-based insect monitoring, it has also revealed a number of open questions and opportunities for further investigation. The following subsections outline potential directions for advancing this research.

The dynamic electromagnetic insect model can be extended by incorporating anatomically detailed geometries and dielectric properties derived from measurement or literature databases. This would enable accurate prediction of radar signatures and realistic inter-species comparisons. Such models can be implemented by importing high-resolution 3D insect meshes into full-wave solvers and assigning multilayer dielectric profiles to represent cuticle, haemolymph, and air cavities. The extended framework would also allow systematic investigation of polarimetric responses and aspect-angle dependent scattering, providing a richer physical basis for both classification and system design. In addition, the simulated time-domain responses can be used to generate large-scale physics-informed datasets for machine-learning training, reducing the dependence on extensive labelled field measurements.

For the autonomous detection stage, future work will focus on replacing the fixed harmonic-ratio threshold with adaptive, data-driven decision strategies. This can be achieved by combining the harmonic ratio with complementary spectral and temporal descriptors and learning the activity boundary using semi-supervised or self-supervised approaches. In practice, clustering or probabilistic models can be trained on unlabelled radar data to estimate the statistical distribution of insect and clutter segments, allowing the detection threshold to be inferred automatically for different radar configurations and environmental conditions. Such methods would preserve the low-complexity embedded implementation while improving robustness to noise, clutter, and inter-species variability. Implementation on embedded edge-processing platforms will allow real-time activity detection and reduce data transmission requirements in distributed sensing networks.

The hierarchical classification framework can be further developed through the expansion of the labelled radar signature database to include a wider range of species, flight behaviours, and environmental conditions. This requires coordinated field measurement campaigns in which radar recordings are synchronised with ground-truth observations and environmental metadata such as temperature and humidity are logged. The influence of range-dependent signal-to-noise ratio and aspect angle can be addressed by collecting free-flight data with controlled trajectories or by incorporating guiding structures that increase insect dwell time within the radar beam while allowing unharmed release. These developments will improve species-level generalisation and enable continuous monitoring of community composition and behavioural changes. Domain adaptation and transfer-learning techniques can also be explored to maintain classification performance across different radar hardware platforms and deployment environments without requiring complete retraining.

The joint sensing and communication concept can be advanced by implementing a fully integrated system in which the micro-Doppler signature is measured directly from a digitally modulated communication waveform. This requires a real-time hardware platform with shared RF front-end, synchronised baseband processing, and simultaneous communication and sensing operation. Adaptive equalisation algorithms can be introduced to mitigate interference and channel distortion, while joint waveform optimisation can be performed using multi-objective design techniques that balance communication quality-of-service and sensing performance. In large-scale deployments, spectrum-sharing and resource-allocation protocols can be developed and evaluated through network-level simulations and experimental multi-node testbeds. The integration of edge computing and cloud-based data aggregation will enable scalable architectures in which local sensing nodes perform initial processing and transmit compact ecological indicators rather than raw data.

For the AoA estimation framework, future work will involve the fabrication and experimental characterisation of spherical-mode multi-port antennas with precise modal amplitude and phase control. The virtual-mode formulation can then be validated in real multi-target outdoor scenarios, where AoA estimation, detection, and classification are performed simultaneously within a unified processing chain.

At the system level, long-term field deployments across diverse ecological sites will be required to assess environmental robustness, seasonal variability, and long-duration operational stability. The fusion of radar-derived indicators with environmental sensing and geospatial data within a real-time data platform will enable automated ecological analytics and support applications such as biodiversity assessment, habitat health monitoring, and precision agriculture.

Collectively, these developments will transform the current proof-of-concept implementations into a field-deployable sensing infrastructure capable of autonomous detection, classification, localisation, and communication within large-scale pollinator monitoring networks.

8.3 Conclusion

In summary, this thesis demonstrate that micro-Doppler signatures at mmWave frequencies contain sufficient biomechanical information to support reliable detection, classification to enable non-lethal, and automated monitoring of pollinating insects. By showing that these sensing capabilities can coexist with communication functionality and operate within compact hardware constraints, the work shows the feasibility of distributed radar networks for continuous biodiversity monitoring and precision agriculture.

Although the proposed system validates the core sensing principles, further work is required to transition from controlled experiments to fully operational deployments. This includes real-time implementation on embedded platforms, large-scale collection of labelled radar signatures across diverse environments, experimental verification of spherical-mode AoA estimation with fabricated antennas, and network-level integration of multifunction sensing nodes. These developments will support the emergence of autonomous sensing infrastructures that transform how insect populations are monitored, providing continuous and quantitative indicators for ecosystem health and sustainable food production.

Bibliography

[1] G. Ceballos, P. R. Ehrlich, and P. H. Raven, “Vertebrates on the brink as indicators of biological annihilation and the sixth mass extinction,” *Proceedings of the National Academy of Sciences*, vol. 117, no. 24, pp. 13 596–13 602, 2020.

[2] S. Seibold, M. M. Gossner, N. K. Simons, *et al.*, “Arthropod decline in grasslands and forests is associated with landscape-level drivers,” *Nature*, vol. 574, no. 7780, pp. 671–674, 2019.

[3] J. Ollerton, “Pollinator diversity: Distribution, ecological function, and conservation,” *Annual review of ecology, evolution, and systematics*, vol. 48, pp. 353–376, 2017.

[4] S. G. Potts, J. C. Biesmeijer, C. Kremen, P. Neumann, O. Schweiger, and W. E. Kunin, “Global pollinator declines: Trends, impacts and drivers,” *Trends in ecology & evolution*, vol. 25, no. 6, pp. 345–353, 2010.

[5] G. A. Montgomery, M. W. Belitz, R. P. Guralnick, and M. W. Tingley, “Standards and best practices for monitoring and benchmarking insects,” *Frontiers in ecology and evolution*, vol. 8, p. 579 193, 2021.

[6] R. van Klink, T. August, Y. Bas, *et al.*, “Emerging technologies revolutionise insect ecology and monitoring,” *Trends in Ecology & Evolution*, 2022.

[7] N. Kumar, N Nagarathna, and F. Flammini, “Yolo-based light-weight deep learning models for insect detection system with field adaption,” *Agriculture*, vol. 13, no. 3, p. 741, 2023.

[8] T. T. Høye, J. Ärje, K. Bjerge, *et al.*, “Deep learning and computer vision will transform entomology,” *Proceedings of the National Academy of Sciences*, vol. 118, no. 2, e2002545117, 2021.

[9] R. Van Klink, J. K. Sheard, T. T. Høye, T. Roslin, L. A. Do Nascimento, and S. Bauer, *Towards a toolkit for global insect biodiversity monitoring*, 2024.

[10] J. Riley, D. Reynolds, A. Smith, *et al.*, "Observations of the autumn migration of the rice leaf roller cnaphalocrocis medinalis (lepidoptera: Pyralidae) and other moths in eastern china," *Bulletin of Entomological Research*, vol. 85, no. 3, pp. 397–414, 1995.

[11] T. J. Mabee, B. A. Cooper, J. H. Plissner, and D. P. Young, "Nocturnal bird migration over an appalachian ridge at a proposed wind power project," *Wildlife Society Bulletin*, vol. 34, no. 3, pp. 682–690, 2006.

[12] J. W. Chapman, R. L. Nesbit, L. E. Burgin, *et al.*, "Flight orientation behaviors promote optimal migration trajectories in high-flying insects," *Science*, vol. 327, no. 5966, pp. 682–685, 2010.

[13] D. Mirkovic, P. M. Stepanian, J. F. Kelly, and P. B. Chilson, "Electromagnetic model reliably predicts radar scattering characteristics of airborne organisms," *Scientific reports*, vol. 6, no. 1, p. 35 637, 2016.

[14] C. R. Vaughn, "Birds and insects as radar targets: A review," *Proceedings of the IEEE*, vol. 73, no. 2, pp. 205–227, 1985.

[15] S. Hobbs and A. C. Aldhous, "Insect ventral radar cross-section polarisation dependence measurements for radar entomology," *IEE Proceedings-Radar, Sonar and Navigation*, vol. 153, no. 6, pp. 502–508, 2006.

[16] D. Mirkovic, P. M. Stepanian, C. E. Wainwright, D. R. Reynolds, and M. H. Menz, "Characterizing animal anatomy and internal composition for electromagnetic modelling in radar entomology," *Remote Sensing in Ecology and Conservation*, vol. 5, no. 2, pp. 169–179, 2019.

[17] F. I. Addison, T. Dally, E. J. Duncan, *et al.*, "Simulation of the radar cross section of a noctuid moth," *Remote Sensing*, vol. 14, no. 6, p. 1494, 2022.

[18] R. Wang, C. Hu, C. Liu, *et al.*, "Migratory insect multifrequency radar cross sections for morphological parameter estimation," *IEEE Transactions on Geoscience and Remote Sensing*, vol. 57, no. 6, pp. 3450–3461, 2018.

[19] C. Hu, W. Li, R. Wang, C. Liu, T. Zhang, and W. Li, "Accurate insect orientation extraction based on polarization scattering matrix estimation," *IEEE Geoscience and Remote Sensing Letters*, vol. 14, no. 10, pp. 1755–1759, 2017.

[20] R. Wang, C. Hu, X. Fu, Z. Jiang, and C. Zhang, "Micro-doppler measurement of insect wing-beat frequencies with w-band coherent radar," *Scientific Reports*, vol. 7, no. 1, p. 1396, 2017.

[21] C. Hu, S. Kong, R. Wang, T. Long, and X. Fu, "Identification of migratory insects from their physical features using a decision-tree support vector machine and its application to radar entomology," *Scientific reports*, vol. 8, no. 1, p. 5449, 2018.

[22] C. Hu, S. Kong, R. Wang, and F. Zhang, "Radar measurements of morphological parameters and species identification analysis of migratory insects," *Remote Sensing*, vol. 11, no. 17, p. 1977, 2019.

[23] R. Wang, J. Wang, W. Li, M. Li, F. Zhang, and C. Hu, "Robust estimation of insect morphological parameters for entomological radar using multi-frequency echo intensity-independent estimators," *IEEE Transactions on Geoscience and Remote Sensing*, 2024.

[24] M. Diyap, A. T. Zadeh, J. Moll, and V. Krozer, "Numerical and experimental studies on the micro-doppler signatures of freely flying insects at w-band," *Remote sensing*, vol. 14, no. 23, p. 5917, 2022.

[25] N. Aldabashi, S. M. Williams, A. Eltokhy, E. Palmer, P. Cross, and C. Palego, "A machine learning integrated 5.8-ghz continuous-wave radar for honeybee monitoring and behavior classification," *IEEE Transactions on Microwave Theory and Techniques*, vol. 71, no. 9, pp. 4098–4108, 2023.

[26] A. Zandamela, A. Chiumento, N. Marchetti, M. J. Ammann, and A. Narbudowicz, "Exploiting Multimode Antennas for MIMO and AoA Estimation in Size-Constrained IoT Devices," *IEEE Sensors Letters*, vol. 7, no. 3, pp. 1–4, 2023.

[27] R. Van Klink, D. E. Bowler, K. B. Gongalsky, A. B. Swengel, A. Gentile, and J. M. Chase, "Meta-analysis reveals declines in terrestrial but increases in freshwater insect abundances," *Science*, vol. 368, no. 6489, pp. 417–420, 2020.

[28] E. E. Zattara and M. A. Aizen, “Worldwide occurrence records suggest a global decline in bee species richness,” *One Earth*, vol. 4, no. 1, pp. 114–123, 2021.

[29] C. Carvell, J. Osborne, A. Bourke, S. Freeman, R. F. Pywell, and M. Heard, “Bumble bee species’ responses to a targeted conservation measure depend on landscape context and habitat quality,” *Ecological Applications*, vol. 21, no. 5, pp. 1760–1771, 2011.

[30] J. W. Campbell and J. Hanula, “Efficiency of malaise traps and colored pan traps for collecting flower visiting insects from three forested ecosystems,” *Journal of Insect Conservation*, vol. 11, no. 4, pp. 399–408, 2007.

[31] M. A. Ebrahimi, M. H. Khoshtaghaza, S. Minaei, and B. Jamshidi, “Vision-based pest detection based on svm classification method,” *Computers and Electronics in Agriculture*, vol. 137, pp. 52–58, 2017.

[32] A. N. Alves, W. S. Souza, and D. L. Borges, “Cotton pests classification in field-based images using deep residual networks,” *Computers and Electronics in Agriculture*, vol. 174, p. 105 488, 2020.

[33] T. Kasinathan, D. Singaraju, and S. R. Uyyala, “Insect classification and detection in field crops using modern machine learning techniques,” *Information Processing in Agriculture*, vol. 8, no. 3, pp. 446–457, 2021.

[34] M. Besson, J. Alison, K. Bjerge, *et al.*, “Towards the fully automated monitoring of ecological communities,” *Ecology letters*, vol. 25, no. 12, pp. 2753–2775, 2022.

[35] E. D. Chesmore, “Application of time domain signal coding and artificial neural networks to passive acoustical identification of animals,” *Applied Acoustics*, vol. 62, no. 12, pp. 1359–1374, 2001.

[36] I. Potamitis, T. Ganchev, and N. Fakotakis, “Automatic acoustic identification of insects inspired by the speaker recognition paradigm.,” in *INTERSPEECH*, 2006.

[37] A. B. Kohlberg, C. R. Myers, and L. L. Figueroa, “From buzzes to bytes: A systematic review of automated bioacoustics models used to detect, classify and monitor insects,” *Journal of Applied Ecology*, vol. 61, no. 6, pp. 1199–1211, 2024.

[38] D. Unwin and C. Ellington, “An optical tachometer for measurement of the wing-beat frequency of free-flying insects,” *Journal of Experimental Biology*, vol. 82, no. 1, pp. 377–378, 1979.

[39] Y. Chen, A. Why, G. Batista, A. Mafra-Neto, and E. Keogh, “Flying insect classification with inexpensive sensors,” *Journal of insect behavior*, vol. 27, no. 5, pp. 657–677, 2014.

[40] H. Chen, M. Li, H. Månefjord, *et al.*, “Lidar as a potential tool for monitoring migratory insects,” *Iscience*, vol. 27, no. 5, 2024.

[41] A. Noskov, J. Bendix, and N. Friess, “A review of insect monitoring approaches with special reference to radar techniques,” *Sensors*, vol. 21, no. 4, p. 1474, 2021.

[42] R Hajovsky, A Deam, and A LaGrone, “Radar reflections from insects in the lower atmosphere,” *IEEE Transactions on Antennas and Propagation*, vol. 14, no. 2, pp. 224–227, 1966.

[43] C Tolbert, A Straiton, and C Britt, “Phantom radar targets at millimeter radio wavelengths,” *IRE Transactions on antennas and Propagation*, vol. 6, no. 4, pp. 380–384, 1958.

[44] S. Kong, C. Hu, R. Wang, *et al.*, “Insect multifrequency polarimetric radar cross section: Experimental results and analysis,” *IEEE Transactions on Geoscience and Remote Sensing*, vol. 59, no. 8, pp. 6573–6585, 2020.

[45] C. Hu, W. Li, R. Wang, T. Long, and V. A. Drake, “Discrimination of parallel and perpendicular insects based on relative phase of scattering matrix eigenvalues,” *IEEE Transactions on Geoscience and Remote Sensing*, vol. 58, no. 6, pp. 3927–3940, 2020.

[46] R. Wang, J. Cai, C. Hu, C. Zhou, and T. Zhang, “A novel radar detection method for sensing tiny and maneuvering insect migrants,” *Remote Sensing*, vol. 12, no. 19, p. 3238, 2020.

[47] C. Waldschmidt, J. Hasch, and W. Menzel, “Automotive radar—from first efforts to future systems,” *IEEE Journal of Microwaves*, vol. 1, no. 1, pp. 135–148, 2021.

[48] M. I. Skolnik, “Radar handbook,” *IEEE Aerospace Electronic Systems Magazine*, vol. 23, no. 5, pp. 41–41, 2008.

[49] M. A. Richards *et al.*, *Fundamentals of radar signal processing.* Mcgraw-hill New York, 2005, vol. 1.

[50] H.-J. Li, Y.-W. Kiang, and W. Chen, "Radar and inverse scattering," *The Electrical Engineering Handbook*, pp. 671–690, 2005.

[51] A. G. Stove, "Linear fmcw radar techniques," in *IEE Proceedings F (Radar and Signal Processing)*, IET, vol. 139, 1992, pp. 343–350.

[52] Y. Liqiang, F. Haozheng, X. Jing, *et al.*, "Pushing the boundaries of aphid detection: An investigation into mmwaveradar and machine learning synergy," *Computers and Electronics in Agriculture*, vol. 229, p. 109 655, 2025.

[53] R. Dudley, *The biomechanics of insect flight: form, function, evolution.* Princeton university press, 2002.

[54] M. A. Deakin, "Formulae for insect wingbeat frequency," *Journal of Insect Science*, vol. 10, no. 1, 2010.

[55] D. N. Byrne, S. L. Buchmann, and H. G. Spangler, "Relationship between wing loading, wingbeat frequency and body mass in homopterous insects," *Journal of Experimental Biology*, vol. 135, no. 1, pp. 9–23, 1988.

[56] C.-A. Darveau, "Insect flight energetics and the evolution of size, form, and function," *Integrative and Comparative Biology*, vol. 64, no. 2, pp. 586–597, 2024.

[57] M. P. Tercel, F. Veronesi, and T. W. Pope, "Phylogenetic clustering of wingbeat frequency and flight-associated morphometrics across insect orders," *Physiological Entomology*, vol. 43, no. 2, pp. 149–157, 2018.

[58] J. H. Jensen, J. C. Dyre, and T. Hecksher, "Universal wing-and fin-beat frequency scaling," *Plos One*, vol. 19, no. 6, e0303834, 2024.

[59] V. A. Drake and D. R. Reynolds, *Radar entomology: observing insect flight and migration.* Cabi, 2012.

[60] V. Drake, J. Chapman, K. Lim, D. Reynolds, J. Riley, and A. Smith, "Ventral-aspect radar cross sections and polarization patterns of insects at x band and their relation to size and form," *International Journal of Remote Sensing*, vol. 38, no. 18, pp. 5022–5044, 2017.

[61] J. R. Riley, “Radar cross section of insects,” *Proceedings of the IEEE*, vol. 73, no. 2, pp. 228–232, 1985.

[62] J. Riley, “A millimetric radar to study the flight of small insects,” *Electronics & communication engineering journal*, vol. 4, no. 1, pp. 43–48, 1992.

[63] R. Wang, C. Hu, C. Liu, *et al.*, “Migratory insect multifrequency radar cross sections for morphological parameter estimation,” *IEEE Transactions on Geoscience and Remote Sensing*, vol. 57, no. 6, pp. 3450–3461, 2018.

[64] O. Alzaabi, *Airborne Insect Radar Scattering Characterization Using Electromagnetic Modeling.* The Pennsylvania State University, 2019.

[65] S. Nelson, P. Bartley, K. Lawrence, *et al.*, “RF and microwave dielectric properties of stored-grain insects and their implications for potential insect control,” *Transactions of the ASAE*, vol. 41, no. 3, pp. 685–692, 1998.

[66] H. Chen, X. Li, W. Yu, *et al.*, “Chitin/mos2 nanosheet dielectric composite films with significantly enhanced discharge energy density and efficiency,” *Biomacromolecules*, vol. 21, no. 7, pp. 2929–2937, 2020.

[67] H. L. Van Trees, *Optimum array processing: Part IV of detection, estimation, and modulation theory.* John Wiley & Sons, 2002.

[68] L. C. Godara, “Application of antenna arrays to mobile communications. II. Beamforming and direction-of-arrival considerations,” *Proceedings of the IEEE*, vol. 85, no. 8, pp. 1195–1245, 1997.

[69] S. S. Haykin, *Adaptive filter theory.* Pearson Education India, 2002.

[70] R. Schmidt, “Multiple emitter location and signal parameter estimation,” *IEEE Trans. on Ant. and Prop.*, vol. 34, no. 3, pp. 276–280, 1986.

[71] R. Roy and T. Kailath, “ESPRIT-estimation of signal parameters via rotational invariance techniques,” *IEEE Transactions on acoustics, speech, and signal processing*, vol. 37, no. 7, pp. 984–995, 1989.

[72] L. Antony, N. Marchetti, and A. Narbudowicz, “Modelling of micro-doppler effect in mm-wave antenna due to near-field insect fly-by,” in *2023 IEEE International Symposium On Antennas And Propagation (ISAP)*, IEEE, 2023, pp. 1–2.

[73] V. C. Chen, F. Li, S.-S. Ho, and H. Wechsler, "Micro-doppler effect in radar: Phenomenon, model, and simulation study," *IEEE Transactions on Aerospace and electronic systems*, vol. 42, no. 1, pp. 2–21, 2006.

[74] J. R. Riley, A. Smith, and D. Reynolds, "The feasibility of using vertical-looking radar to monitor the migration of brown planthopper and other insect pests of rice in china," *Insect Science*, vol. 10, no. 1, pp. 1–19, 2003.

[75] L. Antony, N. Marchetti, I. Donohue, and A. Narbudowicz, "Insect detection using mm-waves: Integrated communication and biodiversity sensing based on micro-doppler effects," *IEEE Access*, 2025.

[76] A. Thomas, A. Ludlow, and J. Kennedy, "Sinking speeds of falling and flying aphis fabae scopoli," *Ecological Entomology*, vol. 2, no. 4, pp. 315–326, 1977.

[77] A. Santhanakrishnan, A. K. Robinson, S. Jones, *et al.*, "Clap and fling mechanism with interacting porous wings in tiny insect flight," *Journal of Experimental Biology*, vol. 217, no. 21, pp. 3898–3909, 2014.

[78] S. A. Gauthreaux Jr, "The flight behavior of migrating birds in changing wind fields: Radar and visual analyses," *American Zoologist*, vol. 31, no. 1, pp. 187–204, 1991.

[79] L. Antony, N. Marchetti, I. Donohue, and A. Narbudowicz, "Statistical analysis of mm-wave signals for enhanced biodiversity monitoring,"

[80] H. G. Spangler and S. L. Buchmann, "Effects of temperature on wingbeat frequency in the solitary bee centris caesalpiniae (anthophoridae: Hymenoptera)," *Journal of the Kansas Entomological Society*, vol. 64, no. 1, pp. 107–109, 1991. [Online]. Available: `http://www.jstor.org/stable/25085252` (visited on 03/26/2023).

[81] H.-G. Kim, N. Moreau, and T. Sikora, *MPEG-7 audio and beyond: Audio content indexing and retrieval.* John Wiley & Sons, 2006.

[82] G. Peeters, "A large set of audio features for sound description (similarity and classification) in the cuidado project," *CUIDADO Ist Project Report*, vol. 54, no. 0, pp. 1–25, 2004.

[83] J. D. Johnston, "Transform coding of audio signals using perceptual noise criteria," *IEEE Journal on selected areas in communications*, vol. 6, no. 2, pp. 314–323, 1988.

[84] E. Scheirer and M. Slaney, "Construction and evaluation of a robust multifeature speech/music discriminator," in *1997 IEEE international conference on acoustics, speech, and signal processing*, IEEE, vol. 2, 1997, pp. 1331–1334.

[85] J. G. Proakis, *Digital signal processing: principles, algorithms, and applications, 4/E.* Pearson Education India, 2007.

[86] D. N. Joanes and C. A. Gill, "Comparing measures of sample skewness and kurtosis," *Journal of the Royal Statistical Society: Series D (The Statistician)*, vol. 47, no. 1, pp. 183–189, 1998.

[87] S. Gonzalez and M. Brookes, "A pitch estimation filter robust to high levels of noise (pefac)," in *2011 19th European Signal Processing Conference*, IEEE, 2011, pp. 451–455.

[88] A. M. Noll, "Cepstrum pitch determination," *The journal of the acoustical society of America*, vol. 41, no. 2, pp. 293–309, 1967.

[89] B. S. Atal, "Automatic speaker recognition based on pitch contours," *The Journal of the Acoustical Society of America*, vol. 52, no. 6B, pp. 1687–1697, 1972.

[90] The MathWorks, Inc., *Matlab*, Computer software, Version R2024a, 2024. [Online]. Available: `https://www.mathworks.com/products/matlab.html`.

[91] C. M. Bishop and N. M. Nasrabadi, *Pattern recognition and machine learning.* Springer, 2006, vol. 4.

[92] I. Goodfellow, Y. Bengio, A. Courville, and Y. Bengio, *Deep learning.* MIT press Cambridge, 2016, vol. 1.

[93] P. Geurts, D. Ernst, and L. Wehenkel, "Extremely randomized trees," *Machine learning*, vol. 63, no. 1, pp. 3–42, 2006.

[94] T. Hastie, R. Tibshirani, J. Friedman, *et al.*, *The elements of statistical learning*, 2009.

[95] L. Prokhorenkova, G. Gusev, A. Vorobev, A. V. Dorogush, and A. Gulin, "Catboost: Unbiased boosting with categorical features," *Advances in neural information processing systems*, vol. 31, 2018.

[96] J. Opitz, "A closer look at classification evaluation metrics and a critical reflection of common evaluation practice," *Transactions of the Association for Computational Linguistics*, vol. 12, pp. 820–836, 2024.

[97] S. M. Lundberg, G. Erion, H. Chen, *et al.*, "From local explanations to global understanding with explainable ai for trees," *Nature machine intelligence*, vol. 2, no. 1, pp. 56–67, 2020.

[98] K. M. Glover, K. R. Hardy, T. G. Konrad, W. N. Sullivan, and A. Michaels, "Radar observations of insects in free flight: Radar tracking of single insects in the atmosphere leads to detection of distinctive phenomena.," *Science*, vol. 154, no. 3752, pp. 967–972, 1966.

[99] N. S. Altman, "An introduction to kernel and nearest-neighbor nonparametric regression," *The American Statistician*, vol. 46, no. 3, pp. 175–185, 1992.

[100] T. J. Wolf, C. P. Ellington, S. Davis, and M. J. Feltham, "Validation of the doubly labelled water technique for bumblebees bombus terrestris (l.)," *Journal of Experimental Biology*, vol. 199, no. 4, pp. 959–972, 1996.

[101] L. Antony, A. Zandamela, N. Marchetti, and A. Narbudowicz, "Angle of arrival estimation methods using spherical-modes-driven multiport antennas," in *2024 18th European Conference on Antennas and Propagation (EuCAP)*, IEEE, 2024, pp. 1–5.

[102] L. Antony, A. Zandamela, N. Marchetti, and A. Narbudowicz, "Virtual spherical modes for aoa estimation with small sub-wavelength antennas," *IEEE Antennas and Wireless Propagation Letters*, 2024.

[103] L. Antony and A. Narbudowicz, "Study of virtual spherical modes for multi-target angle of arrival estimation," in *2025 19th European Conference on Antennas and Propagation (EuCAP)*, IEEE, 2025, pp. 1–5.

[104] W. Hansen, "A new type of expansion in radiation problems," *Physical review*, vol. 47, no. 2, p. 139, 1935.

[105] A. Zandamela, N. Marchetti, M. J. Ammann, and A. Narbudowicz, "Spherical Modes Driven Directional Modulation With a Compact MIMO Antenna," *IEEE Antennas and Wireless Propagation Letters*, vol. 22, no. 3, pp. 477–481, 2023.

[106] P. Chevalier, L. Albera, A. Ferréol, and P. Comon, "On the virtual array concept for higher order array processing," *IEEE Transactions on Signal Processing*, vol. 53, no. 4, pp. 1254–1271, 2005.

[107] P. Pal and P. P. Vaidyanathan, "Nested arrays: A novel approach to array processing with enhanced degrees of freedom," *IEEE Transactions on Signal Processing*, vol. 58, no. 8, pp. 4167–4181, 2010.

[108] C.-L. Liu and P. Vaidyanathan, "Remarks on the spatial smoothing step in coarray MUSIC," *IEEE Signal Processing Letters*, vol. 22, no. 9, pp. 1438–1442, 2015.

[109] D. G. Chachlakis and P. P. Markopoulos, "Structured autocorrelation matrix estimation for coprime arrays," *Signal Processing*, vol. 183, p. 107 987, 2021.

[110] L. Antony, A. Zandamela, N. Marchetti, and A. Narbudowicz, "Angle of Arrival Estimation Methods Using Spherical-Modes-Driven Multiport Antennas," in *EUCAP 2024*, European Conference on Antennas and Propagation (EuCAP), 2024.

[111] A. Zandamela, N. Marchetti, M. J. Ammann, and A. Narbudowicz, "3-d beam-steering mimo antenna for on-body iot applications," *IEEE Transactions on Antennas and Propagation*, vol. 72, no. 3, pp. 2241–2251, 2024.

[112] A. Zandamela, N. Marchetti, and A. Narbudowicz, "Directional modulation for enhanced privacy in smartwatch devices: Proposing a security solution compatible with internet of things devices [bioelectromagnetics]," *IEEE Antennas and Propagation Magazine*, vol. 66, no. 2, pp. 59–90, 2024.

[113] A. A. Zandamela, K. Schraml, V. Jantarachote, *et al.*, "On the efficiency of miniaturized 360° beam-scanning antenna," in *2019 13th European Conference on Antennas and Propagation (EuCAP)*, 2019, pp. 1–4.